DETAILED DESCRIPTION AND FLIGHT PERFORMANCE OF THE RAM B VEHICLE

by James L. Raper, Robert J. Keynton, and Gerard E. Woodbury

Langley Research Center
Langley Station, Hampton, Va.

DETAILED DESCRIPTION AND FLIGHT PERFORMANCE

OF THE RAM B VEHICLE

By James L. Raper, Robert J. Keynton,
and Gerard E. Woodbury

Langley Research Center
Langley Station, Hampton, Va.

NATIONAL AERONAUTICS AND SPACE ADMINISTRATION

DETAILED DESCRIPTION AND FLIGHT PERFORMANCE

OF THE RAM B VEHICLE

By James L. Raper, Robert J. Keynton,
and Gerard E. Woodbury
Langley Research Center

SUMMARY

A general description of the performance of the second flight of the RAM B
vehicle and some selected details of the mechanical design and fabrication of
the RAM B vehicle have been presented. The purpose of the B series flight tests
was to probe the radio blackout region, to correlate and modify ionization atten-
uation theories, and to evaluate the effectiveness of methods for overcoming
signal attenuation. The RAM B vehicle fulfilled its intended mission require-
ments. The flight-test results showed that the over-all vehicle structural
design, heat shielding, and payload-stage configuration survived the unique
conditions associated with the high-temperature, jet-pluming instability envi-
ronment encountered during the flight. The vehicle successfully followed the
approximate nominal trajectory and achieved a velocity of 17,860 feet per second
at an altitude of 162,000 feet.

Flight data discussed include velocity, altitude, accelerations, and roll
rates. Angle-of-attack and component temperature histories are also presented
but are not analyzed.

INTRODUCTION

As part of a general research program of the Langley Research Center to
investigate the parameters causing radio blackout of reentry vehicle transmis-
sions and to determine as many alleviating factors for the problem as possible,
a free-flight test program utilizing multistage rocket-propelled vehicles was
initiated. The B series vehicle of this report has been used in order to boost
four times the weight and permit blunter payloads than the payload boosted in
the A series flight tests (ref. 1). Other Langley plasma attenuation investi-
gations have been limited to ground tests and theoretical studies associated
with the problem of plasma attenuation of radio transmissions (refs. 2, 3,
and 4) and to flight tests at lower speeds with limited instrumentation (ref. 5).

The three-stage, solid-propellant, unguided vehicle for the B series of the
RAM (Radio Attenuation Measurement) flight program was designed to place a
175-pound payload at a velocity of about 20,000 feet per second and at an alti-
tude of about 180,000 feet on an ascending trajectory so that an apogee of at

least 300,000 feet was attained. This report presents a detailed description of some mechanical design and construction aspects of the B series vehicle and a limited analysis of the vehicle performance during the RAM B2 flight test, payload-stage temperatures, and angular motions. Reference 6 presents a detailed analysis of the RAM B2 experiment.

The RAM B vehicle was designed to probe the region of high signal attenuation while flying an ascending trajectory so that it would transcend the so-called radio blackout region after attaining peak velocity. This type of trajectory was chosen rather than those used in the flights of reference 5 in order to reduce aerodynamic heating, to monitor vehicle and instrumentation performance before and after the radio blackout region, and to relay onboard recorded data to ground stations after flight through the plasma environment.

The 250-pound payload attained a maximum velocity of 17,860 feet per second at an altitude of 162,000 feet. Trajectory apogee was 290,000 feet. The flight test was conducted on May 28, 1963, from the NASA Wallops Station.

The RAM B1 vehicle experienced an abrupt thrust termination due to motor failure after approximately one-fourth of the second-stage thrusting period. Because the flight conditions were not attained, no formal report has been made of the RAM B1 flight.

SYMBOLS

A_t cross-sectional area of nozzle throat, sq in.

$a_{L,Hi}$ high-range longitudinal accelerometer reading, positive in positive X-direction, g units

$a_{L,Lo}$ low-range longitudinal accelerometer reading, positive in positive X-direction, g units

$a_{L,Vib}$ longitudinal vibrometer reading, positive in positive X-direction, g units

a_T transverse accelerometer reading, positive in positive Y-direction, g units.

C_{D_O} axial-force coefficient at zero angle of attack

C_d nozzle discharge coefficient

C_F thrust coefficient

C_N normal-force coefficient

C_{N_α} normal-force-curve slope per degree

$C_{p,t}$ Newtonian total-pressure coefficient

F thrust, lb

M Mach number

p_c chamber pressure, psia

$\Delta p_\alpha, \Delta p_\beta$ differential pressure in XZ-plane and $X_o Y_o$-plane, respectively, psid

$\Delta p_{\beta'}$ differential pressure in XY-plane, psid

q_∞ free-stream dynamic pressure, psf

S reference area, sq ft

t time, sec

u, v, w velocity components resolved to body axes, fps

V velocity, fps

X, Y, Z body axes (fig. 30(b))

X_o, Y_o, Z_o space axes (fig. 30(b))

x, y, z coordinate along X-, Y-, and Z-axis (positive in positive X-, Y-, and Z-directions), respectively, in.

x_b axial distance from nose stagnation point, in.

α vehicle angle of attack in XZ-plane, deg

β projection of vehicle angle of attack in $X_o Y_o$-plane into plane of velocity vector, deg

β' vehicle angle of attack in XY-plane, deg ($\beta' = \beta$ when $\alpha = 0$)

ϵ ratio of nozzle exit area to throat area

η total angle of attack, deg

λ nozzle-divergence loss factor

ϕ differential pressure port location from hemispherical stagnation point, deg

VEHICLE DESCRIPTION

Vehicle Staging and Trajectory Sequence

The RAM B launch vehicle was an unguided, three-stage, solid-propellant system. Each stage was aerodynamically stable and spun to reduce dispersion effects. The first stage was a Castor-E8 rocket motor (fig. 1) with two 0.24 KS 9900 Mod. I (Hotseat) spin motors (fig. 2) for initial spin-up. The second stage was an Antares-IA1 rocket motor (fig. 3) and the third stage was a 30 KS 8000 (Alcor) rocket motor (fig. 4). The spin motors were located on the vehicle launch center of gravity with their thrust axis perpendicular to but displaced from the vehicle longitudinal axis. The over-all vehicle length was approximately 42 feet and it weighed approximately 13,300 pounds at launch. Figure 5 is an inboard profile drawing showing pertinent vehicle dimensions and principal hardware sections. Figure 6 is a photograph of the payload and vehicle mounted on a zero-length boom-type launcher. Figure 7 is a composite sequence photograph showing the first 1.2 seconds of vehicle flight during spin motor firing and first-stage spin-up.

The first-stage rocket motor was ignited by ground circuitry through a flyaway umbilical cable. After 1 inch of forward movement, the second and third stages were armed by first-motion switches. After approximately 20 feet of forward movement the first-stage fins were clear of the launcher boom and two lanyard activated switches located at the base of the first stage ignited the spin motors and activated a 0.5-second delay switch. Approximately 0.5 second after spin-motor ignition the delay switch initiated the two explosive bolts on the spin rig harness which were fractured, permitting the spin motors and harness to be spun away from the vehicle in two pieces. The second-stage rocket motor was ignited by a ground-based dualized command system according to radar velocity, position, and attitude information. The third-stage rocket motor was ignited by a dualized second-stage chamber-pressure decay switch.

The first and second stages were stabilized with delta-planform in-line wedge fins. The third stage was flare stabilized. In order to maintain the initial spin rate imparted to the vehicle by the spin motors, the fin tips of the first stage were canted 9° and the fins of the second stage were canted 0.44^{o} in such a manner as to impart a clockwise spin direction when viewed from the launcher.

Stage Hardware

The stage hardware is in general the same as that used in the Blue Scout Jr. launch vehicle. Changes are larger first-stage fins and a new third-stage stabilizing transition section. All of the hardware is of monocoque construction wherein aluminum rings or forgings are covered with fiber-glass panels. This type of hardware was utilized in order to maintain the vehicle weight at a low value compatible with the velocities desired. The vehicle hardware is composed of major sections, each given a letter designation or name. (See fig. 5.)

Base F.- The primary purpose of the base F section was to provide the aft launcher connection and to provide rigid surfaces for fin mounting. Base F section consisted of the shroud and aerodynamic fins which were attached around the nozzle of the first stage (fig. 8). Figure 9 is a drawing of this section showing details of dimensions, assembly, and materials utilized. The fabrication and alinement tolerances of each fin were individually taken into account so that each fin would produce equal rolling moment. Each fin tip was nominally deflected 9° in order to provide a roll rate of about 3 cycles per second at first-stage burnout; the fin leading edges were swept back 45° and were fabricated from 0.071-inch-thick material. A flame seal was installed at the end of the base section to close the gap between the nozzle and the section and to prevent hot gases from being sucked into the section.

Spin rig.- Figure 10 shows the spin rig which was used to spin-up the vehicle. The system was attached to a cylindrical shroud in two halves by explosive bolts. A thin layer of Teflon tape was placed between the spin rig and the shroud to insure proper separation. Each half consisted of two 90° segments hinged together. Locating bosses on the shroud at the vehicle launch center of gravity insured proper positioning of the spin motors and transmittal of the torque to the shroud. The shroud was fixed to the front end of the first-stage rocket motor so that the torque was transmitted properly to the vehicle. The spin rig was a self-contained system and had connections to the blockhouse through two flyaway umbilicals.

C section.- The transition section (C section) joining the first- and second-stage rocket motors was fabricated in two parts (upper C and lower C) and joined by a blowout diaphragm. Lower C section is bolted to the head end of the first-stage rocket motor and contains two access doors for pyrotechnically arming the motor (see fig. 10). Aerodynamic heat protective fairings behind each fin protect wire bundles going from lower C section to upper C section. All vehicle umbilicals enter the vehicle through trap doors in lower C section. Figure 11 is a detailed drawing of C section with all major components.

Upper C section primarily provides second-stage fin mounting attachment points. Each fin is swept back 70° and is deflected 0.44° to obtain a roll rate of about 3 cycles per second at second-stage burnout. The fin leading edge is 0.125-inch-thick steel. Figure 12 shows upper C section with one of the four access doors removed to show the internal components. The vehicle command receivers, relays, junction boxes, and ignition batteries for second- and third-stage ignition are located in upper C section.

Figure 13 shows the second-stage fin trailing edge. A silicone rubber ablative material was applied to the trailing edge for protection from the exhaust plume heating. A fin trailing-edge thermocouple history is discussed subsequently. The electrical separation plugs were protected by a spring-loaded heat protective door to prevent possible plug melting and subsequent electrical short circuit.

G section.- The transition section (G section) joining the second- and third-stage rocket motors is fabricated in three parts and joined by a blowout diaphragm. Figure 14 is a detailed drawing of G section indicating all major components, materials, type of fabrication, and methods of attachment.

Lower G section is bolted to the front end of the second-stage rocket motor and is fabricated in two pieces: a load-carrying structure and a fiber-glass aerodynamic fairing. Vent holes located in the lower G fairing provided pressure relief for the second-stage heat shield and all of the third stage. Figure 15 shows the lower G structure with all flight components installed. The structure serves as a mounting surface for the second-stage motor chamber-pressure transducer and the third-stage ignition-pressure switch, and as a tie point for the electrical separation plug lanyards. Figure 16 shows the complete lower G section attached to the third stage. Figure 17 shows the lower G section aerodynamic fairing removed so that one of the two electrical separation plugs is visible. The electrical plug heat protective cover is designed to protect the plug from the rocket-exhaust plume after stage separation. The second-stage aerodynamic fairing (reverse flare) break wire was installed to verify vehicle continuity until third-stage ignition.

Figure 18 shows the stabilizing flare and third-stage rocket motor. Figure 19 shows the aft end of upper G section (flare closure) with all flight hardware installations. The C-band beacon antenna is inclined 3° to the center line and is covered with a noncharring ablation material. The entire flare closure is covered with cork as protection from the exhaust plume heating. The temperature readings from the flare closure calorimeter are introduced in a subsequent section. The third stage is vented into the lower G section through the flame seal slits and through the electrical disconnect plug door openings.

Heat shields.- Both the second- and third-stage rocket motors require heat protective shields to prevent a loss of strength in the motor chamber walls due to aerodynamic heating. For the third stage the heat shield is also the structural member. The second-stage heat shield is essentially a cork-lined nonstructural fiber-glass unit designed to cover the second-stage motor case, to carry the wiring bundles, and to prevent the motor case from exceeding its temperature limit of 150° F. The shield is made in two halves and joined by external splice plates. Figures 11, 14, and 15 show details of the heat-shield installation. A layer of heat reflective and radar reflective aluminum foil was also placed on the outside motor wall facing the heat shield.

The third-stage heat shield is a structural fiber-glass unit providing heat protection for the third-stage motor and wire bundles (fig. 18). The shield is made in two halves and joined by internal splice plates with the exposed screw heads covered by a 0.1-inch-thick layer of cork.

As previously indicated, provision for venting the second stage is provided in the fairing of lower G section. Venting was required because of the structural design limits. The external pressure existing on the heat-shield surfaces changed at rapid rates due to the trajectory and local flow dynamics. As a result of this rapid pressure change, sufficient venting was necessary to maintain the difference between the internal and external pressures below the design limits of the structure for either a collapsing or bursting condition. Figures 14, 17, and 20 show the venting path. Vent holes were put in the attachment rings at stations 49.50 and 92.69 (fig. 5) to vent the forward end of the third stage to the flare. The electrical plug heat protective door vented the flare to the area under the lower G fairing. The second-stage heat shield is

vented to the lower G fairing through the wiring tunnels. Upper C is sealed from the heat shield and is vented through local surface holes.

Payload

The payload was a hemispherically blunted cone cylinder approximately 67 inches long and bolted to an attached ring at the front end of the third-stage rocket motor (figs. 5 and 21). Figure 20 is a detailed drawing of the structure common to all RAM B payloads. Figure 21 shows the payload mounted on the third stage and the location of the umbilical door. Figure 22 shows the payload mounting ring and accelerometer and pressure transducer installation on the front end of the third-stage rocket motor. In general, the payload structure consists of an aluminum skin supported by aluminum rings with an outside covering of heat protective noncharring ablation material. The aluminum substructure was fabricated to specification and the ablation material was applied by spray technique and machined to a thickness which decreased in proportion to the distance from the hemispherical nose. The hemispherical nose and approximately first 14 inches of the cone were machined from beryllium. Beryllium was selected for this experiment because of its high thermal conductivity which provided assurance that the material would not melt for the anticipated temperature environment.

Vehicle Electrical System

The vehicle electrical system was designed to be as safe and reliable as practical for personnel hazard protection. In general, redundant systems were utilized throughout the vehicle, so that the operation of either or both as a complete system or system component would insure success. All pyrotechnic devices contained redundant initiators connected to separate power sources. All ignition wiring was redundant. Redundant spin motor ignition switches were utilized as were second-stage first-motion arming switches, command receiver system components, and third-stage ignition pressure switches. Command receiver components, batteries, antennas, and receivers were redundant and independently monitored up to lift-off. Remote pyrotechnic arming, monitoring, and continuous resistivity checks were provided by console instrumentation in the launch control blockhouse. Other instrumentation provided monitoring of all batteries (activated or not activated), various temperatures, and safe or arm condition. Electrically activated inert batteries were installed for all ignition systems. The spin motor batteries were remotely charged from the blockhouse and the second-stage ignition batteries were pyrotechnically activated near launch. Manually activated batteries were installed for the command receiver, payload, and C-band beacon.

Thermal Protection

Thermal protection was necessary because of two significant types of heating: aerodynamic, caused by shocks and skin friction, and impinging rocket-exhaust plume, caused by underexpanded rocket nozzle exhausts coming into contact with adjacent surfaces. The first-stage fins were swept back 45° with the

7

leading edges formed from 0.071-inch-thick 4130 steel and having 0.25-inch radius for thermal protection of the leading edge. The second-stage fins were swept back 70° and capped with 0.125-inch-thick high-temperature superalloy steel forming a 0.15-inch-radius leading edge. Both sets of fins had fiber-glass surface panels to protect the aluminum substructure castings from heating. The trailing edges of the second-stage fins were protected from jet plume heating by a 1/8-inch-thick hand-applied coating of silicone rubber. This thickness was estimated to be more than adequate even though no plume heating data were available for the particular rocket motor, trajectory, and hardware involved. The second-stage rocket-motor heat shield (figs. 11 and 14) was a nonstructural 0.05-inch-thick fiber-glass cylinder lined with 0.25-inch-thick high-density cork. The application of the insulative cork to the inside of the fiber-glass shield prevented collapse of the heat shield onto the motor case due to aerodynamic loading, stiffened the shield and made it more resistant to flutter, and gave increased assurance that the case temperature limit of 150° F would not be exceeded. Liberal use was made of the cork on the third-stage flare. The cork was found to be superior to most other easily applied economical materials when compared on the basis of insulating efficiency per pound. Reference 7 presents more information on the cork and its characteristics. The 13° half-angle flare face was covered with 0.2-inch-thick cork applied in two equal thickness layers of three gores each. The cork was vacuum bonded to the prepared aluminum substructure with a high-temperature epoxy adhesive. A single layer of 0.15-inch-thick cork was applied to the flare closure to protect the flare supporting structure from the jet exhaust plume. A special disk of noncharring ablation material was bonded to the C-band beacon antenna face to protect it from heating. This material was required in place of the charring cork in order not to change the antenna characteristics. The third-stage heat shield was a structural 0.10-inch-thick fiber-glass member designed to maintain its load-carrying capability under high heating as well as to provide thermal protection for the rocket-motor case.

Thermal considerations determined the design of the payload shell. Approximately 30 percent of the total payload weight was allotted to thermal protection of the payload substructure and instrumentation throughout the total flight. Beryllium was required for the hemispherical nose tip to insure a high-heat conductivity away from the stagnation region without melting so that all pressure orifices would remain intact. The noncharring ablation material was required because of its high ablation temperature characteristics.

Vehicle Mass Properties

Time histories of the vehicle weight, center of gravity, pitch or yaw mass moment of inertia, and roll mass moment of inertia are presented in figures 23, 24, 25, and 26, respectively, for all stages of the flight configuration. As indicated in the figures, there are very few measured vehicle mass characteristics because of the practicality of accurately measuring the quantities for large masses. The calculated values were based on both calculated and measured mass properties of the rocket motors, vehicle hardware, and payload. The weight and center-of-gravity location for all vehicle components or assembled components were determined separately. These results were combined for each vehicle stage, and these values were combined to establish total and intermediate stage values

of weight and center of gravity. All vehicle components were weighed separately, and the center-of-gravity location and weight were determined for the stages assembled as completely as possible. The absence of suitable facilities prevented determination of all except the payload-stage inertias. Table 1 presents the actual static component weight breakdown. Table 2 gives a calculated dynamic flight weight breakdown.

Vehicle Aerodynamic Characteristics

Mach number variations of stage center of pressure, normal-force coefficient, and axial-force coefficient are presented in figure 27. All stage aerodynamic data have been derived from detailed wind-tunnel tests (refs. 8 and 9). Figure 27(a) presents the first-stage longitudinal aerodynamic characteristics and center-of-gravity variation with Mach number. Aeroelastic analysis has shown that the minimum static margin in the flexible vehicle is 27 inches, which is a decrease of 6 inches in the rigid-vehicle static margin. Figure 27(b) presents the variation of the second-stage longitudinal aerodynamic characteristics with Mach number. Figure 27(c) gives the variation of the third-stage longitudinal aerodynamic characteristics with Mach number. The wind-tunnel static stability results indicated that this stage would be statically unstable at low angles of attack due to the rocket jet pluming reducing the flare effectiveness to nearly zero. However, the tunnel results also showed recovery of flare effectiveness at high angles of attack, resulting in a trim angle other than 0°. For the preflight nominal trajectory chosen, the trim angle was 6°; however, in the actual flight the altitude history was lower on the average for third-stage operation and, consequently, the pluming was not as severe. The vehicle was statically stable for all angles of attack above approximately 2^O rather than 6° as shown in figure 27(c).

TRAJECTORY PROGRAMING AND IN-FLIGHT COMPENSATION

Perhaps the most unique aspect of the RAM B flight series is the requirement for assuring accurate altitude and flight-path-angle conditions at third-stage burnout. In order to approach such a requirement without a control system, it is necessary to make the assumption that the second and third stages will fly a ballistic trajectory and have a predictable velocity increment. Then, this assumption permits one to control second-stage ignition time to compensate for first-stage velocity errors and effective launch-elevation-angle errors which are caused by winds, thrust misalinement, and fabrication tolerances. There is a twofold reason for this accurate altitude and attitude placement capability. The payload must experience an amount of attenuation sufficient for accurate measurements, but not too much to cause radio blackout and not too little to mask the fact that the attenuation is truly plasma-sheath attenuation. Secondly, there must be a sufficiently positive flight-path angle at third-stage burnout to assure that the payload ascends above the attenuation region to insure that all data recorded during the blackout region can be transmitted to ground stations.

Wind Compensation

The majority of angular dispersions observed in low launch acceleration vehicles are caused by winds. In the RAM B flights the required low launch elevation angles would not permit neglecting wind effects because this would have caused as much as a 20° change in launch azimuth and a 3° change in effective launch elevation angle. The potential azimuth errors would have made range safety and downrange tracking impossible. The elevation errors were greater than could be compensated by a variable second-stage ignition technique. A detailed wind-tunnel study of the vehicle aerodynamic characteristics (ref. 8) was undertaken to permit accurate utilization of existing wind compensation techniques. The wind compensation technique of reference 10 was utilized. Success with the technique during two launchings has been acceptable. It should be noted that the adequacy of this compensation technique is largely dependent upon ability to accurately measure launch wind and to predict the vehicle's response to that wind.

Second-Stage Command Ignition

In order to compensate for first-stage velocity and elevation-angle errors which accumulate during first-stage thrusting, a method of trajectory control which incorporates ground command ignition of the second stage from plotboard presentations has been developed. Basically, the technique requires that a velocity increment - higher or lower than nominal - be determined at a time prior to the time when command ignition will occur. By utilizing this velocity increment and particle ballistics, it is possible to select a combination of flight-path angle and altitude where second-stage ignition should occur to give a desired third-stage burnout altitude. The technique essentially compares nominal velocity with actual flight velocity at first-stage maximum velocity (the most easily defined comparison point) and then a combination of that velocity increment and the actual flight path (altitude and flight-path elevation angle) determine when to command ignition of the second stage. Is is obvious that this technique depends upon an accurately predictable flight of the remaining two stages. Reference 11 presents a detailed description of the technique.

The ground equipment associated with the trajectory control technique consisted of the FPS-16 radar (the most accurate Wallops radar), two radar plotboards, real-time analog differentiating equipment, the FRW-2 ground command transmitter, and a relay unit and command ignition switch at the radar plotboard. The FPS-16 had an analog differentiator connected in parallel with the existing circuit so that it was possible to display real-time velocity, altitude, and flight-path angle in the vertical plane of the trajectory.

The vehicle onboard equipment utilized in the command ignition consisted of dualized DRW-13 receiver components and a C-band transponder. It was possible to command ignition or cause no ignition of the second stage and to command no ignition of the third stage. In this respect the command ignition system served as a passive range safety device.

INSTRUMENTATION

Vehicle

The payload FM/FM telemeter transmitted 15 continuous channels and 2 channels of commutated data at 2.5 cycles per second; only part of these channels were for vehicle instrumentation. A total of 75 measurements were made of transverse acceleration, thrust and drag acceleration, skin temperatures, differential pressure for angle of attack, vibration, sun detector (roll rate and roll attitude), motor chamber pressures, antenna efficiency, and conditions of the material injected into the flow field. Figure 28 presents segments of a typical telemetry oscillograph record showing the time intervals associated with ignition of each stage. Each telemetry oscillograph record was set up to have three sets of reference and timing traces to permit accurate reading of the data. The primary vehicle performance parameters measured are shown in this figure. The instrumentation of primary concern in this report is that for the vehicle motion and environmental measurements. Table 3 presents the continuously transmitted vehicle quantities and the location of the instruments with respect to the third-stage burnout center of gravity. Figure 20 shows the location of the principal vehicle motion instrumentation. Figure 22 is a photograph which shows mounting details of the accelerometers and third-stage motor chamber pressure transducers. Table 4 presents the location of the vehicle thermocouples, the commutated switch position, and the thickness of the material by which the thermocouple was thermally shielded. Figure 29 is a sketch of the second stage showing the relative location of all the thermocouples.

The thermocouples were installed primarily to verify the adequacy of the thermal protection materials and secondarily to determine the thermal environment and thermal efficiency of the protective materials. Thermocouple measurements were made of the temperatures of the inner wall of the conical beryllium nose and the conical and cylindrical payload structure covered with noncharring ablation material, the temperatures of the free air surrounding the second- and third-stage chamber forward and after dome, the temperatures of the second-stage fin leading and trailing edges, and the temperature of the third-stage flare inner wall. An extremely sensitive asymptotic-type calorimeter gave a measure of the heating rate on the third-stage flare face. A relatively slow-response slug-type calorimeter gave a measure of the heating rate on the third-stage flare closure caused by rocket-exhaust plume radiative and convective heating. All thermocouples measuring back-wall temperatures were resistance welded to the metal surfaces and the free-air thermocouples were formed by joining the two thermocouple elements into a bead whose diameter was approximately equal to double the element gage.

Thrust and drag acceleration were measured by two accelerometers whose ranges were from 25g to -3g for thrust and ±2g for drag. These instruments served as accurate event markers, and with the combination of motor chamber pressure transducers on the second and third stages thrust and coast drag coefficients were determined. One transverse accelerometer was located in the payload so as to obtain an acceleration correlation with the vehicle rate of change of angle of sideslip. It was not possible to mount the accelerometers at a center-of-gravity position because this position varied through the boosted portions of

the flight (figs. 20 and 22). Consequently, the accelerometers were located so that angular accelerations and accelerations due to angular velocity would be small and, therefore, the corrections for the vehicle center-of-gravity displacement would be small.

A single high-frequency telemetry channel was used to monitor longitudinal vibration experienced at the forward thrust ring of the third-stage rocket motor. The vibrometer was attached to one mounting bolt and was sensitive to the acceleration history of each motor. The primary purpose of the vibrometer was to obtain vibration data on the Alcor motor.

The differential pressure orifices were located in pairs 180° apart on the hemispherical nose so that the ports in each plane were 45° on either side of the longitudinal axis (fig. 20). The calibration of the differential pressure cells over a ± 1.0 psid range was found to be linear and free of hysteresis effects with the pressure cells capable of 100-percent overload without affecting the characteristics of the instruments. Figure 30 shows the conventional aerodynamic axis system for the vehicle and the third stage and indicates the angles measured.

A sun detector consisting of essentially a photocell covered by a narrow aperture quartz window was mounted in the payload conical section perpendicular to the vehicle longitudinal axis. Roll rate and roll position were determined from data obtained by this instrument. It was necessary to know vehicle roll position in order to analyze the effects of the vehicle antenna patterns on the observed signal attenuations. Roll rate was also determined from ground-based cameras and from received signal strength measurements.

Ground Range

The payload telemetry data were received by recording stations at the NASA Wallops Station, Langley Research Center, Coquina Beach, North Carolina, a mid-ocean tracking ship, and Bermuda. Each station recorded telemetered data as well as received signal strengths for signal attenuation analysis. Figure 31 shows the relative location of these stations to each other and to the vehicle ground track. The vehicle was tracked by the Wallops radars - SCR-584, modified SCR-584, FPS-16, SPANDAR, and M.I.T. S-band radar located on the mainland - to the limit of each respective unit's range. All radars provided real-time displays of space position in terms of azimuth, flat-earth altitude, and flat-earth range, and the FPS-16 in addition provided planar velocity and flat-earth flight-path elevation angle. The payload stage was also tracked for a 20-second interval by the Bermuda Coopers Island FPS-16 radar.

Wind and atmospheric conditions were determined by means of ground-based anemometers, FPS-16 tracked chaff balloons, theodolite tracked balloons, and rawinsondes launched near the time of flight and tracked by a GMD-1A rawin set to an altitude of approximately 80,000 feet. An attempt at obtaining atmospheric conditions above this altitude by rocket-borne instrumentation was not successful. Three special vehicle-tracking theodolites were used in the first 15 seconds of the vehicle flight to determine the precise manner in which the

vehicle reacted to the surface winds and to determine and help explain any unexpected deviations in vehicle launch elevation or azimuth.

Accuracy

The measured temperatures presented in the figures are considered to be accurate to within ±2 percent. It should be noted that the thermocouple is considerably more accurate than ±2 percent and the main error source is due to the telemeter system. The differential pressure measurements are considered to be accurate within ±2 percent of the calibrated full-scale range of the pressure cell, giving an accuracy of ±0.04 psid. The angles of attack are also inversely proportional to stream dynamic pressure which includes stream density and velocity accuracies. The resultant angular error is approximately ±0.25° during the third-stage thrust portion of the flight. The space position, velocity, and flight-path-angle data obtained from reduced data of the most accurate radar (FPS-16) are considered to be accurate within 50 feet, 50 feet per second, and 0.5°, respectively, during third-stage thrusting.

FLIGHT RESULTS AND DISCUSSION

Trajectory Sequence of Events

The RAM B2 vehicle was launched at 64.8° elevation and 95.5° azimuth to compensate for existing winds and to follow effective 65° launch elevation and 102° azimuth angles. The sequence of trajectory events is presented in table 5. The vehicle weighed approximately 13,300 pounds at launch and had an initial longitudinal acceleration of approximately 4.5g.

The first stage was given an initial spin rate of approximately 2.8 cycles per second by the two spin motors. The spin motors and their support harness were high-drag additions to the first stage and were therefore separated by centrifugal force from the vehicle (being released by two explosive bolts at 1.3 seconds after launch).

The first-stage motor burned out at an altitude of approximately 50,000 feet at about 38.5 seconds and coasted for about 12 seconds (nominal coast time was 16 seconds) at which time the second stage was ignited by ground command. The first stage was separated by a blowout diaphragm upon ignition of the second stage. Ignition of the third stage occurred when the second-stage chamber pressure dropped to 50 psia. The third stage also was separated by a blowout diaphragm from the second stage and burned out at an altitude of approximately 162,000 feet. Payload apogee was approximately 290,000 feet and impact was approximately 1,000 international nautical miles downrange.

Figure 32 presents a comparison of the actual and expected altitude-velocity profile for the RAM B2 vehicle. Figure 33 shows the entire altitude—horizontal-range trajectory with primary events noted. For all trajectory data presented in this figure the primary source is the Wallops FPS-16 radar; these data appear as a solid trace with other radar data shown by symbols. The dashed

13

part of the curve after 200 seconds represents a postflight computer trajectory extension. Even though the FPS-16 radar tracked more than 200 seconds, the radar-antenna elevation angle was very low with the result that ground noise caused the data to be less accurate than normal. Consequently, it was necessary to take end conditions from the FPS-16 radar data and adjust them slightly within their accuracy band in order to produce a trajectory extension which would reasonably match the Bermuda data. All radar data were reduced by an electronic computer and referenced to the 1962 spheroid of reference 12. Time histories of altitude, horizontal range, velocity, Mach number, and flight-path angle with comparisons from various sources are presented in figures 34, 35, and 36. Figure 37 presents the FPS-16 radar received signal strength on automatic beacon track mode as a function of slant range. It is of interest to note that the received signal is lower during second-stage flight than when vehicle track was lost (225 seconds at approximately 410 international nautical miles), indicating that vehicle tracking stopped because of low elevation angle rather than because of inadequate beacon signal return.

Vehicle Environmental Conditions

Figures 38, 39, 40, and 41 present the altitude variations up to approximately 80,000 feet of density, pressure, temperature, and speed of sound, respectively, as determined from a rawinsonde launched just prior to the flight. The respective quantities from the ARDC 1959 Standard Atmosphere (ref. 13) up to 200,000 feet altitude were used for all data reduction purposes and are shown for comparison. An attempt to obtain upper altitude characteristics by rocket-borne instrumentation was unsuccessful.

Figure 42 is a time variation of free-stream dynamic pressure and figure 43 is a Mach number variation of Reynolds number based on the FPS-16 data.

Figures 44 and 45 present altitude variations of the wind azimuth and velocity as determined from various prelaunch radar balloons and ground measurements. The technique of reference 10 has been utilized to divide the altitude range up to approximately 32,000 feet into 20 layers, as indicated in the figure, so that the vehicle's total wind sensitivity over the altitude range is 5 percent for each layer. Two fairings appear in the figures. The straight line is the ballistic value of wind velocity or azimuth - that is, the weighted average over the range of sensitive altitude. The straight-line segments indicate the averaged values through the altitude layers and would be used in actually making vehicle loads studies. Figure 46 shows details of wind and azimuth at the lower altitudes. From this figure it can be seen that the vehicle passes through 50 percent of its wind sensitivity by approximately an altitude of 1,800 feet.

Accelerations

Figure 47 shows the flight-measured longitudinal accelerations. These data are taken from the high-range and low-range accelerometers and have not been corrected to the vehicle instantaneous center of gravity. The primary purpose of the high-range longitudinal accelerometer was to help determine velocity in the event of radar malfunction and to monitor individual stage performance.

14

Data from the low-range accelerometer are presented during third-stage coast. The maximum longitudinal acceleration occurred just prior to third-stage motor tail-off and was approximately 22g. Data from the high- and low-range longitudinal accelerometers were in good agreement during coast periods of flight.

Figure 48 shows the flight-measured transverse acceleration history. These data have not been corrected to the vehicle instantaneous center of gravity. The instrument had a range designed to measure gross vehicle motion and, consequently, does not have the desired accuracy for making detailed interpretations of the observed data. However, it is obvious that the vehicle experienced a disturbance at second-range ignition which was rapidly damped. At third-stage ignition there was an instantaneous disturbance on the accelerometer record which did not appear to cause any vehicle angular oscillation. Later during third-stage thrusting the accelerations became divergent, resulting from the jet-plume instability at low angles of attack. At approximately 110 seconds the divergent pattern of the acceleration data is disturbed by material injection which apparently disturbs the vehicle enough along with the now decreasing jet-plume instability to cause the vehicle to oscillate between stable and unstable angles of incidence. The transverse acceleration becomes more negative with time since the coning angle increases.

Figure 49 shows a qualitative picture of the flight-measured longitudinal vibration data at the forward thrust face of the Alcor rocket motor. A detailed spectral analysis of the data has indicated that this figure gives an accurate quantitative idea of the motor operating conditions. A high-frequency vibrometer was mounted on an Alcor motor payload attachment ring bolt and was primarily for the purpose of obtaining in-flight data on the Alcor motor. Vibrations measured before Alcor thrusting are attenuated by the interconnecting structure and, consequently, they did not create any serious vibrational problems for the payload structure. Even with the attenuated vibrations, it is obvious that the second-stage rocket motor imposes the more severe longitudinal vibration problem for the payload. The frequency response of the vibration data presented in figure 49 is limited by the 5,000-cps galvanometer and the 1050-cps filter of the discriminator.

Motor Chamber Pressures

Figure 50 shows the second- and third-stage-motor chamber-pressure histories as obtained by pressure transducers mounted on the forward end of each motor. The chamber-pressure measurements were telemetered on one continuous channel and were electrically interconnected in such a manner that only one transducer was instantaneously providing input to the telemeter. Figures 51 and 52 show the in-flight thrust levels derived from the chamber-pressure measurements compared to motor nominal thrust corrected for flight altitude. These flight chamber-pressure data were converted to thrust by

$$F = \lambda A_t C_d C_F p_c \tag{1}$$

where C_d, the discharge coefficient, was determined by ground static tests and A_t and λ were constants ($\lambda = 0.983$, $C_d = 0.981$, and $A_t = 26.06$ sq in. for

15

Antares and $\lambda = 0.99$, $C_d = 0.972$, and $A_t = 9.73$ sq in. for Alcor) determined by the preflight nozzle geometry. The thrust coefficient C_F was determined as a function of nozzle expansion ratio, ambient and chamber pressures, and assumed equilibrium real-gas exhaust properties. The thrust level and characteristics for the Antares motor showed a greater deviation from the nominal value than was expected. The time required to reach third-stage ignition pressure was approximately 1.5 seconds longer than expected since the temperature at which the motor was ignited was 83° F. In addition, the total impulse was approximately 0.65 percent lower than the nominal. The third-stage thrust level was higher than expected and burning time was approximately 1 second less than the nominal value. Total impulse of the third stage was approximately 3 percent lower than nominal. It should be noted that the third-stage throat area increases by 6.6 percent (determined from static firings) during burning, a factor which has not been accounted for in deriving thrust from pressure.

Roll Rates

The first-stage fin tips were deflected 9° and the second-stage fins were canted 0.44° to impart a positive (clockwise in direction viewed from launcher) roll rate of 3 cycles per second to the vehicle. The roll program was employed to negate the effects of fabrication tolerances, roll resonance problems associated with low roll rates, in-flight disturbances, and thrust misalinements. Gyroscopic stabilization did not become a noticeable force until approximately 30 seconds after third-stage burnout. Aerodynamic forces were predominant up until that time and caused the vehicle to fly essentially a ballistic trajectory.

Figure 53 shows the time history of the flight roll rate as determined from various instrumentation. It can be easily seen that roll rates determined from signal strengths recorded at various widely separated ground stations agree well with the onboard sun detector instrument which was considered the most accurate. Sun detector data in the early portion of flight before the vehicle passed the low-flying clouds are well correlated by ground-based tracking cameras. Figure 54 gives a comparison of the roll frequency with the body-bending frequency computed by the technique of reference 14 and the nonrolling body pitch natural frequency. The requirement that the roll frequency not remain at either the first bending or pitch natural frequency for any length of time because of divergency problems determined the roll program. It was desired that the first stage reach a roll rate before burnout of 3 cps and that the second stage maintain that value of roll. A lower but acceptable value of roll rate was attained at first-stage burnout and the second-stage fins correctly caused the roll rate to reach a burnout value of approximately 3 cps. During third-stage burning there is a small roll-rate increase due to motor thrusting. This phenomenon is not unexpected and is discussed in reference 15.

Skin Temperatures

As many vehicle and payload locations as possible were instrumented with temperature-measuring devices for the purposes of verifying design adequacy, providing malfunction data, evaluating material efficiencies, and providing data

unique to the particular configurational geometry or experiment. Figure 55 shows histories of the temperatures measured at the back wall of the payload skin. Table 4 and figure 29 more accurately define the thermocouple locations and material type and thickness. The thermocouples are referred to by telemeter channel switch position (hereinafter referred to as S.P.). In figure 55(a) there is a noticeable cooling effect shown by the data subsequent to initiation of the experiment at 110.03 seconds. The primary cause for the greatly different curve shapes after 110 seconds is due to the experiment. Figure 55(b) shows that all stations covered by the noncharring ablation material experienced very little temperature rise and that the thermal protection was adequate.

Figure 56 shows the temperature history for the second-stage-fin leading and trailing edges. Figures 13 and 29 and table 4 provide an accurate description of the thermocouple locations. The fin leading-edge temperature history indicates an adequate design since the $1,800^\circ$ F strength limit of the steel leading edge was not exceeded. An area of uncertainty was encountered in predicting the fin trailing-edge temperature history because the effects of jet-plume expansion heating were not known. The solution was to apply a thermal protection material and verify its adequacy. Up to 51 seconds the effects of aerodynamic base heating are observed. As indicated by the curve at 51 seconds, there is an instantaneous effect of motor ignition and jet-plume growth.

Figure 57 shows time histories of the second- and third-stage forward and after chamber dome free-air temperatures. The third-stage after dome free-air thermocouple showed an unexpected rise in temperature at third-stage ignition. The probable cause of this high temperature is that the third-stage flame seal (figs. 14 and 19) failed and hot exhaust gas was sucked into the low-pressure nozzle region. There was no other indication that this malfunction produced other effects.

Figure 58 shows the flare-closure temperature and heating-rate history produced primarily by the Alcor motor burning. As for the second-stage-fin trailing edge, the total effect of plume heating was unknown for this particular geometry, motor, and altitude regime. For the Alcor the jet plume was considerably larger than for the Antares and the whole flare closure was expected to be immersed in the initial expansion. The data were obtained from a slug-type inconel calorimeter whose properties were determined before flight.

Figure 59 shows temperature and heating-rate histories from instrumentation designed to determine the efficiency of the cork thermal protective material on the flare face. Thermocouple S.P. 22 is the history for the back wall of the flare, and S.P. 24 is the history for the temperature midway (0.1 inch) between the flare cork covering (fig. 59(a)). As can be seen, there is considerable lag through the material and the cork prevented the aluminum substructure from exceeding 400° F until after the data period. Reference 7 presents a more detailed analysis of the cork material. Figure 59(b) shows the flare-face heating rate as determined from the temperature history of an accurately calibrated constantan-foil calorimeter. The temperature history was obtained from a copper-constantan conversion table. The calorimeter had extremely fast response and showed considerable sensitivity to the experiment. Once again the effects of cooling are noticeable from the slope of the heating-rate curve before experiment initiation and the general slope thereafter. The manner in

17

which the curve is plotted is considered to be accurate and to be a direct result of the experiment. The rates of change should be accurate because the telemeter calibrations which were recorded every 0.4 second showed no deviation, indicating that the telemeter accuracy level was not changing.

Angle of Attack

Wind-tunnel tests on cones and spherical noses having angle-of-attack meters (refs. 16, 17, and 18) have shown that differential pressures can be accurately used to determine angle of attack over a wide range of Mach numbers. Although the expressions used for computing angle of attack were derived from hypersonic impact theory, references 16 to 18 show that the method also may be employed at supersonic Mach numbers at a relatively small error penalty. Reference 17 shows that the optimum location for each differential pressure orifice is on a 45° radius vector measured from the vehicle longitudinal axis. The RAM B payload orifices are located at the optimum position, $\phi = \pm 45^\circ$.

The angle of attack of the body to the relative wind was measured in two components, α and β'. These angles were determined from the differential-pressure histories of a pair of orifices which were interconnected in such a manner that the angle of incidence was directly proportional to the differential pressure. The expression for computing angle of incidence from differential-pressure data is based on Newtonian impact theory where $C_{p,t}$ varies up to an asymptotic value of 1.84 for Mach numbers greater than approximately 10. References 16 to 18 have also shown that the differential-pressure measuring devices have good accuracy into the low supersonic range. The equations used to determine differential pressures are as follows:

$$\Delta p_\alpha = C_{p,t} q_\infty \sin 2\phi \sin 2\alpha \tag{2}$$

$$\Delta p_{\beta'} = C_{p,t} q_\infty \sin 2\phi \sin 2\beta' \tag{3}$$

Figure 30 shows the vehicle axis system and defines the positive directions. Figure 20 shows the relative location of the payload differential-pressure orifices. In defining the aerodynamic symbols it was discovered that the angles measured are the conventional α but not the conventional β, but

$$\tan \beta = \tan\left(\frac{1}{2} \sin^{-1} \frac{\Delta p_{\beta'}}{C_{p,t} q_\infty}\right) \cos \alpha \tag{4}$$

$$\tan \beta = \tan \beta' \cos \alpha \tag{5}$$

For purposes of this report the angle measured is referred to as β', and for small or zero values of α, $\beta = \beta'$.

18

Figure 60 shows the α, β', and η histories up to 150 seconds. The total angle of attack η is defined by

$$\cos \eta = \cos \alpha \cos \beta \qquad\qquad (6)$$

As indicated by figure 60 the angle of attack has large variations before 10 seconds due to ground winds. The next interval of angular disturbance occurs at second-stage ignition and is caused by nonsymmetrical tipoff forces. As is evident from the converging angular envelope the vehicle is dynamically stable and the time required to damp to one-half amplitude is approximately 5 seconds. At third-stage ignition there is no perceptible angular disturbance, but subsequent to ignition the expansion of the jet plume causes the body trim angle to change from a small angle of attack (approximately 0.5°) to a larger angle of attack (approximately 2°). The effects of jet pluming on stability for this configuration have been extensively studied in a series of wind-tunnel tests (refs. 9 and 19) and analyzed for similar vehicle flight tests (ref. 20). At 110 seconds the experiment was started and the angular motions were amplified; during periodic intervals the data were meaningless because of experiment interaction with the differential-pressure orifices. Angle of attack beyond 150 seconds is not presented because of the accuracy of the angular value. For example, at 180 seconds the accuracy is ±6° due only to differential-pressure sensor error. Consideration of the dynamic-pressure error would cause the accuracy band to be larger. Examination of the data beyond 150 seconds has shown that the vehicle became gyroscopically stabilized at approximately 150 seconds. It should be noted that the absolute angular values in the region beyond 150 seconds are in greater error than the differential-pressure sensor error, indicating that the dynamic-pressure history used for data reduction was too low for this altitude region.

Figure 61 is included to show some of the characteristic motions of the vehicle during intervals of significance. Figure 61(a) begins at second-stage ignition and follows through to one-half of the original angular amplitude. The motion is epicycloidal with inside loops which was expected since the vehicle was designed for rolling above resonance (ref. 21). The resultant angle initially is approximately 3° and decreases to 1.5° in 5 seconds. The magnitude of the initial loops indicates the amount of aerodynamic force required to overcome the disturbing forces due to stage separation. Figure 61(b) shows the time interval before and after third-stage ignition. Figure 61(c) shows that the type of epicyclic motion during maximum jet-pluming interference is a series of overlapping circles; figure 61(d) shows the motion to have been disturbed from the concentric circles into circles with inner loops.

CONCLUDING REMARKS

A general description of the flight performance of the second flight of the RAM B vehicle has been presented. The purpose of the B series flights was to probe the radio blackout region, to correlate and modify present ionization attenuation theories, and to test the effectiveness of methods for overcoming signal attenuation.

The RAM B vehicle fulfilled its intended mission requirements. The flight results showed that the over-all vehicle structural design, heat shielding, and payload-stage configuration survived the unique conditions associated with the high-temperature environment and the effects of jet pluming on vehicle performance during the flight.

The vehicle successfully followed the approximate nominal trajectory and achieved a velocity of 17,860 feet per second at an altitude of 162,000 feet. An apogee of 290,000 feet was attained to permit data recovery.

Flight data discussed included velocity, altitude, accelerations, and roll rates. Angle-of-attack histories and temperature histories of some vehicle components were also discussed but were not analyzed.

Langley Research Center,
    National Aeronautics and Space Administration,
        Langley Station, Hampton, Va., May 12, 1964.

REFERENCES

1. Levine, Jack: Performance and Some Design Aspects of the Four-Stage Solid-Propellant Rocket Vehicle Used in the RAM A1 Flight Test. NASA TN D-1611, 1963.

2. Cuddihy, W. F., and Hughes, J. Kenrick: Simulated Reentry Tests of a Method for Reducing Radio Blackout by Material Addition to Ionized Flow Field. NASA TM X-988, 1964.

3. Russo, F. P., and Hughes, J. K.: Measurements of the Effects of Static Magnetic Fields on VHF Transmission in Ionized Flow Fields. NASA TM X-907, 1964.

4. Ellis, Macon C., Jr., and Huber, Paul W.: Radio Transmission Through the Plasma Sheath Around a Lifting Reentry Vehicle. NASA TN D-507, 1961.

5. Graves, George B., Jr., and Markley, J. Thomas: Telemeter Transmission at 219.5 Megacycles From Two Rocket-Powered Models at Mach Numbers up to 15.7. NACA RM L58D18a, 1958.

6. Cuddihy, William F., Beckwith, Ivan E., and Schroeder, Lyle C.: RAM B2 Flight Test of a Method for Reducing Radio Attenuation During Hypersonic Reentry. NASA TM X-902, 1963.

7. Graves, Randolph A., Jr., and Walton, Thomas E., Jr.: Free-Flight Test Results on the Performance of Cork as a Thermal Protection Material. NASA TN D-2438, 1964.

8. Kelly, Thomas C., and Keynton, Robert J.: Longitudinal Aerodynamic Characteristics and Surface Pressure Measurements for a 1/10-Scale Model of the RAM B Launch Vehicle. NASA TN D-2204, 1964.

9. Hinson, William F., and Falanga, Ralph A.: Effect of Jet Pluming on the Static Stability of Cone-Cylinder-Flare Configurations at a Mach Number of 9.65. NASA TN D-1352, 1962.

10. James, Robert L., Jr., and Harris, Ronald J.: Calculation of Wind Compensation for Launching of Unguided Rockets. NASA TN D-645, 1961.

11. Norman, J. R.: Pre-Flight Planning Trajectory Data for the RAM B Vehicle. Rep. No. 23.40 (Contract No. NAS1-1113), Astronautics Div., Chance Vought Corp., 1962.

12. Jensen, Jorgen, Townsend, George, Kork, Jyri, and Kraft, Donald: Design Guide to Orbital Flight. McGraw-Hill Book Co., Inc., 1962.

13. Minzner, R. A., Champion, K. S. W., and Pond, H. L.: The ARDC Model Atmosphere, 1959. Air Force Surveys in Geophysics No. 115 (AFCRC-TR-59-267), Air Force Cambridge Res. Center, Aug. 1959.

14. Alley, Vernon L., Jr., and Gerringer, A. Harper: A Matrix Method for the Determination of the Natural Vibrations of Free-Free Unsymmetrical Beams With Application to Launch Vehicles. NASA TN D-1247, 1962.

15. Martz, C. William, and Swain, Robert L.: Experimental and Analytical Study of Rolling-Velocity Amplification During the Thrusting Process for Two 10-Inch-Diameter Spherical Rocket Motors in Free Flight. NASA TM X-75, 1959.

16. Swalley, Frank E.: Measurement of Flow Angularity at Supersonic and Hypersonic Speeds With the Use of a Conical Probe. NASA TN D-959, 1961.

17. Beecham, L. J.: The Hemispherical, Differential Pressure Yawmeter at Supersonic Speed. R. & M. No. 3237, British A.R.C., 1961.

18. Roberts, B. G.: Static Response of a Hemispherical-Head Differential Pressure Incidencemeter: An Extension of the Calibration to 30° Incidence and M = 2.75. Tech. Note HSA 72, Weapon Res. Establishment, Australian Defense Sci. Service, Jan. 1961.

19. Falanga, Ralph A., Hinson, William F., and Crawford, Davis H.: Exploratory Tests of the Effects of Jet Plumes on the Flow Over Cone-Cylinder-Flare Bodies. NASA TN D-1000, 1962.

20. Hinson, William F., and Hoffman, Sherwood: Analysis of Jet-Pluming Interference by Computer Simulation of Measured Flight Motions of Two RAM A Fourth Stages. NASA TN D-2018, 1963.

21. Nelson, Robert L.: The Motions of Rolling Symmetrical Missiles Referred to a Body-Axis System. NACA TN 3737, 1956.

TABLE 1.- RAM B2 VEHICLE COMPONENT WEIGHTS

Weight, lb

First stage:
Lower C section, diaphragm, hardware, and fairings 70.30
Spin shell, launch ring, and hardware 105.50
Spin motor mount, hardware, and batteries 99.50
Harness and attachments 1.56
Base F section, seal, and hardware 268.10
Pyrogen unit loaded 14.29
Pyrogen unit expended 9.29
Castor motor loaded 8,724.28
Castor motor expended 1,272.28
Spin motors loaded 85.30
Spin motors expended 58.10
Loaded assembly 9,368.83
Burnout assembly 1,727.03

Second stage:
Lower G section, diaphragm, and pressure switch and transducer 44.13
Aluminum tape for motor wrap 0.63
Heat shield, splice plates, and hardware 59.00
Upper C section, batteries, command receivers, and hardware 238.26
Antares igniter loaded 3.00
Antares igniter expended 1.00
Antares motor loaded 2,275.40
Antares motor expended 166.40
Static balance weight . . . . None
Loaded assembly 2,620.42
Burnout assembly 509.42

Third stage:
Payload, antenna shields, accelerometers, and bracket 247.49
Heat shield and hardware 28.25
Wire bundles and clips 0.31
Upper C section and hardware 61.71
Alcor igniter loaded 3.50
Alcor igniter expended 1.50
Alcor motor loaded 976.31
Alcor motor expended 97.41
Dynamic balance weight . . . . None
Loaded assembly 1,317.57
Burnout assembly 436.67

Totals:
Loaded first stage 13,306.82
Burnout first stage 5,665.02
Loaded second stage 3,937.99
Burnout second stage 1,826.99
Loaded third stage 1,317.57
Burnout third stage 436.67

TABLE 2.- CALCULATED FLIGHT WEIGHT ANALYSIS FOR RAM B2 VEHICLE

Event	Weight, lb	Distance from station 0 to center of gravity, in.
First-stage ignition	13,306.82	287.56
First-stage propellant consumed prior to spin-up (0.8 sec after ignition)	180.66	
Spin-up	13,126.16	
First-stage propellant consumed during spin-up (0.5 sec after spin-motor ignition)	135.50	
Spin-motor propellant consumed	26.50	
Spin-motor ejection	12,964.16	
Spin motors and rig	158.30	
First-stage thrusting	12,805.86	
Cork ablated during thrusting	0.30	
Noncharring material ablated during thrusting . .	3.32	
Remaining propellant consumed	7,140.84	
First-stage burnout	5,661.40	207.99
Cork ablated during coast	0.10	
Noncharring material ablated during coast	1.14	
First-stage inert	1,727.03	
Second-stage ignition	3,933.13	131.86
Cork ablated during thrusting	0.60	
Noncharring material ablated during thrusting . .	0.65	
Propellant consumed	2,111.00	
Second-stage burnout	1,820.88	97.64
Second-stage inert	509.42	
Third-stage ignition	1,311.46	64.44
Cork ablated during thrusting	0.90	
Noncharring material ablated during thrusting . .	0.30	
Propellant consumed	880.90	
Experiment consumed prior to burnout	6.75	
Third-stage burnout	422.61	51.10

TABLE 3.- VEHICLE INSTRUMENTATION
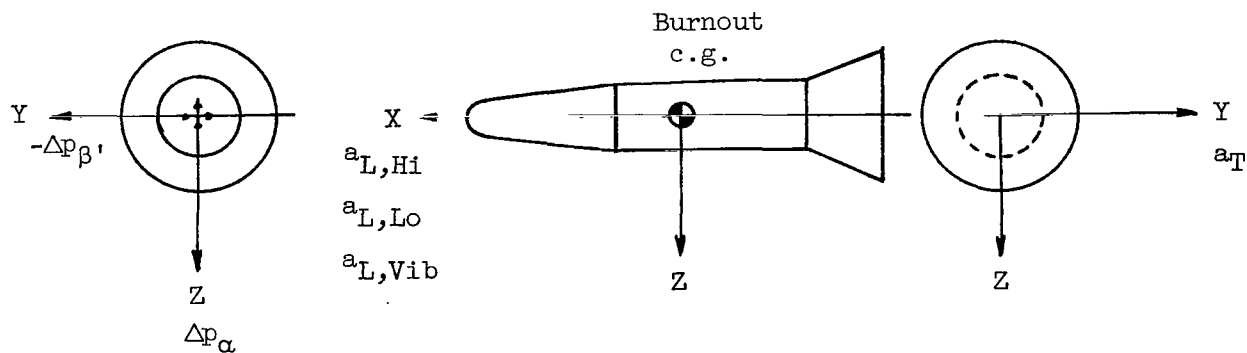
Instrument	Full-scale range	Location		
		x, in. (a)	y, in. (a)	z, in. (a)
Longitudinal accelerometer, $a_{L,Hi}$	-3g to 25g	9.95	0	-2.12
Longitudinal accelerometer, $a_{L,Lo}$	±2g	9.95	2.12	0
Transverse accelerometer, a_T	±3g	8.85	0	2.12
Longitudinal vibrometer, $a_{L,Vib}$	±30g	2.41	4.49	-8.82
Sun detector		49.06	-0.76	5.74
Normal differential pressure, Δp_α	±1 psid	67.20	0	±2.83
Transverse differential pressure, $\Delta p_{\beta'}$ . .	±1 psid	67.20	±2.83	0
Motor chamber pressure p_c:				
Second stage	0 to 500 psia			
Third stage	0 to 625 psia			

[a]Distance along body axis from payload stage burnout center of gravity.

25

TABLE 4.- LOCATION OF THERMOCOUPLES
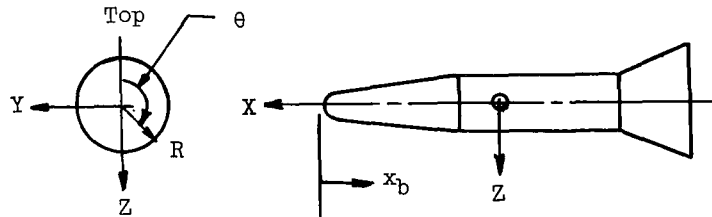
Commutated switch position	θ, deg	x_b, in.	R, in.	Material thickness, in.	Sensor location
1	0	5.75	4.077	0.255 beryllium	Payload beryllium section
2	270	10.25	4.837	0.199 beryllium	Payload beryllium section
3	0	11.25	5.001	0.193 beryllium	Payload beryllium section
4	270	13.50	5.371	0.182 beryllium	Payload beryllium section
5	270	16.75	5.905	0.162 beryllium	Payload beryllium section
6	90	21.86	6.500	0.040 aluminum + 0.33 non-charring ablation material	Payload conical section
7	210	27.86	7.460	0.040 aluminum + 0.32 non-charring ablation material	Payload conical section
8	330	33.86	8.430	0.040 aluminum + 0.31 non-charring ablation material	Payload conical section
9	93	39.86	9.390	0.040 aluminum + 0.30 non-charring ablation material	Payload conical section
10	210	45.86	10.350	0.040 aluminum + 0.29 non-charring ablation material	Payload conical section
11	338	51.86	10.820	0.051 aluminum + 0.25 non-charring ablation material	Payload cylindrical section
12	102	59.86	10.746	0.125 fiber glass + 0.25 non-charring ablation material	Payload cylindrical section
15	0	236.35	20.910	Free air	2d stage fin, trailing edge
16	0	236.35	31.500	0.125 high-temperature superalloy	2d stage fin, leading edge
17	12	224.12	10.870	Free air	2d stage nozzle
18	0	143.17	11.200	Free air	2d stage forward dome
19	315	130.07	9.940	Free air	3d stage nozzle
22	45	136.13	16.760	0.05 aluminum + 0.20 cork	Flare face
23	225	137.04	14.000	0.06 inconel	Flare closure
24	225	131.13	15.760	Under 0.10 cork	Flare face
25	315	131.13	15.950	Constantan foil	Flare face

TABLE 5.- SEQUENCE OF TRAJECTORY EVENTS FOR RAM B2 FLIGHT

[Launch date: May 28, 1963; launch time: 18:59:09 G.M.T.]

Event	Time from first-stage ignition, sec
First-stage ignition	0.00
First movement	.10
Spin-motor ignition	.82
Spin-motor separation	1.35
First-stage burnout	38.43
Second-stage ignition	50.95
Second-stage burnout (50 psia)	89.08
Third-stage ignition	89.08
Third-stage separation	89.10
Third-stage burnout	118.53
Apogee	239.00 (approx.)
Impact	571.00 (approx.)
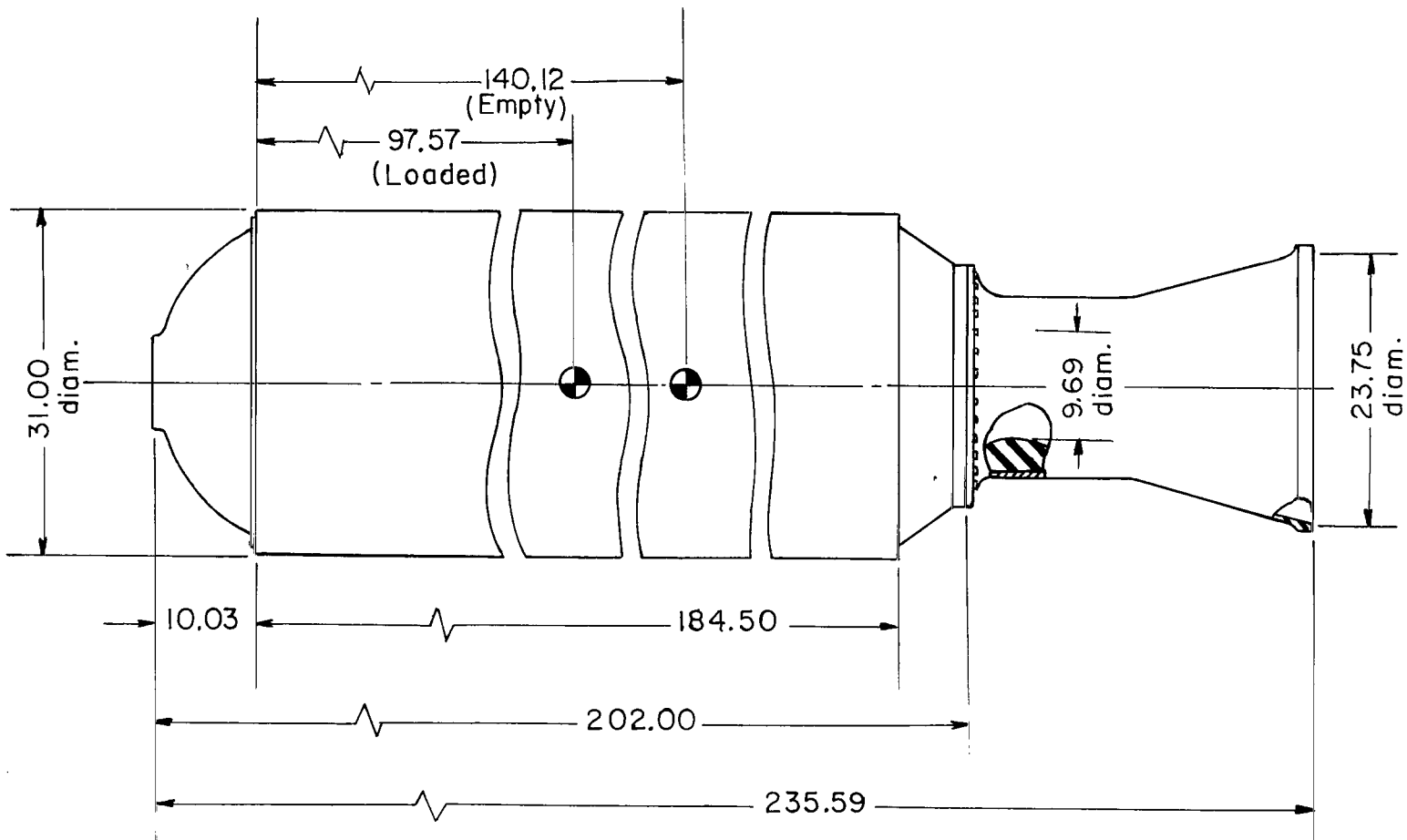
Figure 1.- First-stage rocket motor (Castor). All dimensions are in inches.
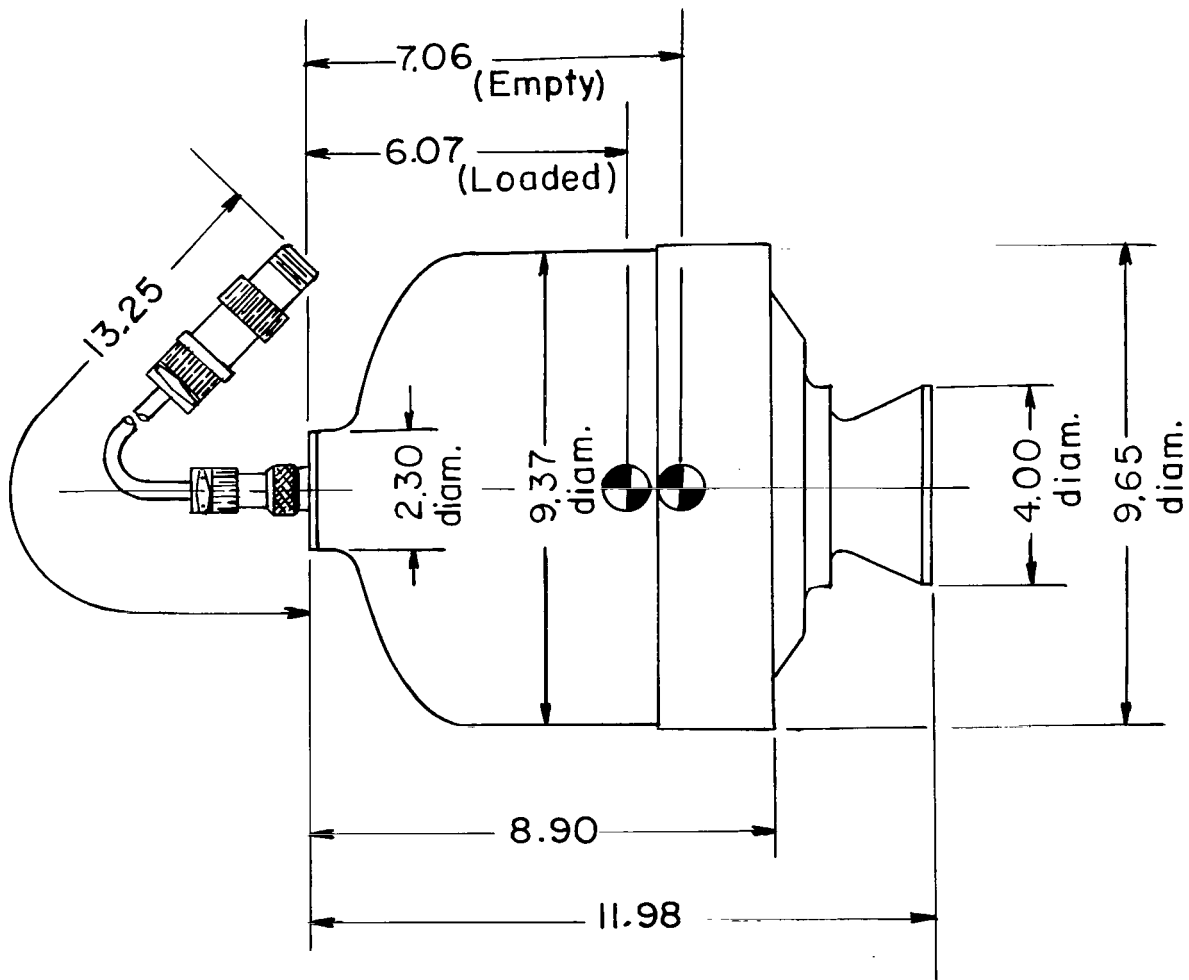
Figure 2.- First-stage spin motor (Hotseat). All dimensions are in inches.
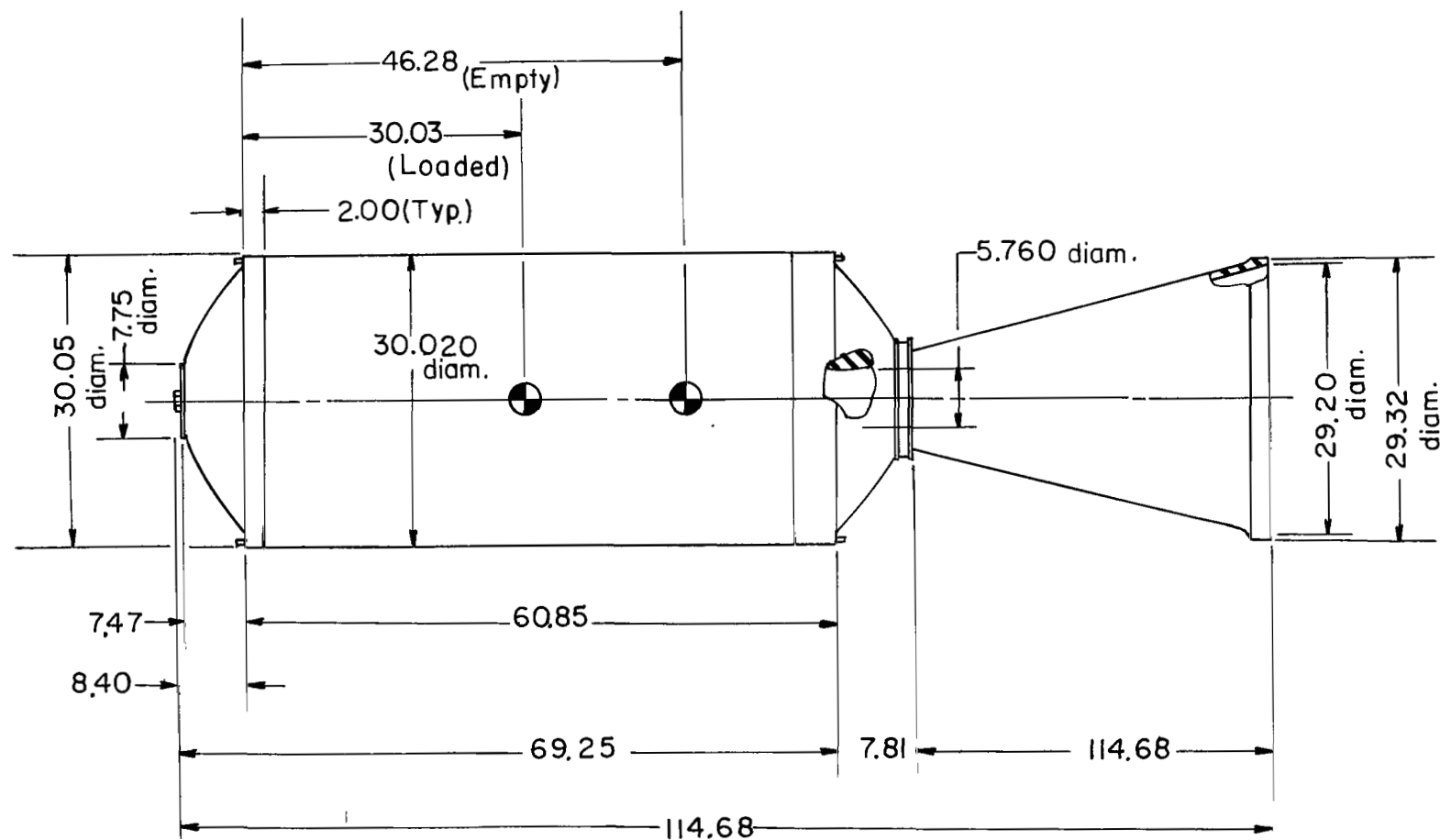
Figure 3.- Second-stage rocket motor (Antares). All dimensions are in inches.
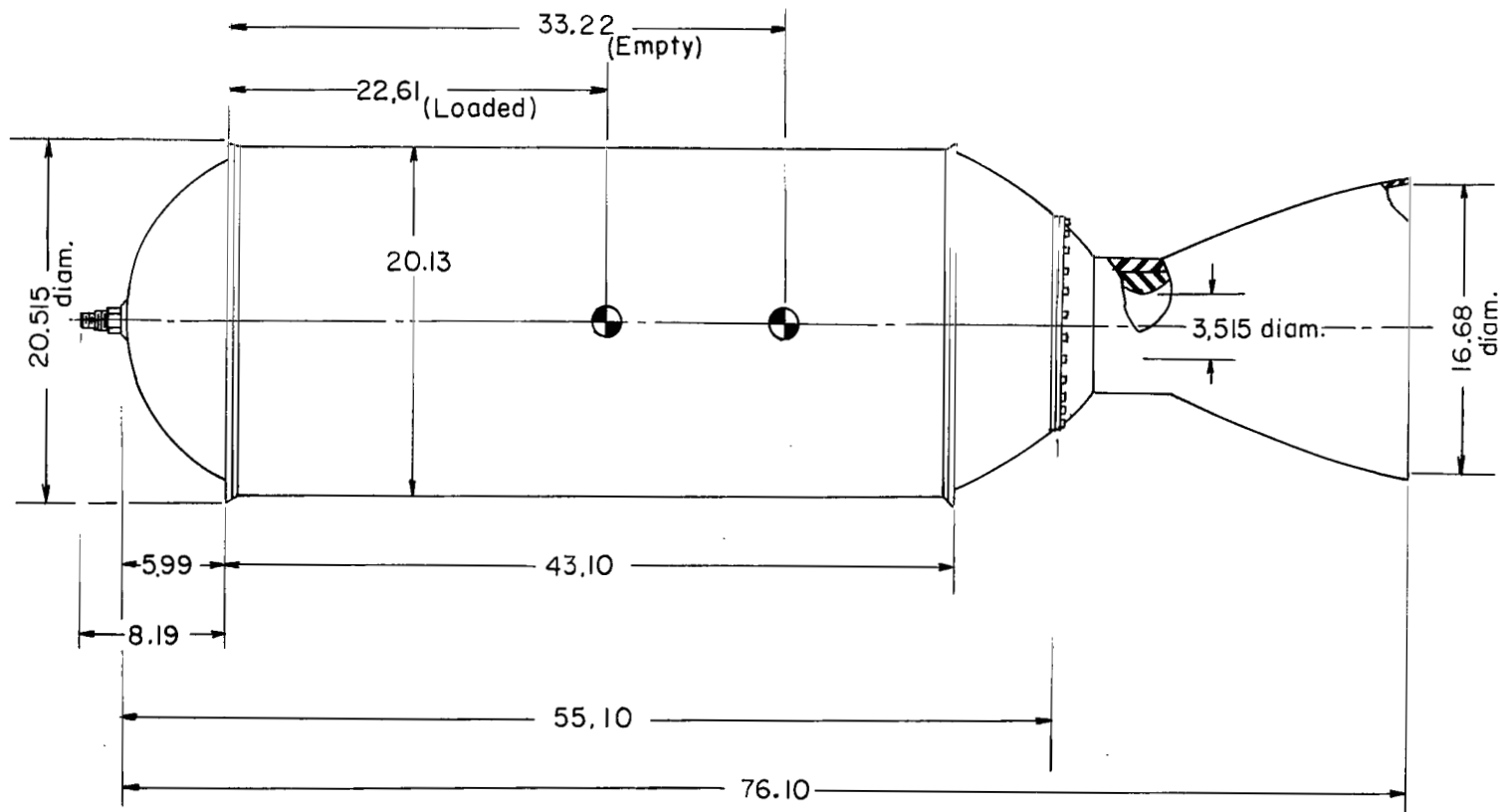
Figure 4.- Third-stage rocket motor (Alcor). All dimensions are in inches.

Figure 5.- RAM B inboard profile. Dimensions are in inches unless otherwise stated.
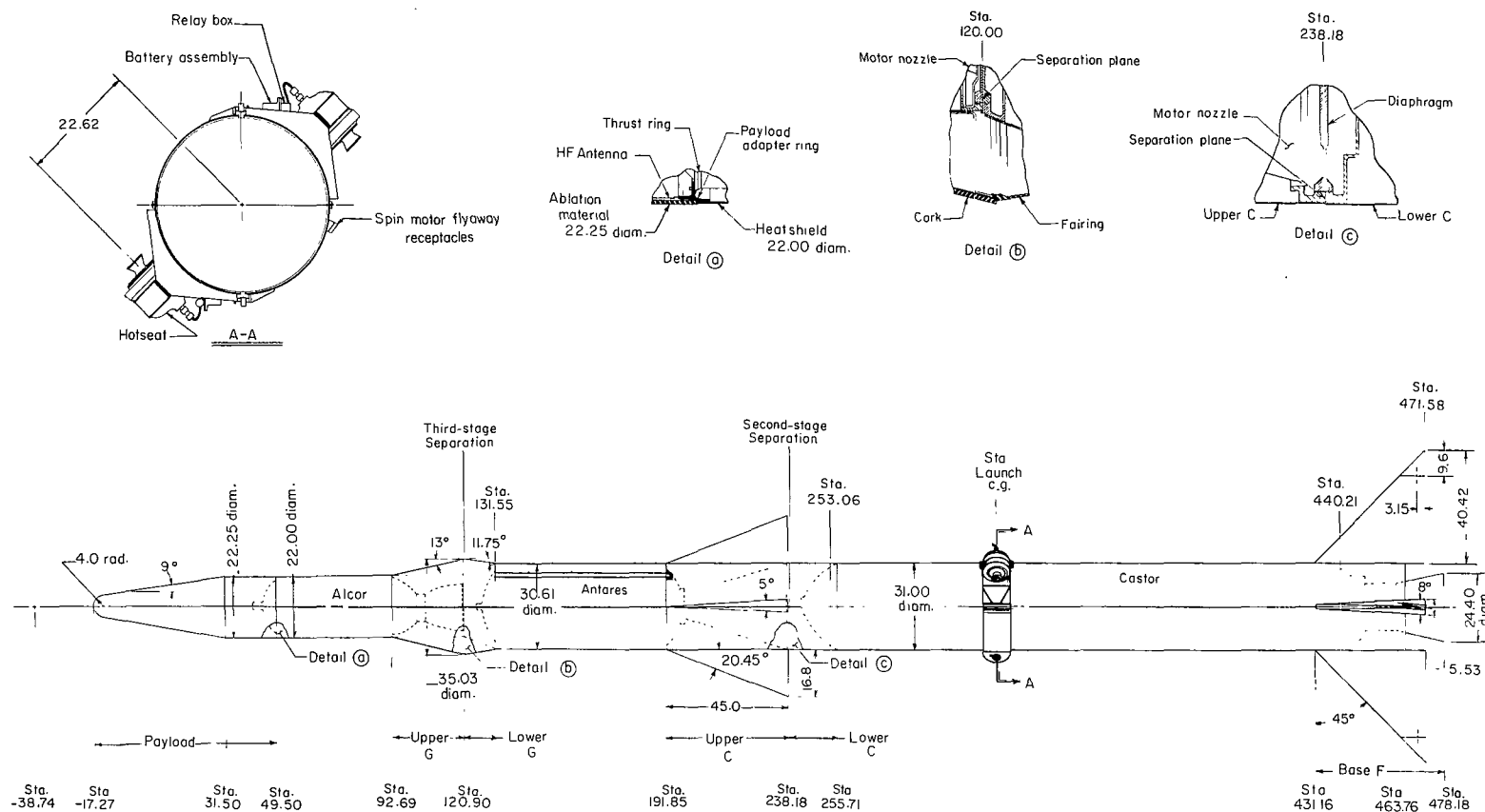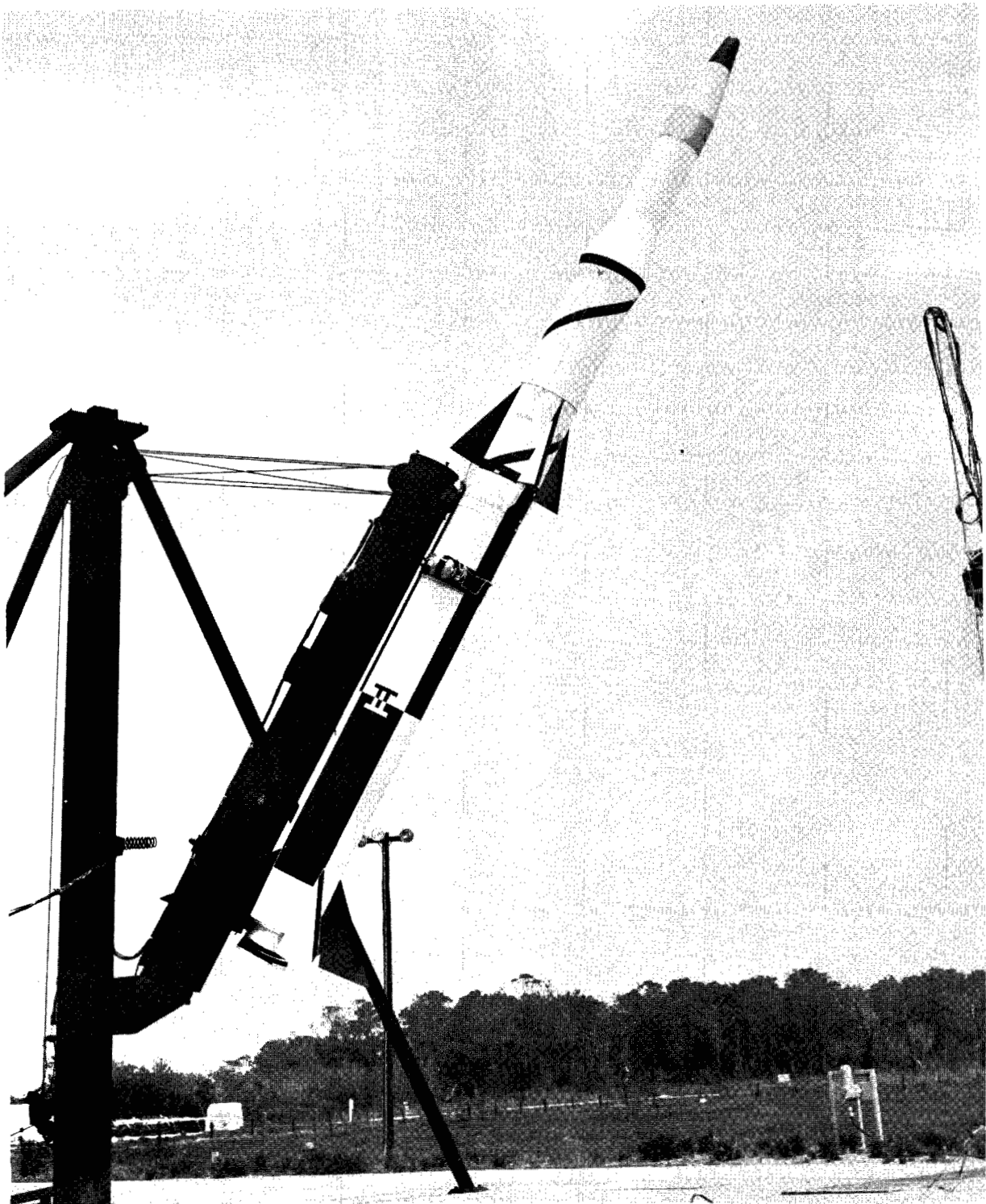
Figure 6.- RAM B vehicle and payload on launcher.   L-63-4919
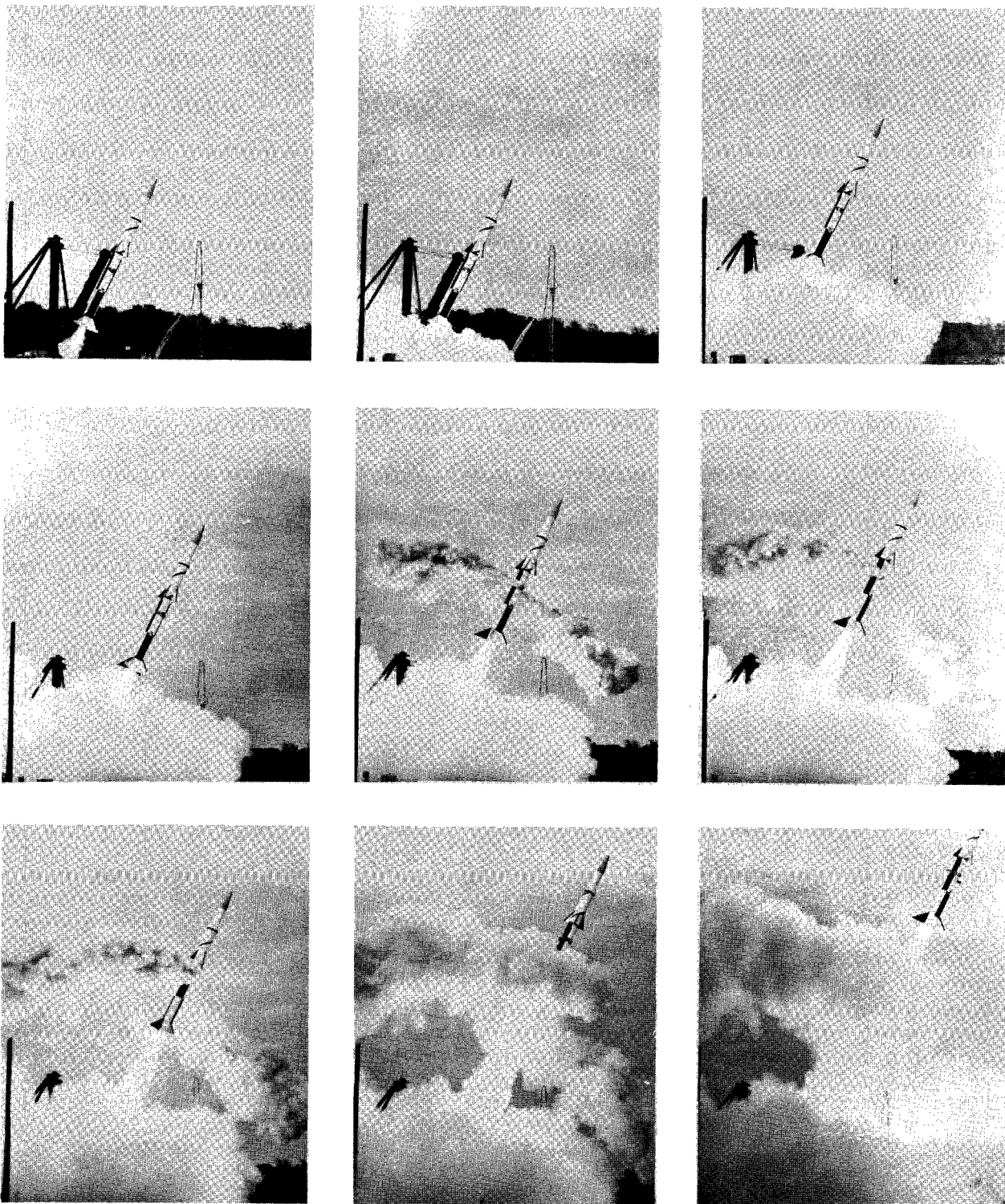
Figure 7.- RAM B spin-up sequence.

L-63-6553

34

Aft launcher fitting

Spin motor
lanyard switch

Nozzle flame seal

Vent hole

Deflected fin tip
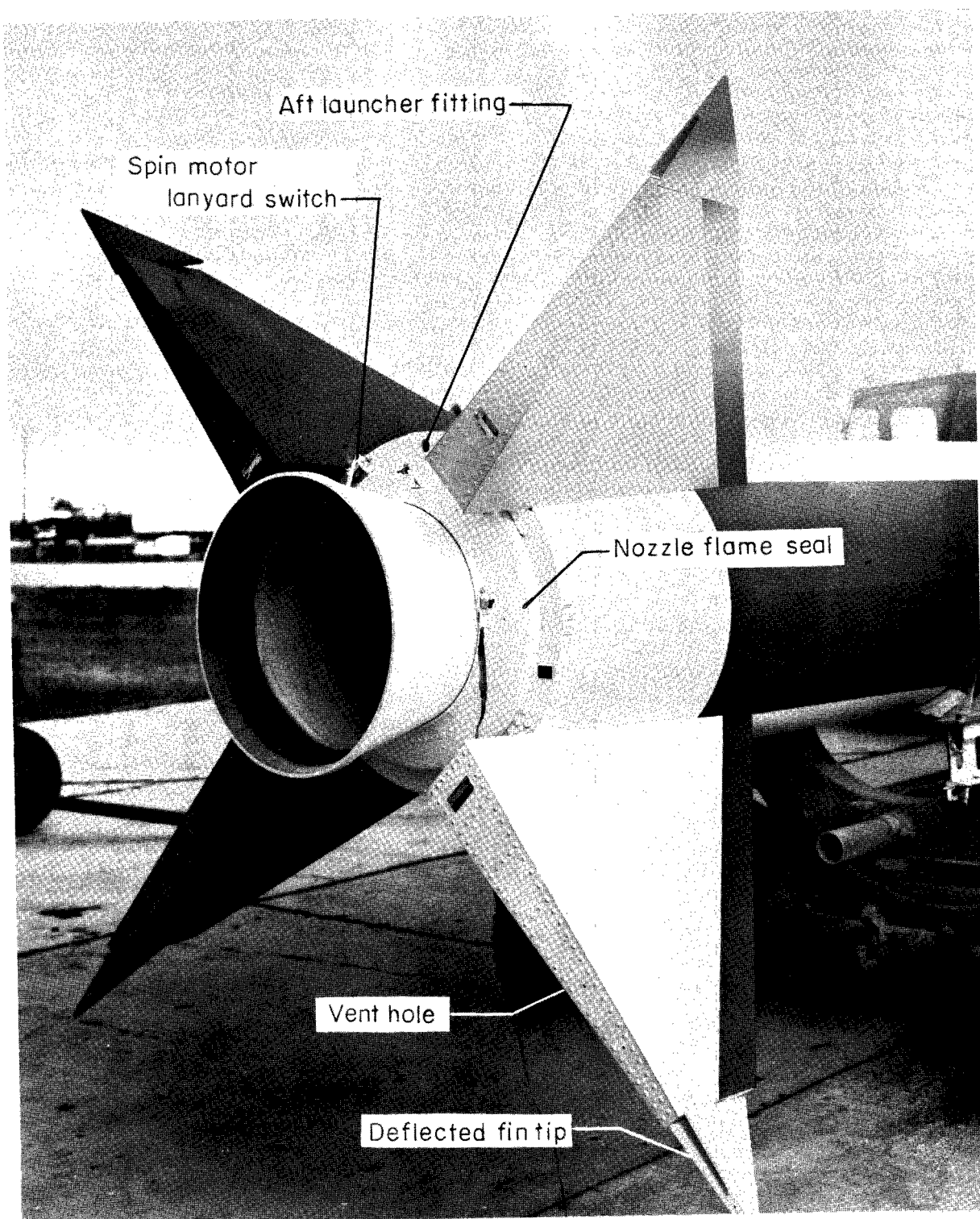
Figure 8.- Base F section.

L-63-8831.1

35

.003 Glass filler

Steel L.E.
0.25 radius

Glass skin

Aluminum fin core

Section A-A

Cast iron
fin tip

0.25 diam.pins
4130 steel

0.75 diam.shaft
4130 steel

A

A

Aluminum skin
0.10 thick

Silicone rubber
sealant

Aft launcher fitting
(rotated)

Nozzle seal

Castor-E 8
motor

9°

Motion
switch

Nozzle

Leading edge
0.071 thick
4130 steel

Glass fabric tape

Fiber-glass skin
0.10 thick

Aluminum-alloy
core structure

Figure 9.- Base F transition section structural detail. Dimensions are in inches unless otherwise noted.
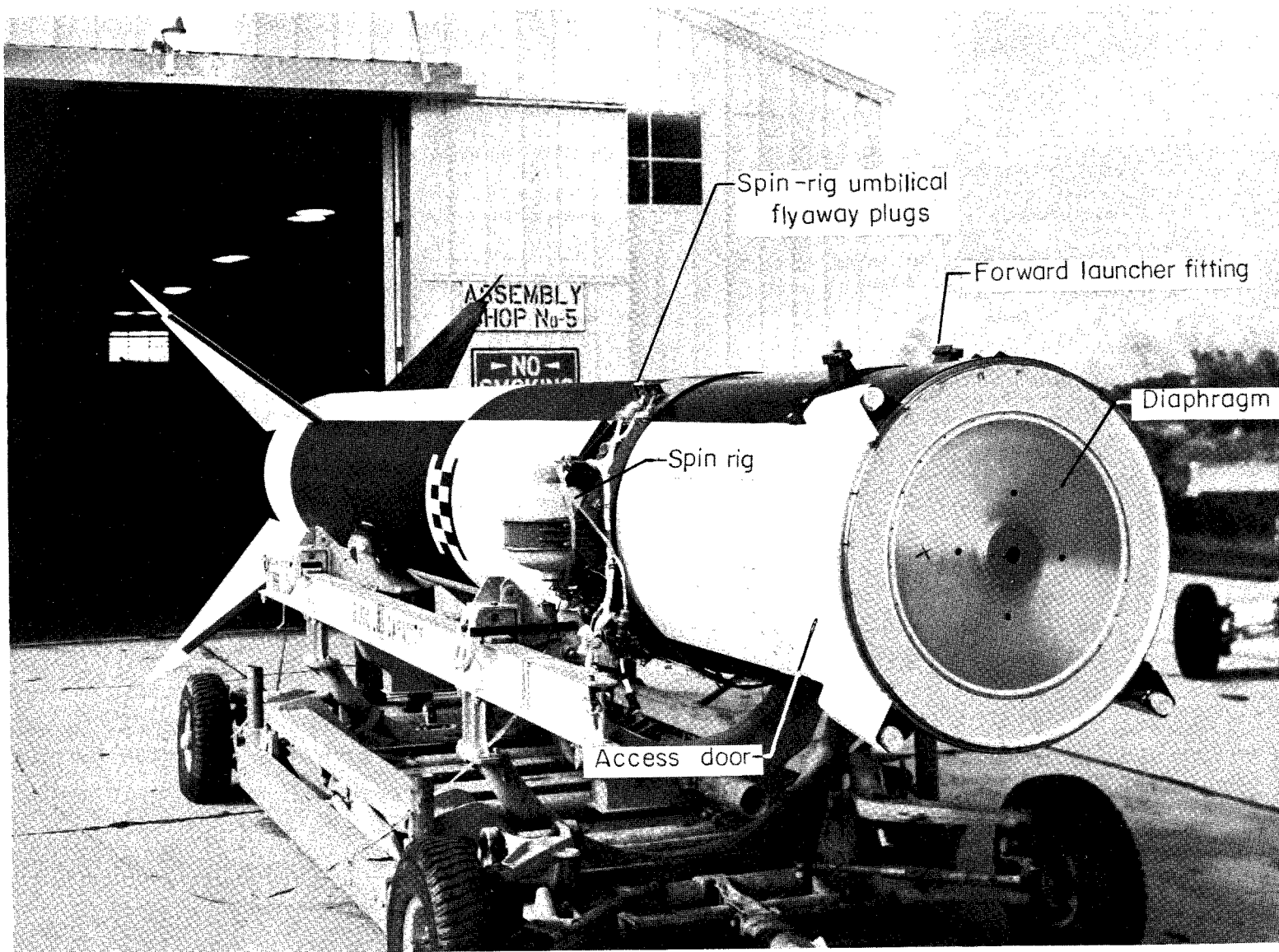
Figure 10.- First-stage assembly.

L-63-8829.1

Ignition
system battery

Cast aluminum
substructure

Lower C sect.
.13 fiber-glass skin

Ext. plug cover
(Typ. 4 fins)

J Box

Thermocouple

Launcher
lugs

Fiber-glass heat
shield .05 thick

Nozzle
seal

Upper C sect.
.12 fiber-glass
skin

Elec. plug
heat
cover

Spin rig torque
sleeve

Cork thermal
insulation
.25 thick

Blowout
diaphragm

Launcher
ring

Antares
motor

Castor
motor

Nozzle

2d Stage fire relay

Command receiver battery

Fairing

Umbilical well
3 plugs (typ.)
(Rotated for clarity)

Spring actuated cover

Leading edge
.125 steel
.15 radius

Fiber-glass skin
.12 thick

First motion switch
2 switches (typ.)
Rotated for clarity

Figure 11.- Details of C section. All dimensions are in inches.
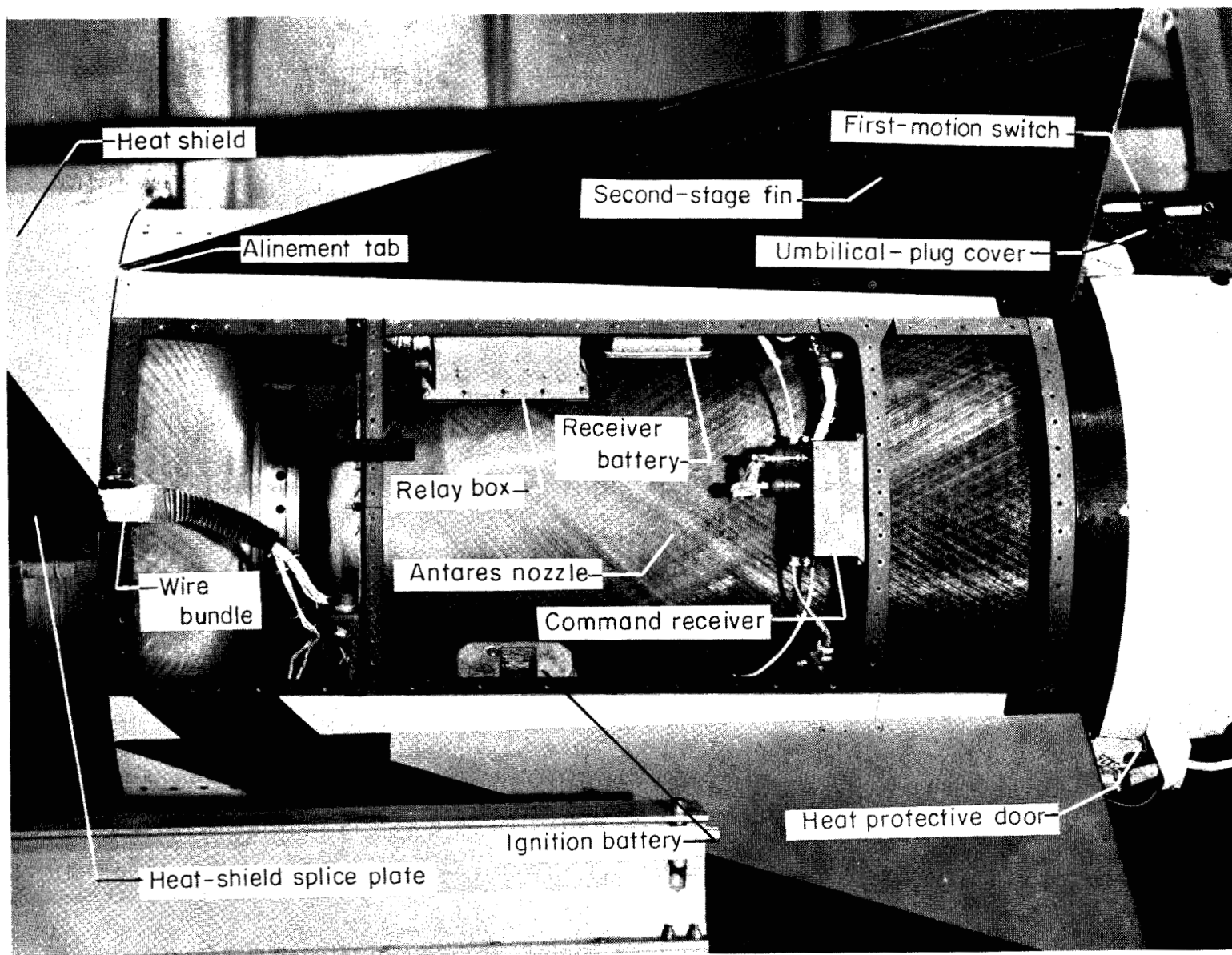
Figure 12.- Upper C section.

L-64-1729.1
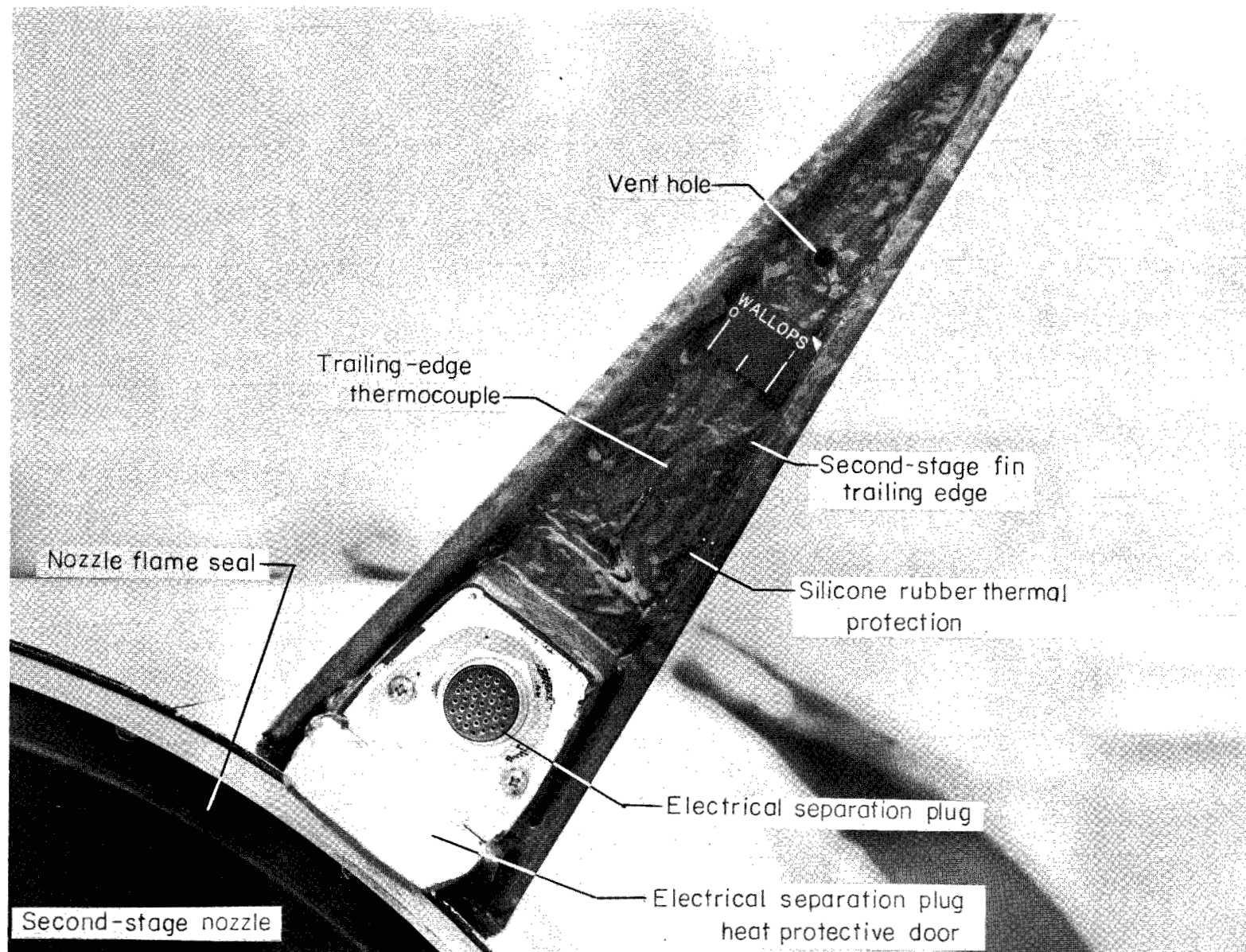
Figure 13.- Second-stage-fin trailing-edge details.
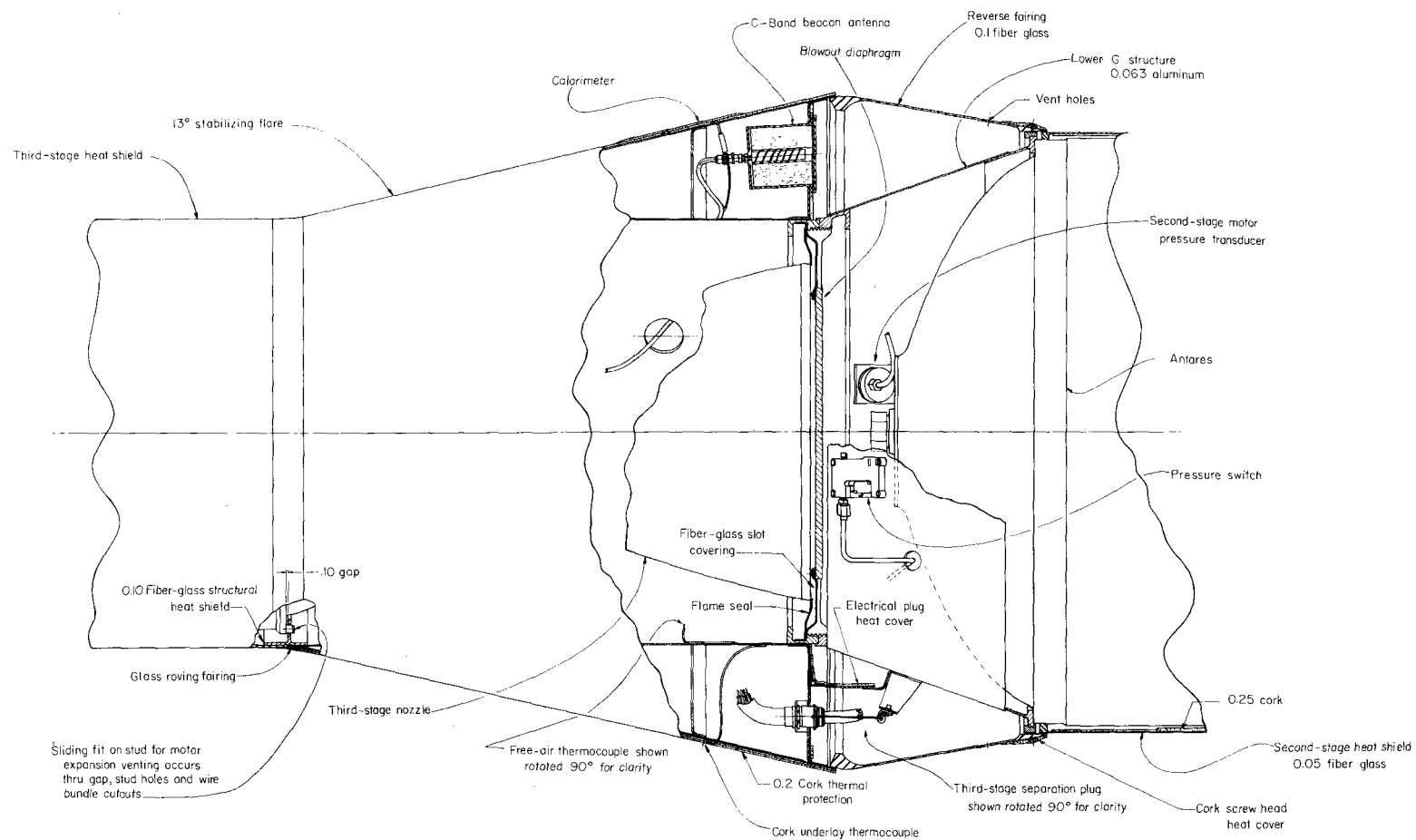
Figure 14.- Details of G section.
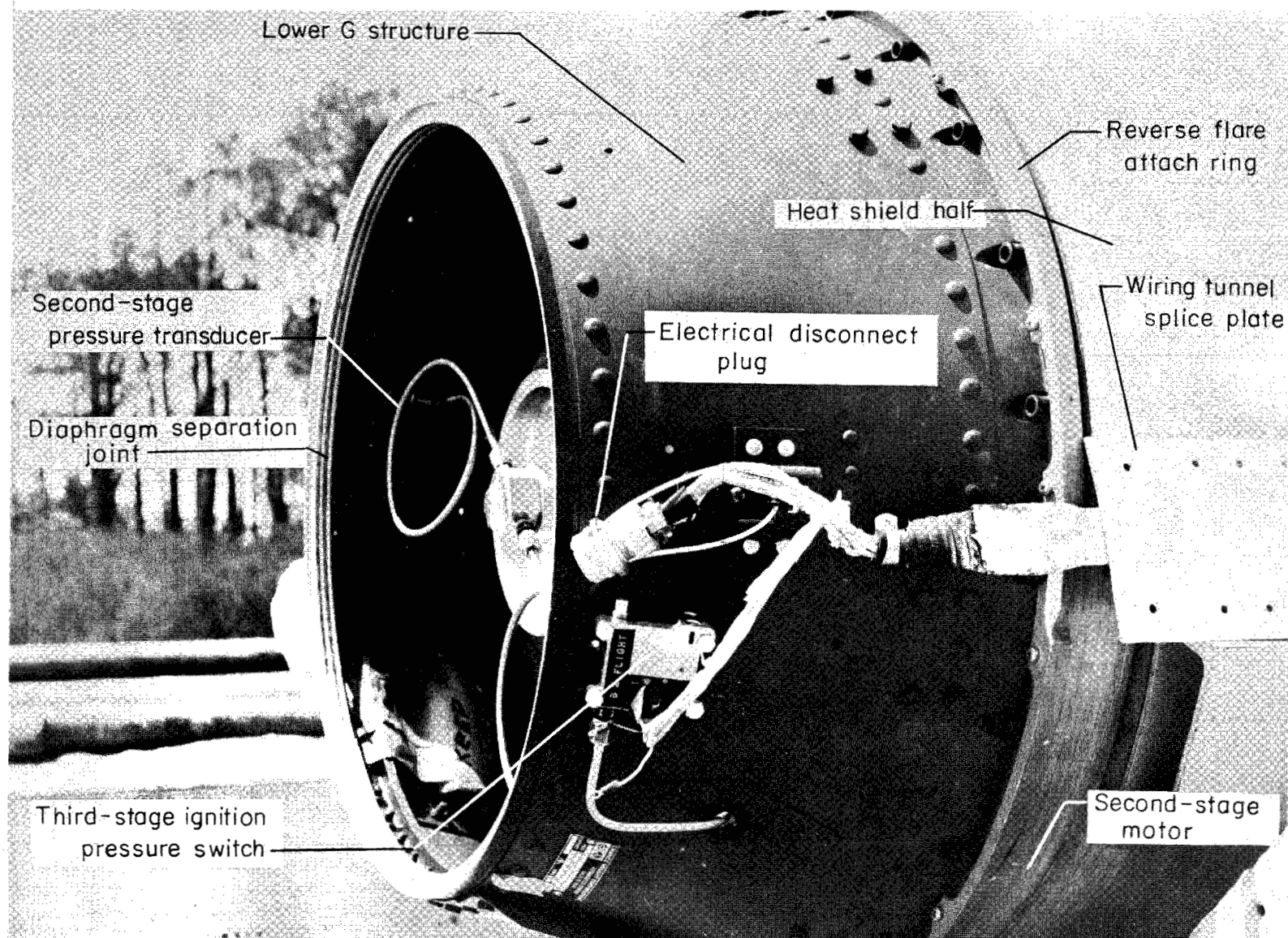
Figure 15.- Lower G section structure.   L-63-4937.1

Separation diaphragm

Second-stage pressure transducer

Vent hole

Vehicle alinement mark

Second-stage forward dome free-air thermocouple

Lower G aerodynamic fairing

Lower G structure

Access door

Figure 16.- Lower G section assembly.

L-63-3952.1

43

Cork heat protective covering

Access door

Electrical plug disconnect lanyard

Electrical plug heat protective cover

Second-stage wire bundle

Reverse flare break wire
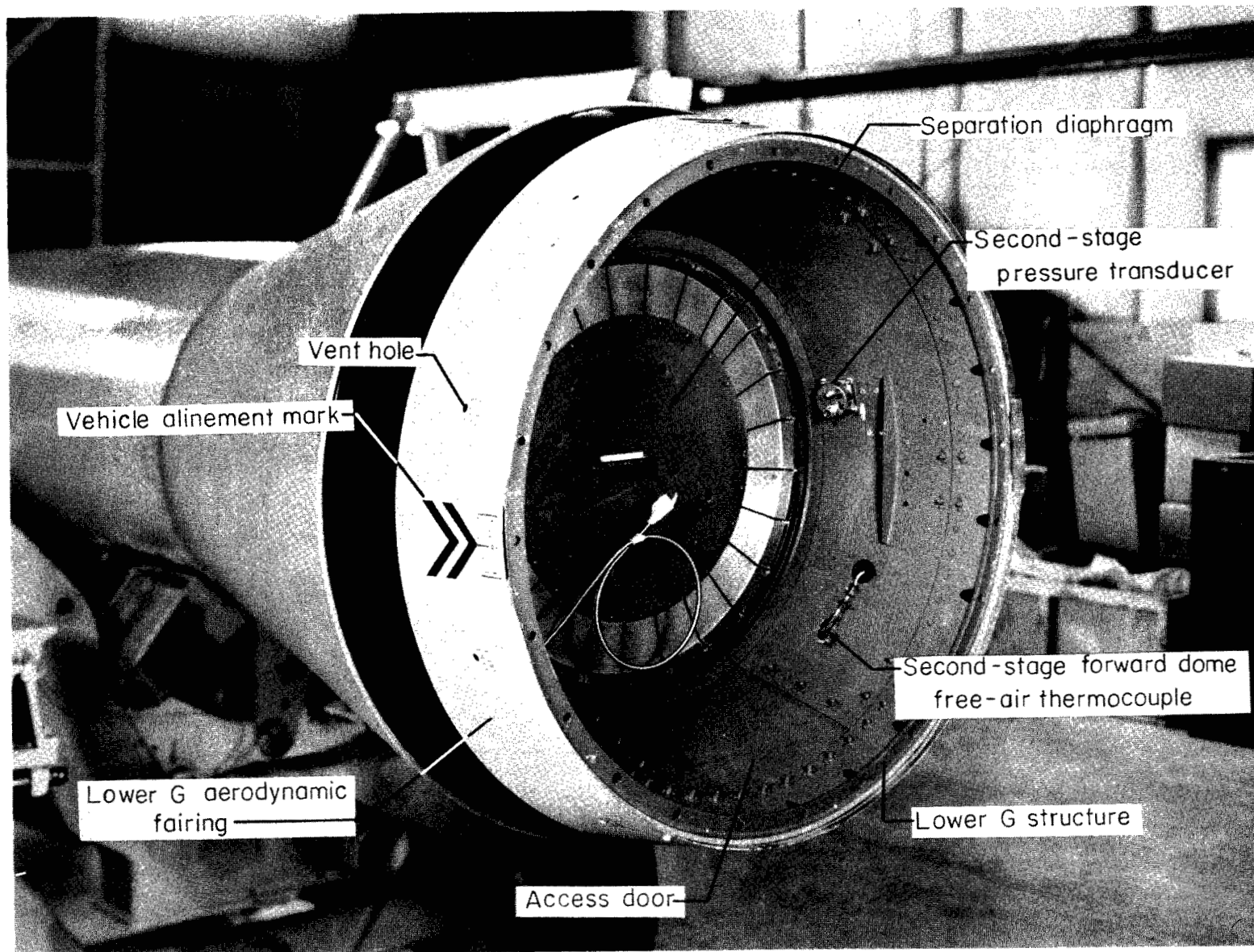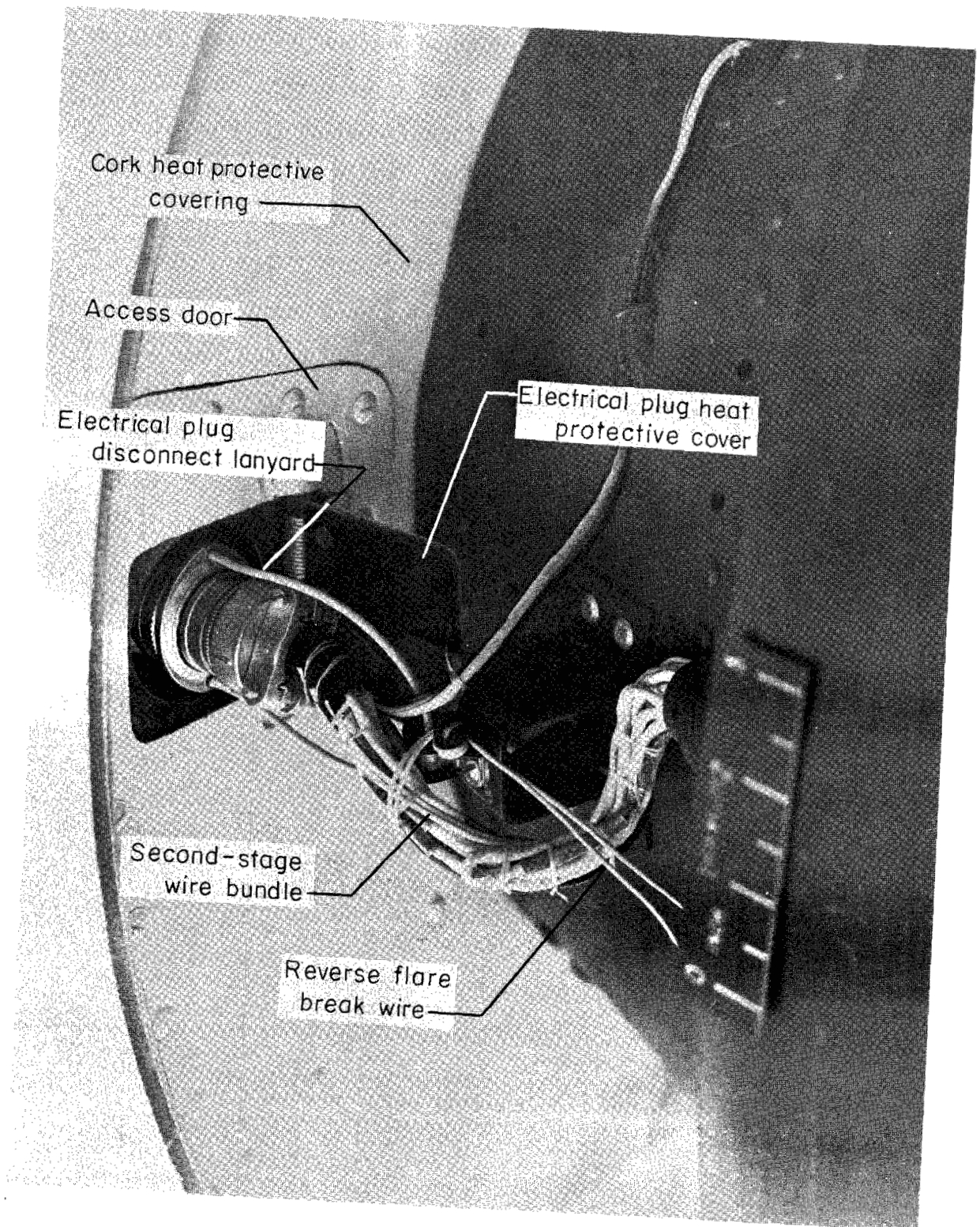
Figure 17.- Lower G section electrical separation plug.

L-63-5248.1

Figure 18.- Third-stage rocket motor and stabilizing flare.   L-62-6248.1
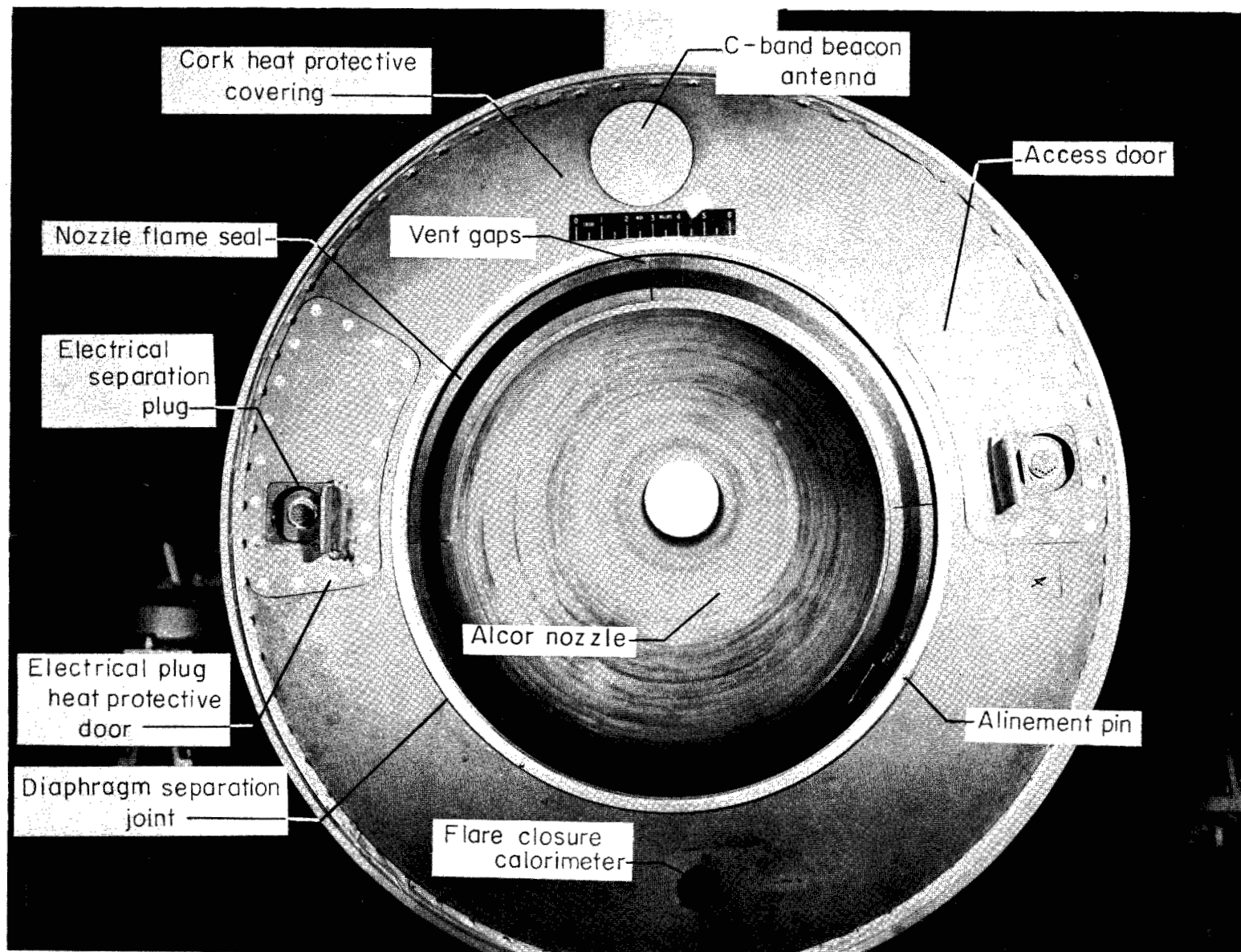
Figure 19.- Upper G section flare closure.

L-63-3516.1
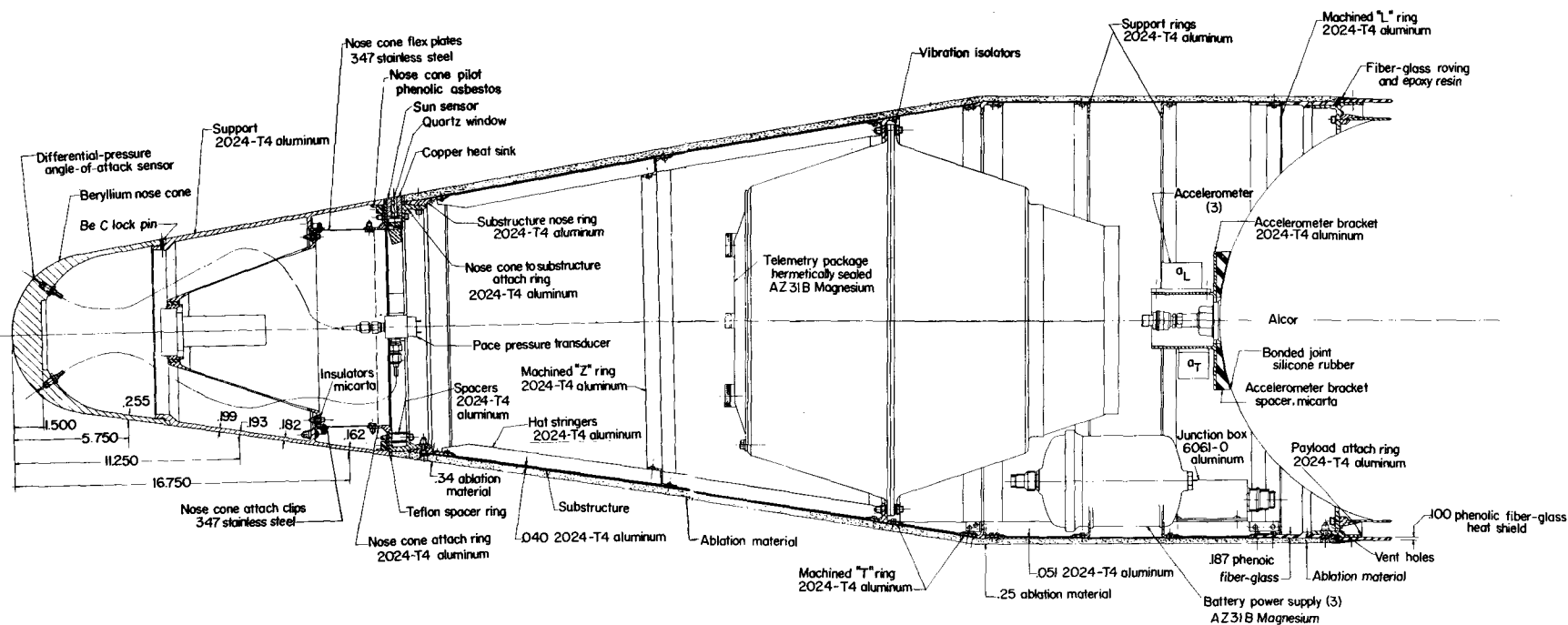
Figure 20.- General payload structure. All dimensions are in inches.

Differential-pressure angle-of-attack sensor

Beryllium nose cone

Be C lock pin

Support 2024-T4 aluminum

Nose cone flex plates 347 stainless steel

Nose cone pilot phenolic asbestos

Sun sensor

Quartz window

Copper heat sink

Substructure nose ring 2024-T4 aluminum

Nose cone to substructure attach ring 2024-T4 aluminum

Pace pressure transducer

Insulators, micarta

Machined "Z" ring 2024-T4 aluminum

Spacers 2024-T4 aluminum

Hat stringers 2024-T4 aluminum

.255

.199 .193 .182

.162

1.500

5.750

11.250

16.750

.34 ablation material

Nose cone attach clips 347 stainless steel

Teflon spacer ring

Nose cone attach ring 2024-T4 aluminum

.040 2024-T4 aluminum

Substructure

Ablation material

Machined "T" ring 2024-T4 aluminum

.25 ablation material

.051 2024-T4 aluminum

Telemetry package hermetically sealed AZ31B Magnesium

Vibration isolators

Support rings 2024-T4 aluminum

Machined "L" ring 2024-T4 aluminum

Fiber-glass roving and epoxy resin

Accelerometer (3)

Accelerometer bracket 2024-T4 aluminum

a_L

a_T

Alcor

Bonded joint silicone rubber

Accelerometer bracket spacer, micarta

Junction box 6061-0 aluminum

Payload attach ring 2024-T4 aluminum

.100 phenolic fiber-glass heat shield

Vent holes

.187 phenoic fiber-glass

Ablation material

Battery power supply (3) AZ31B Magnesium

47

Beryllium nose

Payload

Payload umbilical door

Heat shield

Aerodynamic stabilizing flare

Figure 21.- Third-stage assembly.

L-62-7667.1

Payload attach ring

Glass roving fairing

Transverse accelerometer

Motor pressure transducer

Antenna shield

Longitudinal accelerometer

Third-stage heat shield
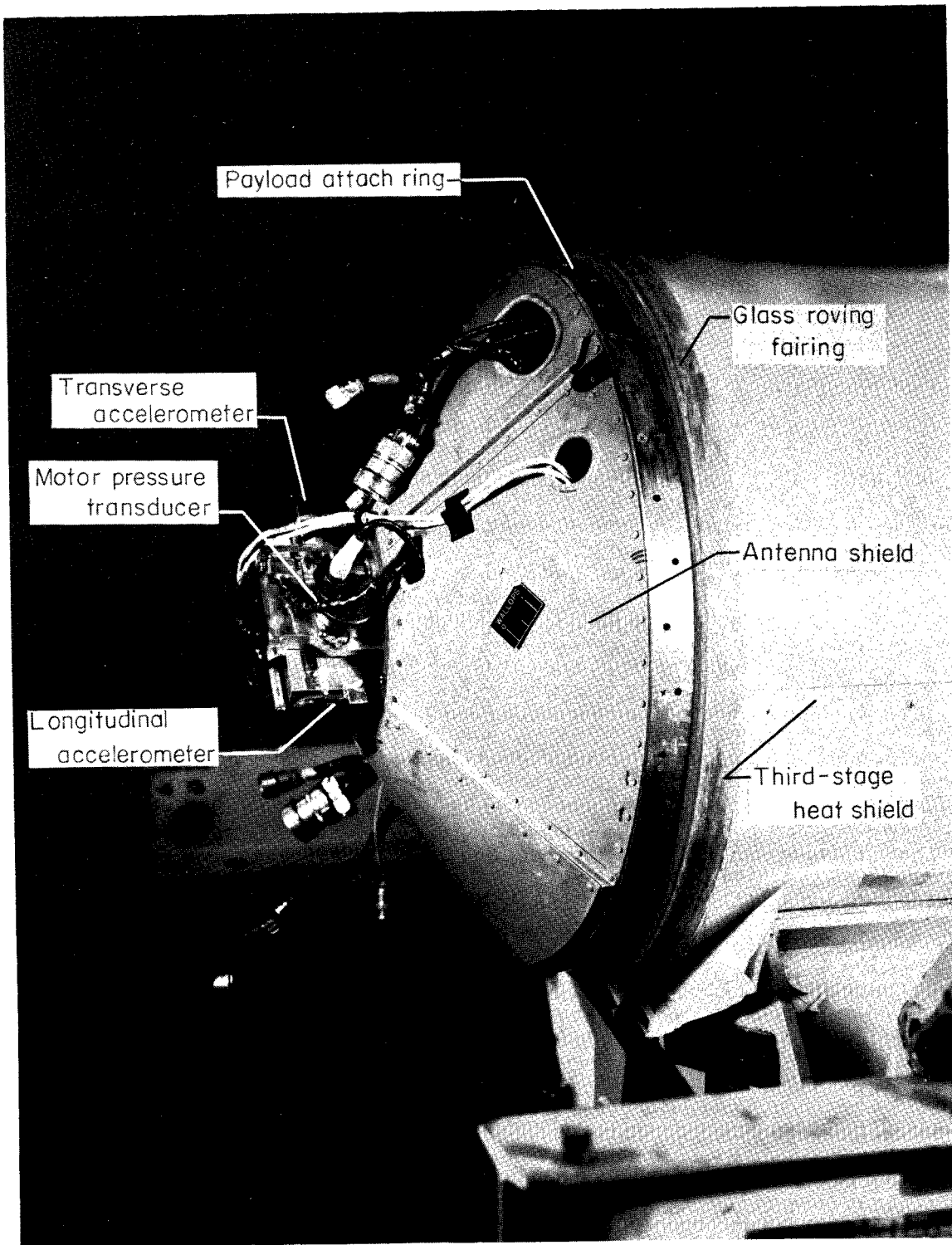
Figure 22.- Payload mounting interface.

L-63-4334.1

49
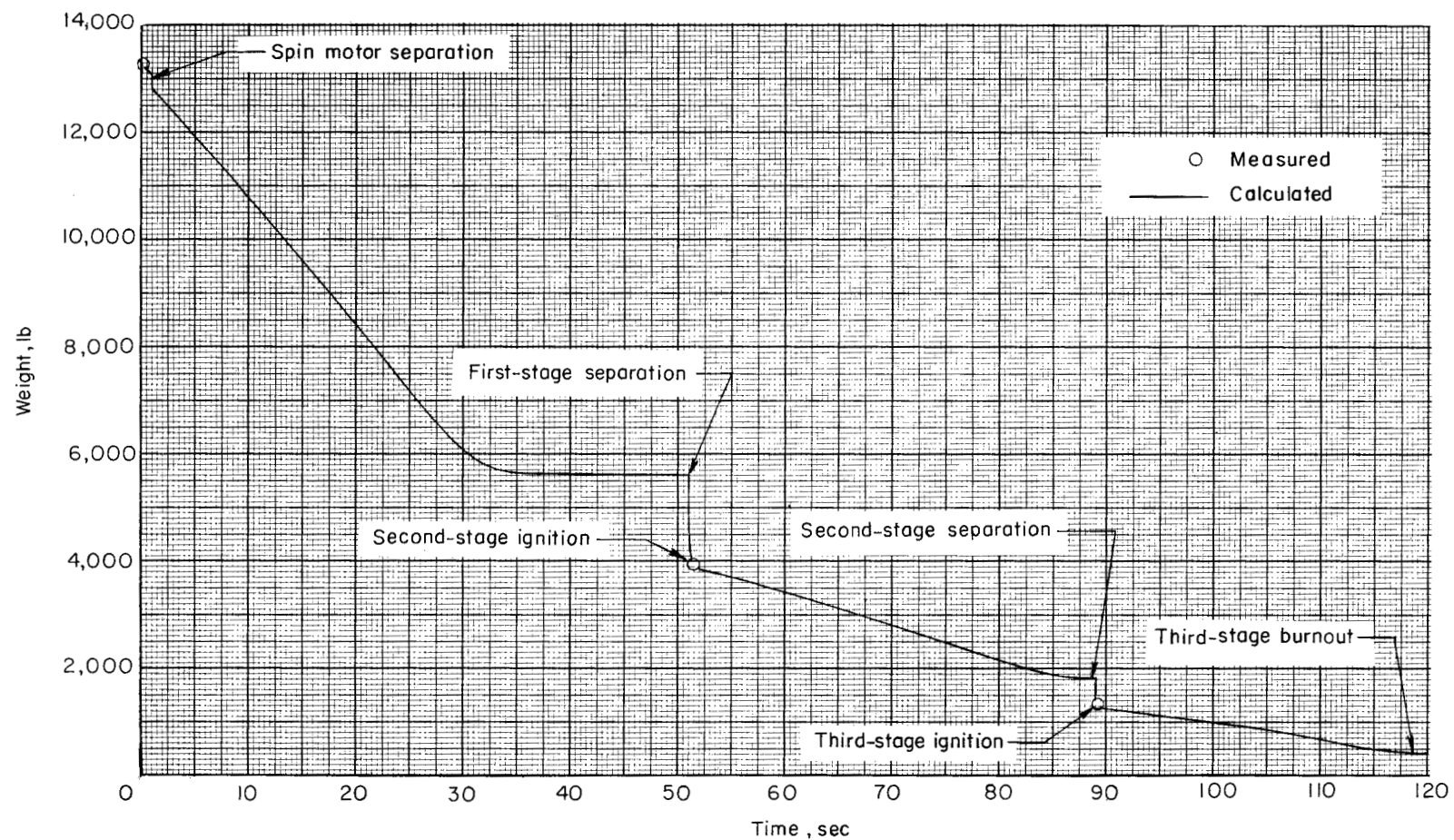
Figure 23.- Time variation of vehicle weight.
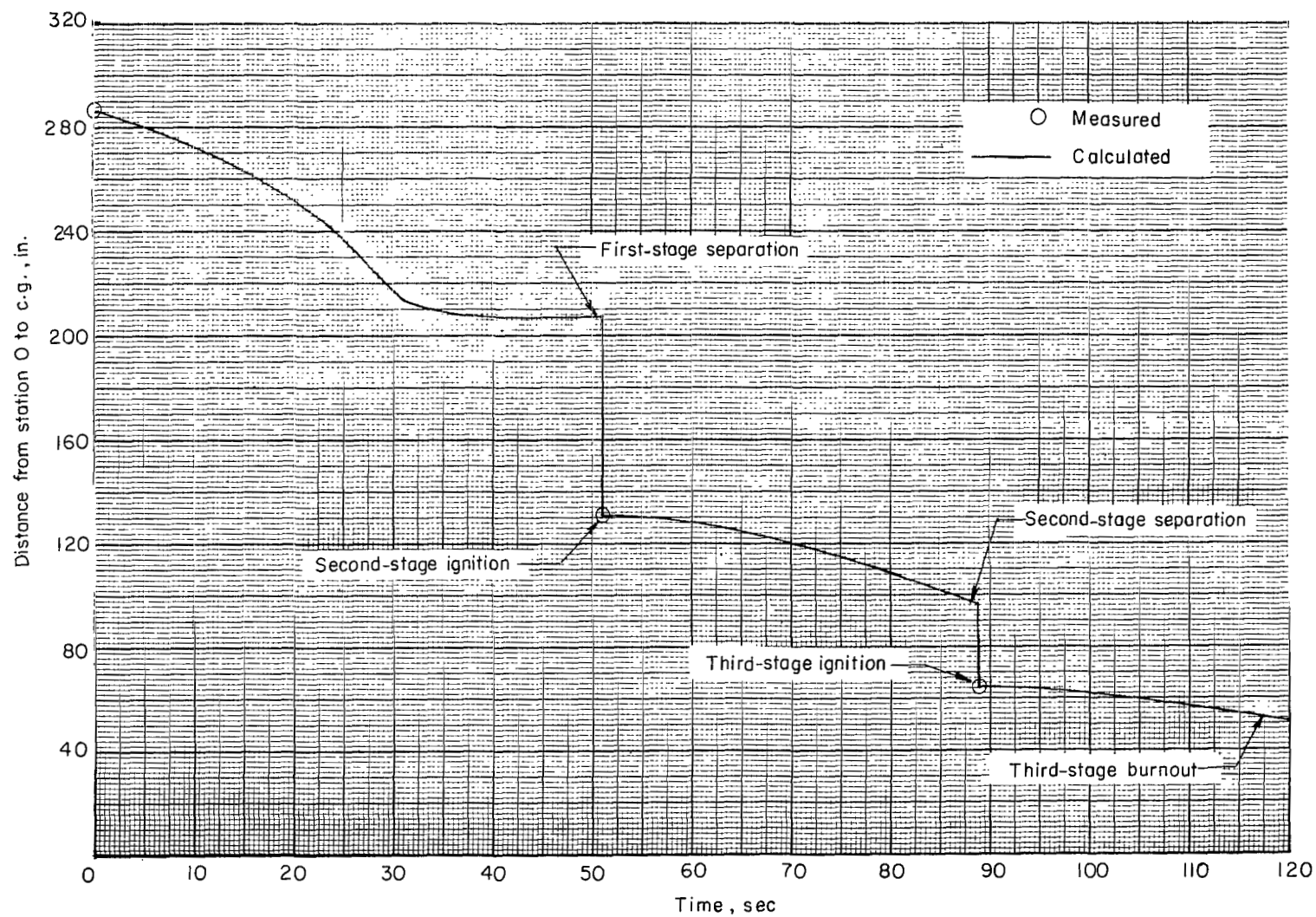
Figure 24.- Time variation of vehicle center-of-gravity location.
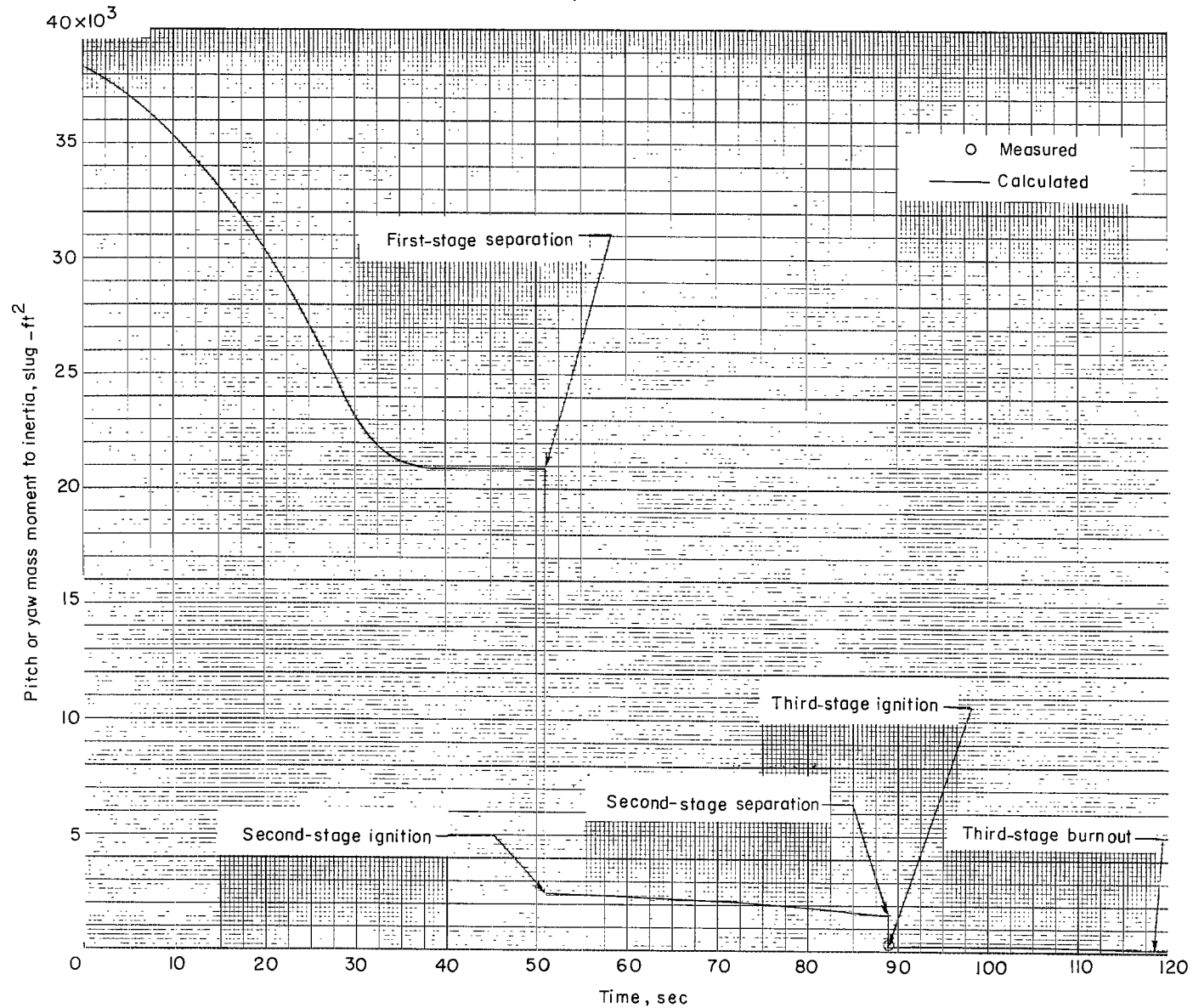
Figure 25.- Time variation of pitch and yaw mass moments of inertia.
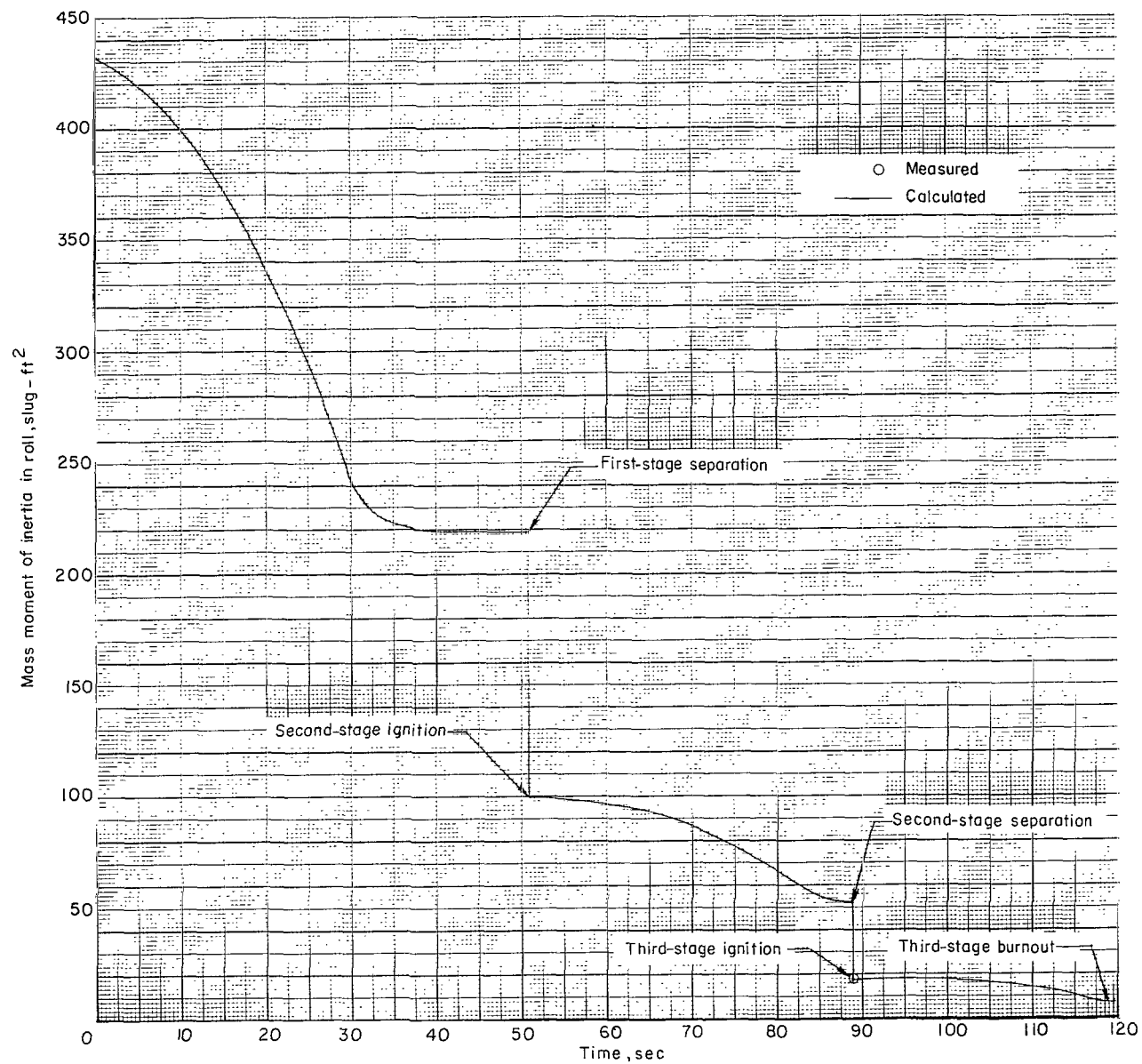
Figure 26.- Time variation of vehicle roll moment of inertia.
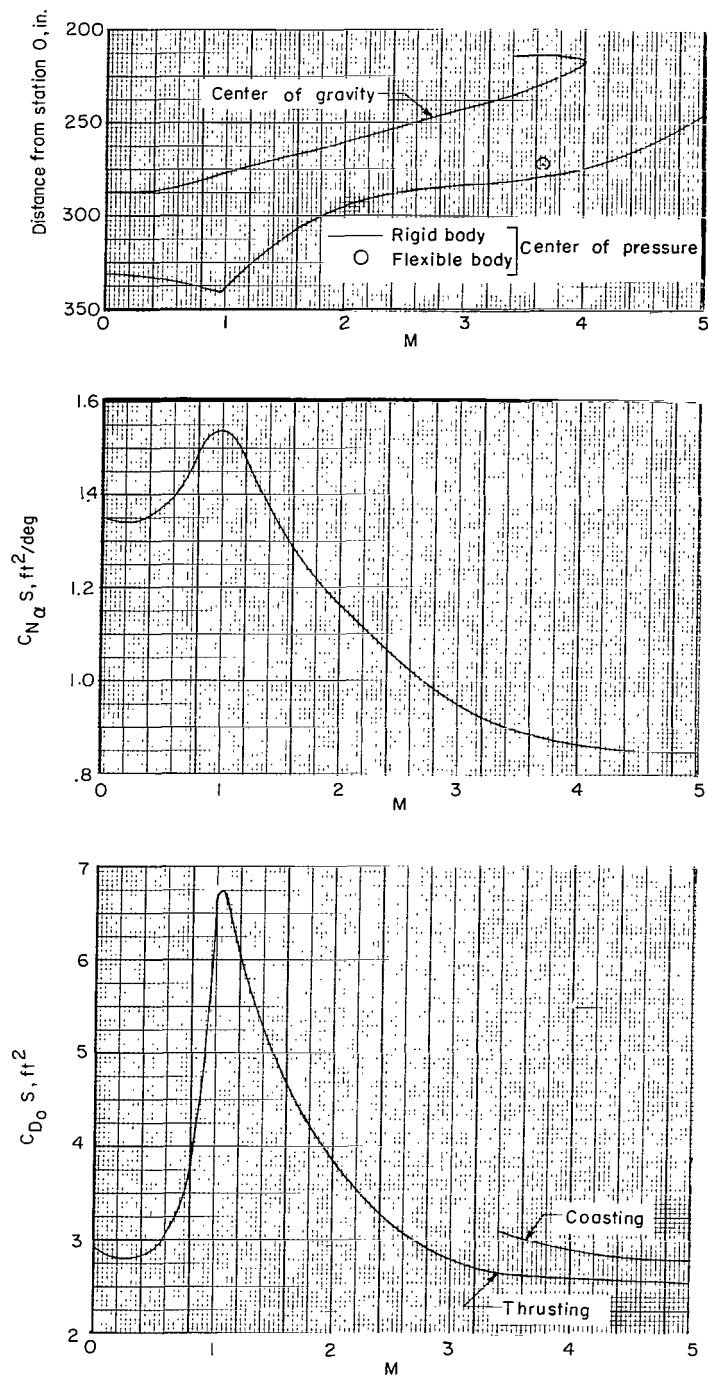
(a) First stage.

Figure 27.- Vehicle longitudinal aerodynamic characteristics.
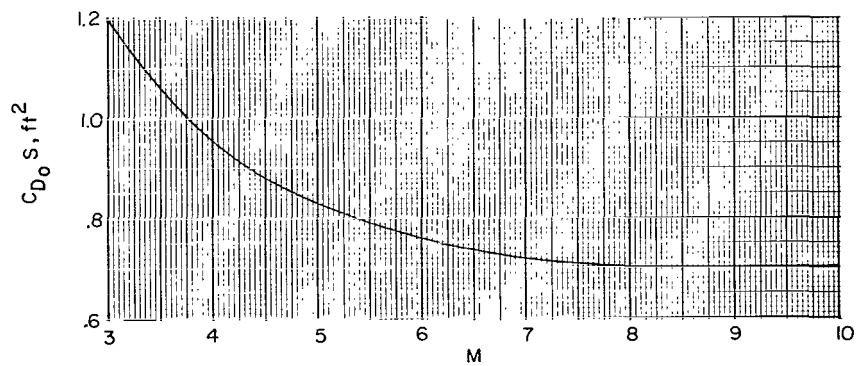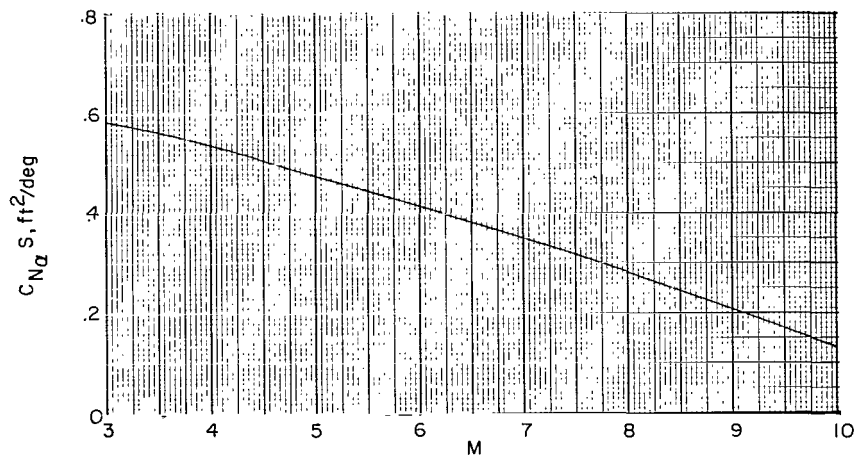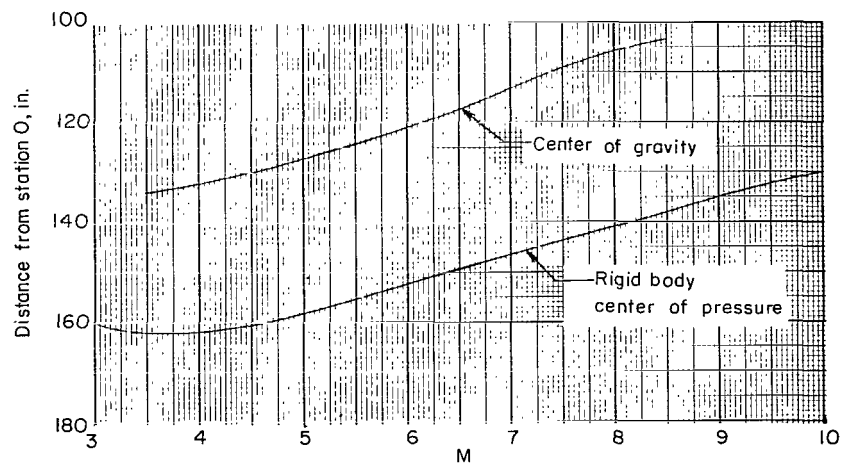
(b) Second stage.

Figure 27.- Continued.
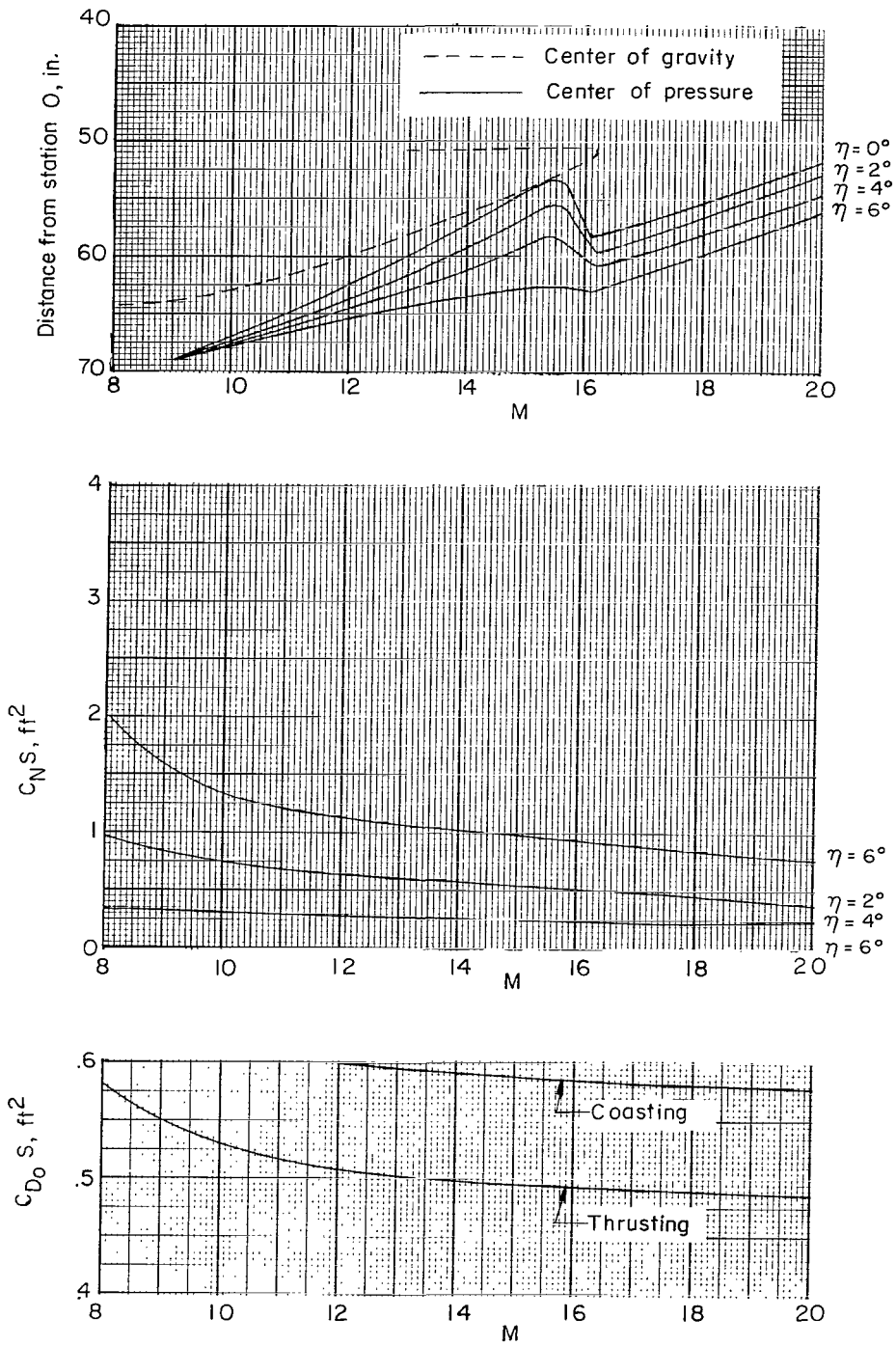
(c) Third-stage longitudinal aerodynamic characteristics with jet-plume effects.

Figure 27.- Concluded.
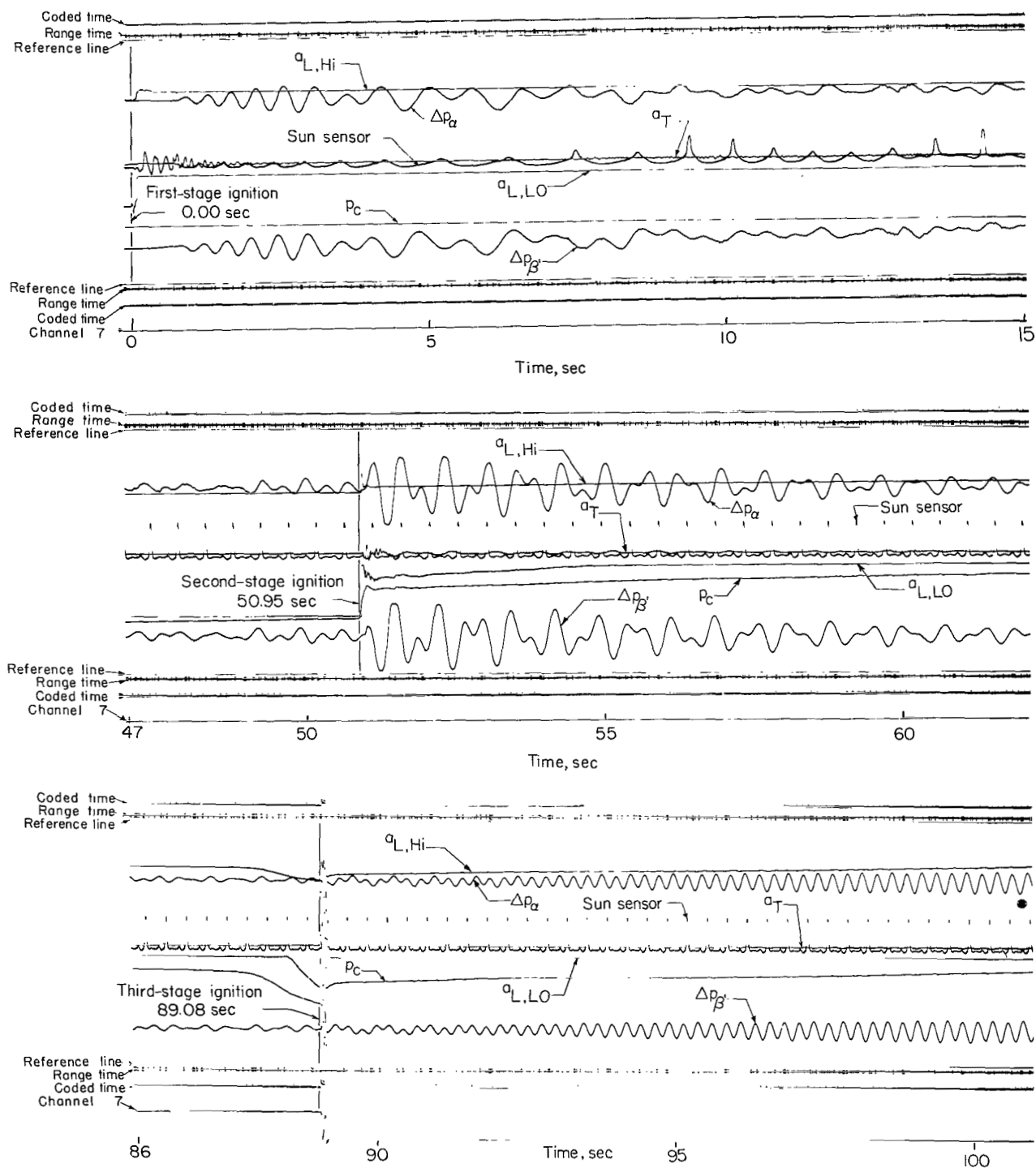
Figure 28.- Typical telemetry oscillograph record.
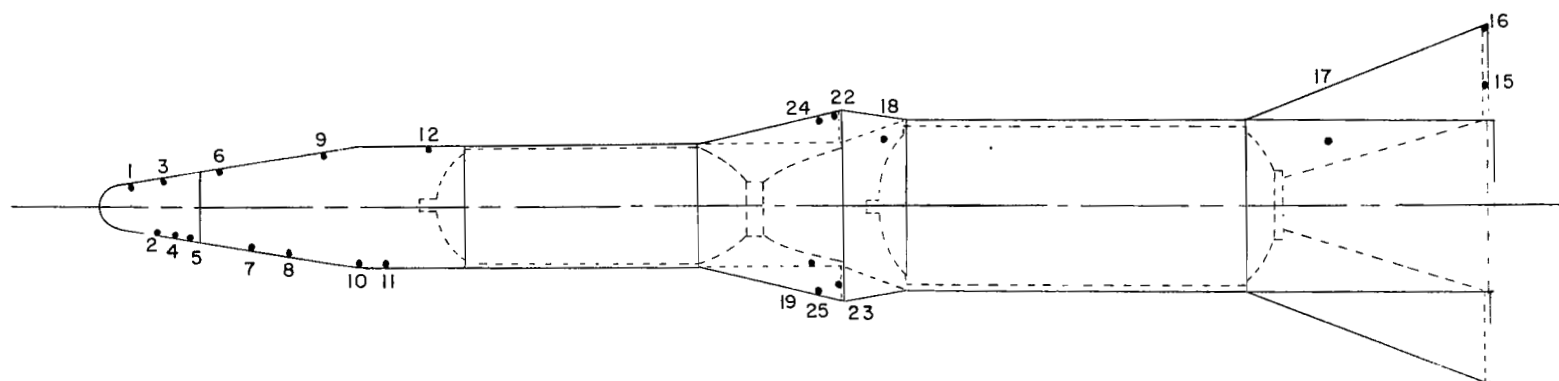
Figure 29.- Thermocouple locations. (See table 4 for details of thermocouple locations.)
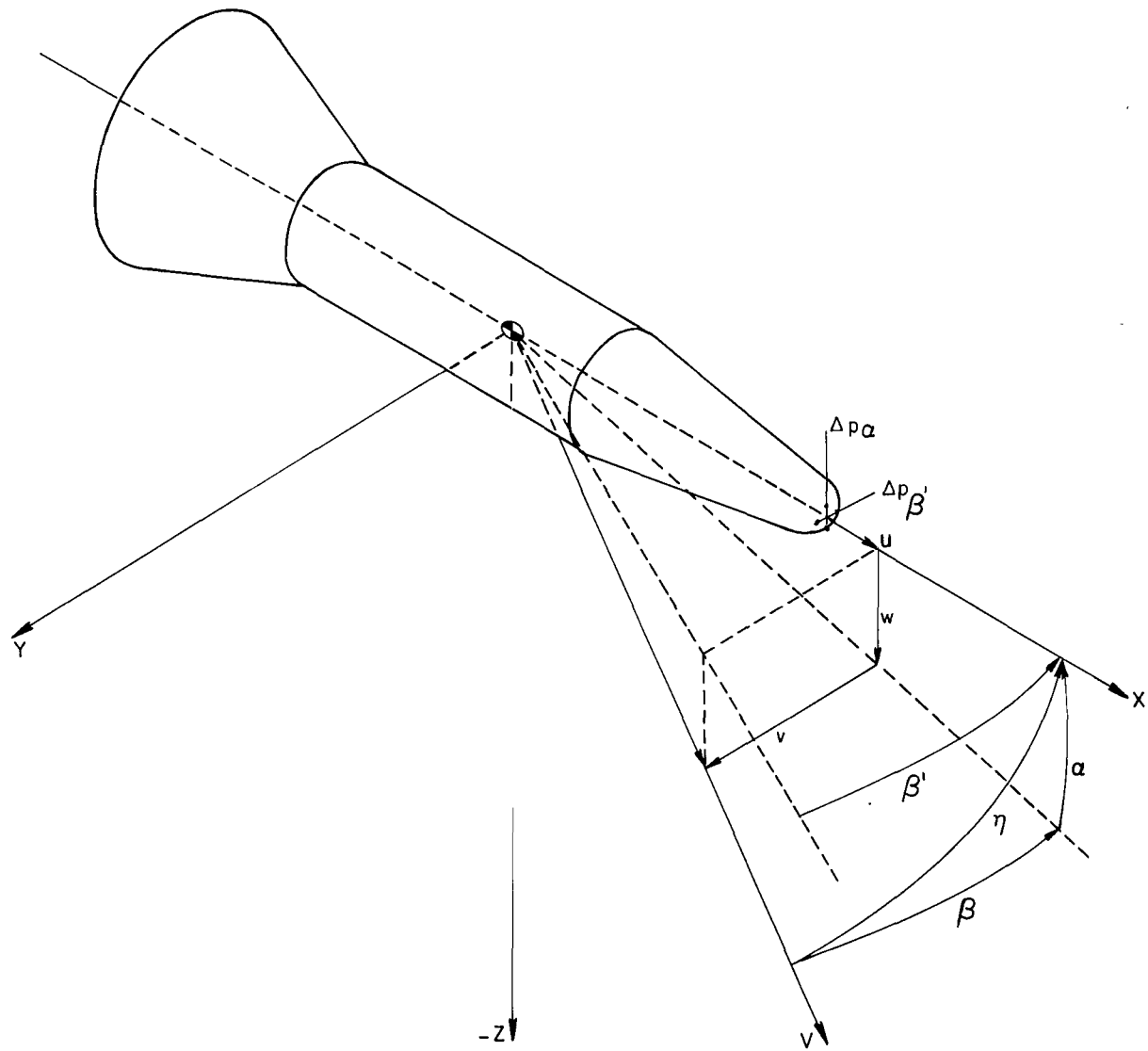
(a) Payload stage.

Figure 30.- Conventional axis systems.
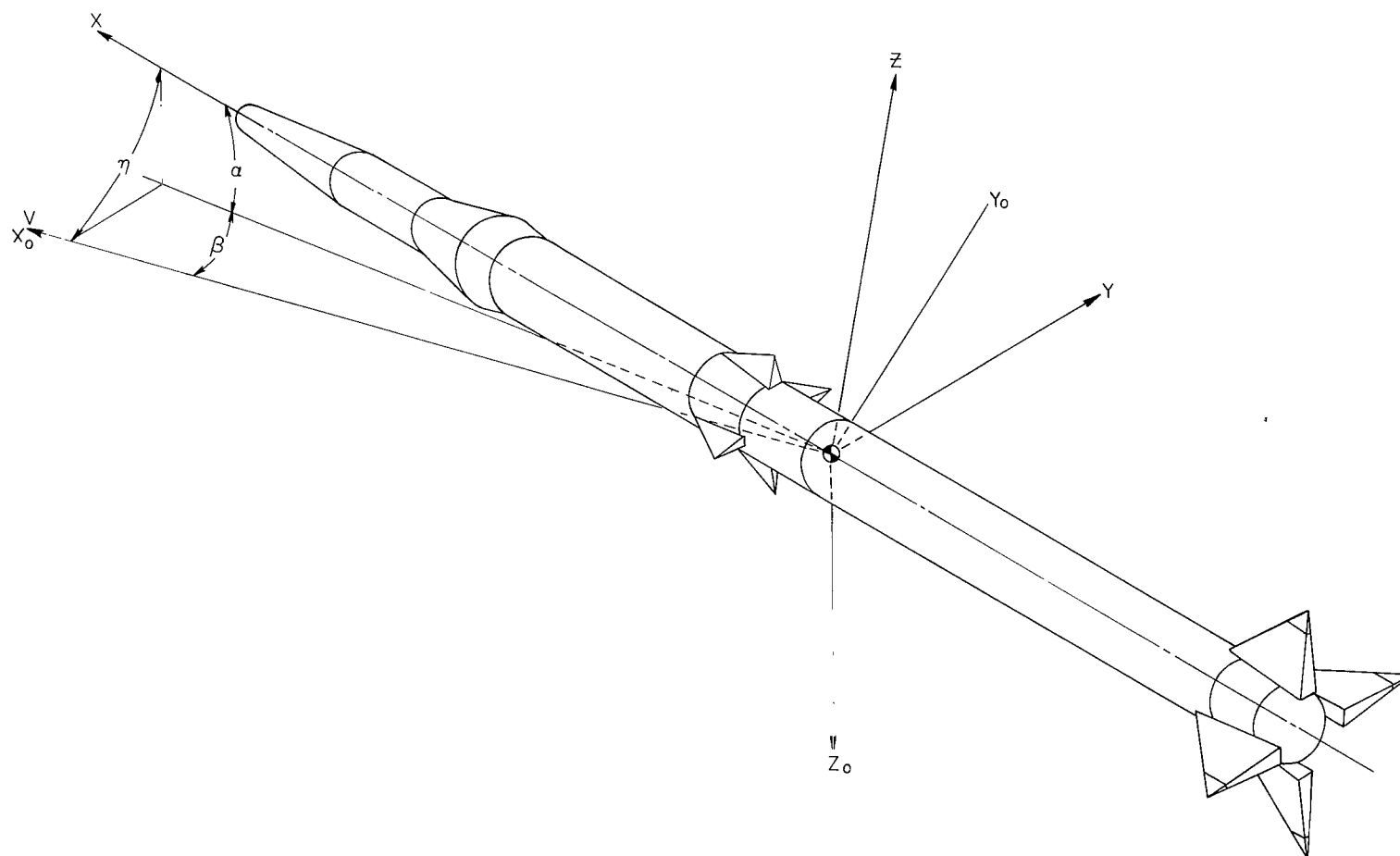
(b) Vehicle.

Figure 30.- Concluded.
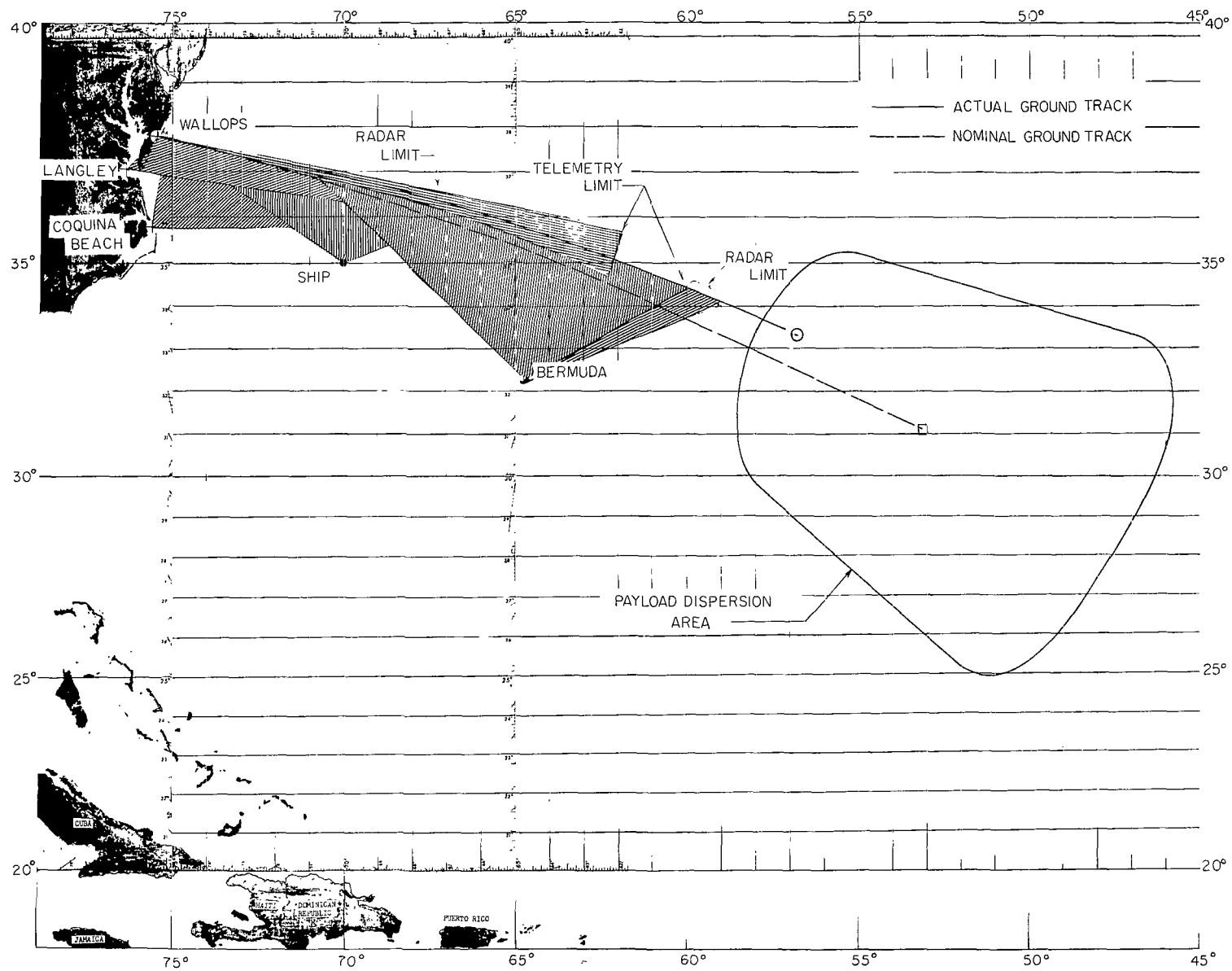
Figure 31.- Flight ground track and tracking stations.
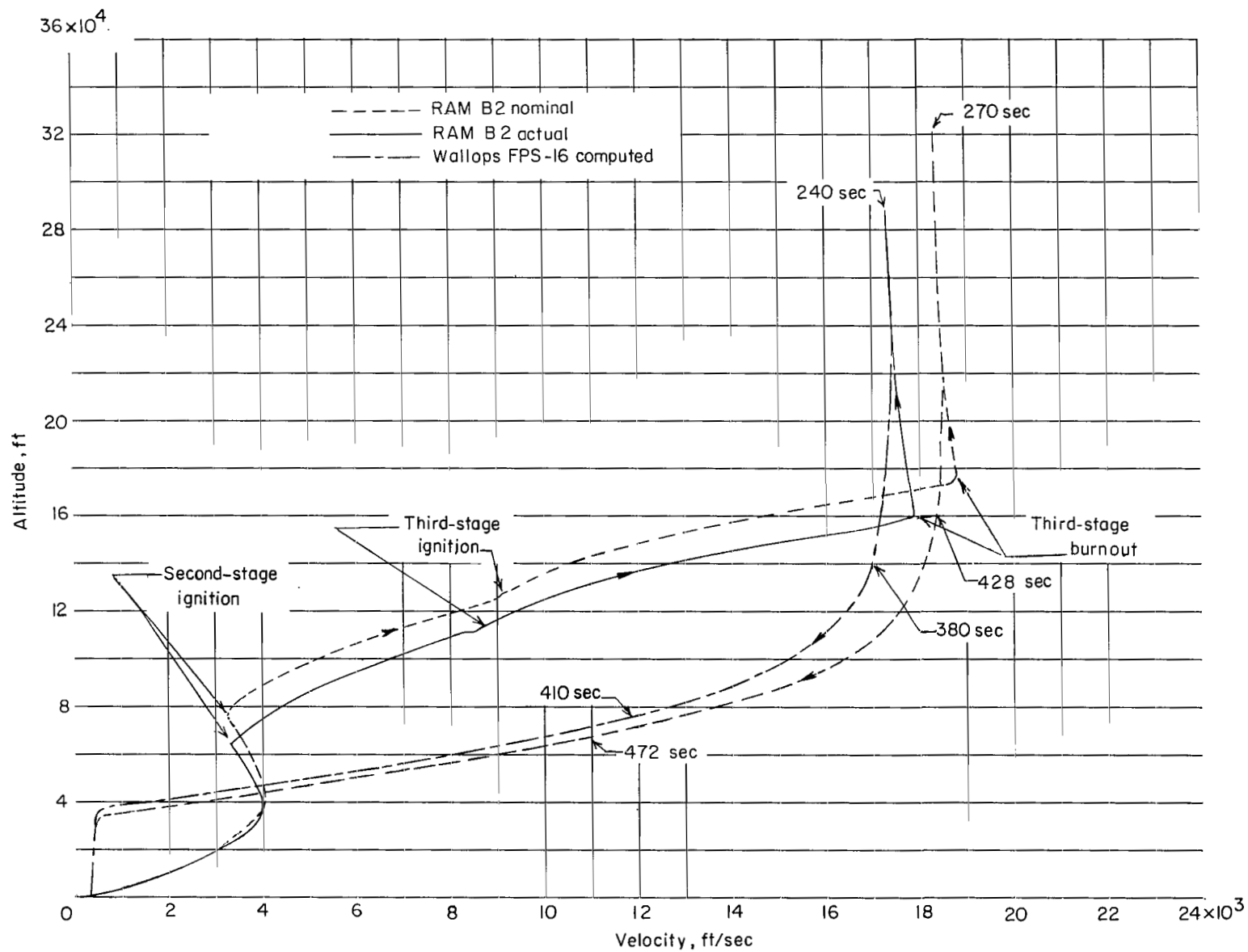
Figure 32.- RAM B2 nominal and actual altitude-velocity profiles.
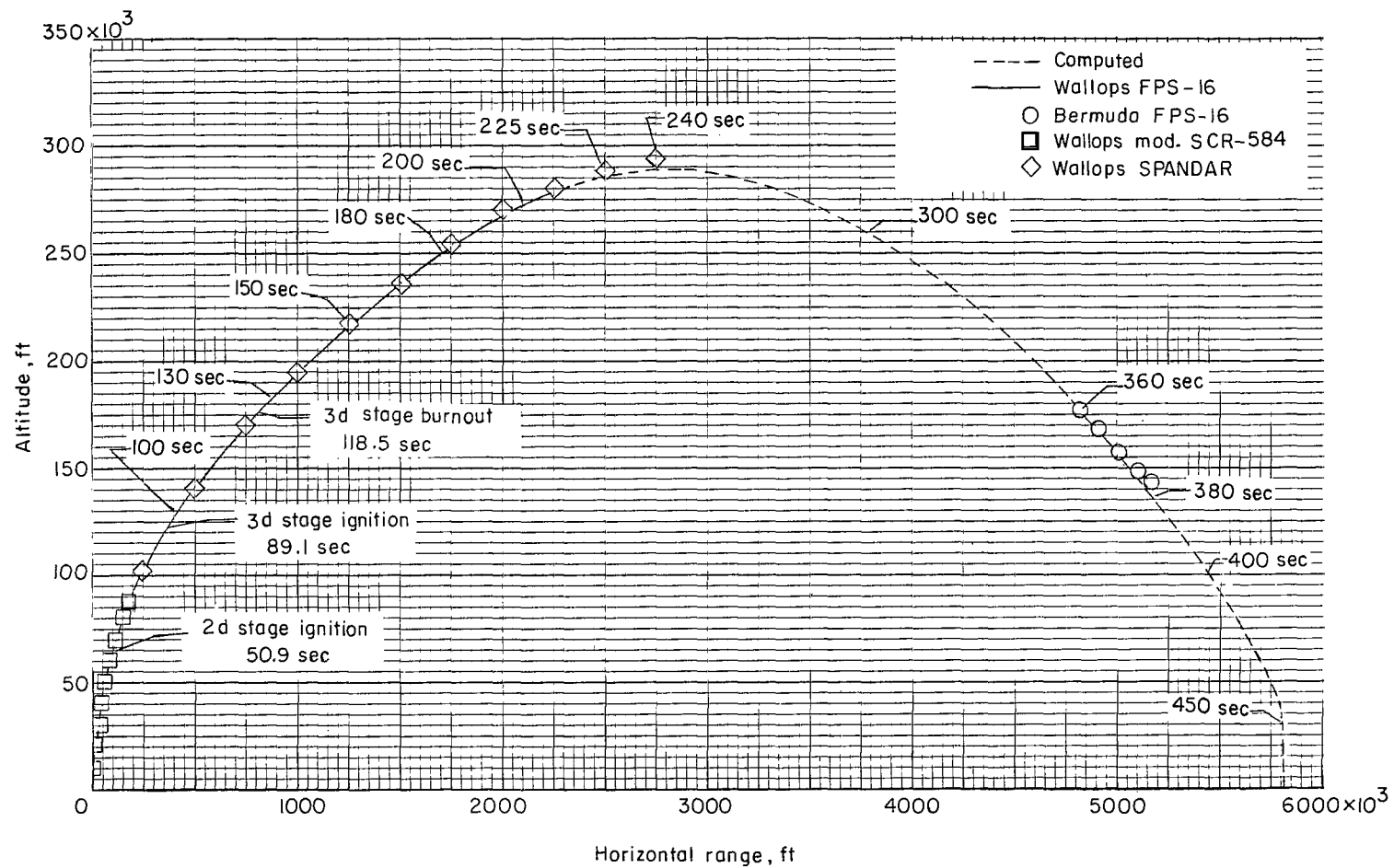
Figure 33.- Actual altitude—horizontal-range path.
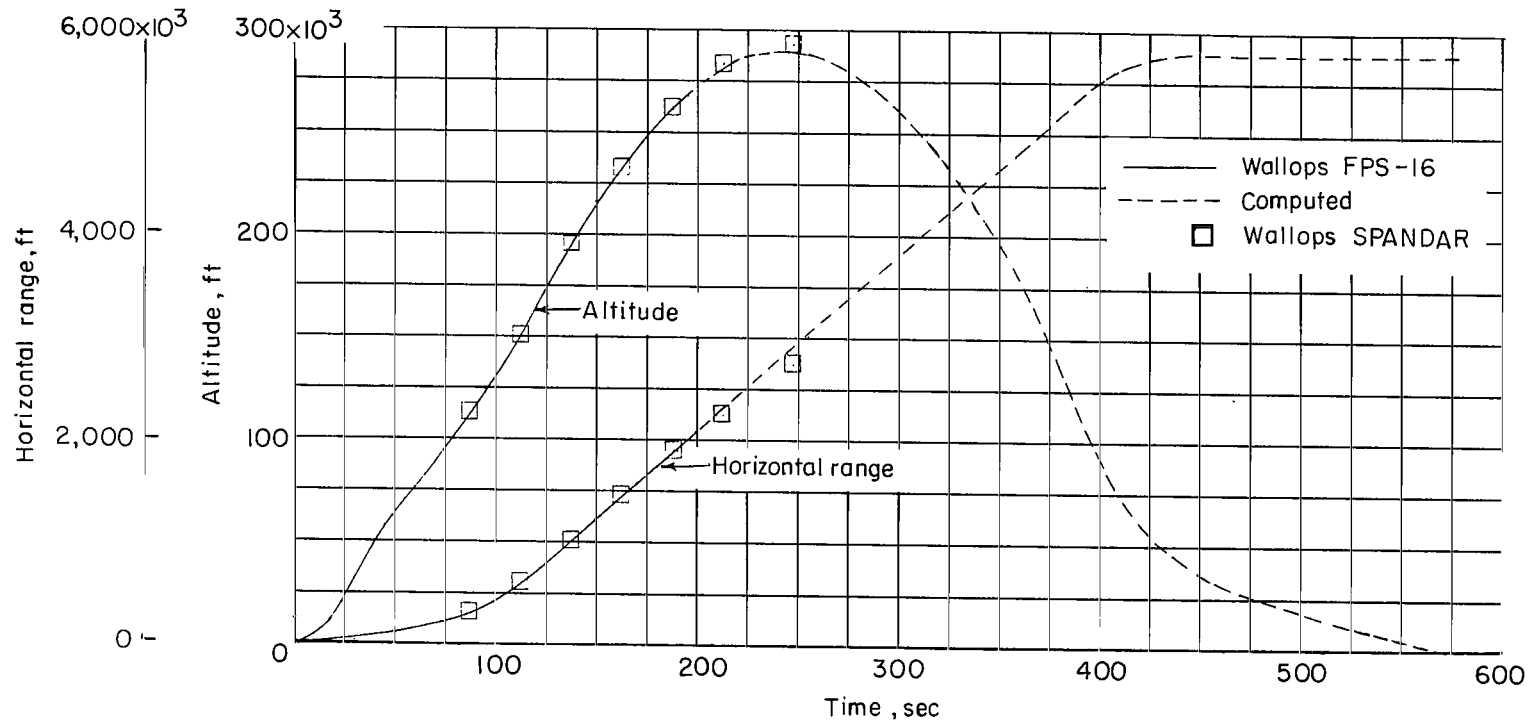
(a) Space position.

Figure 34.- Radar space position and velocity.
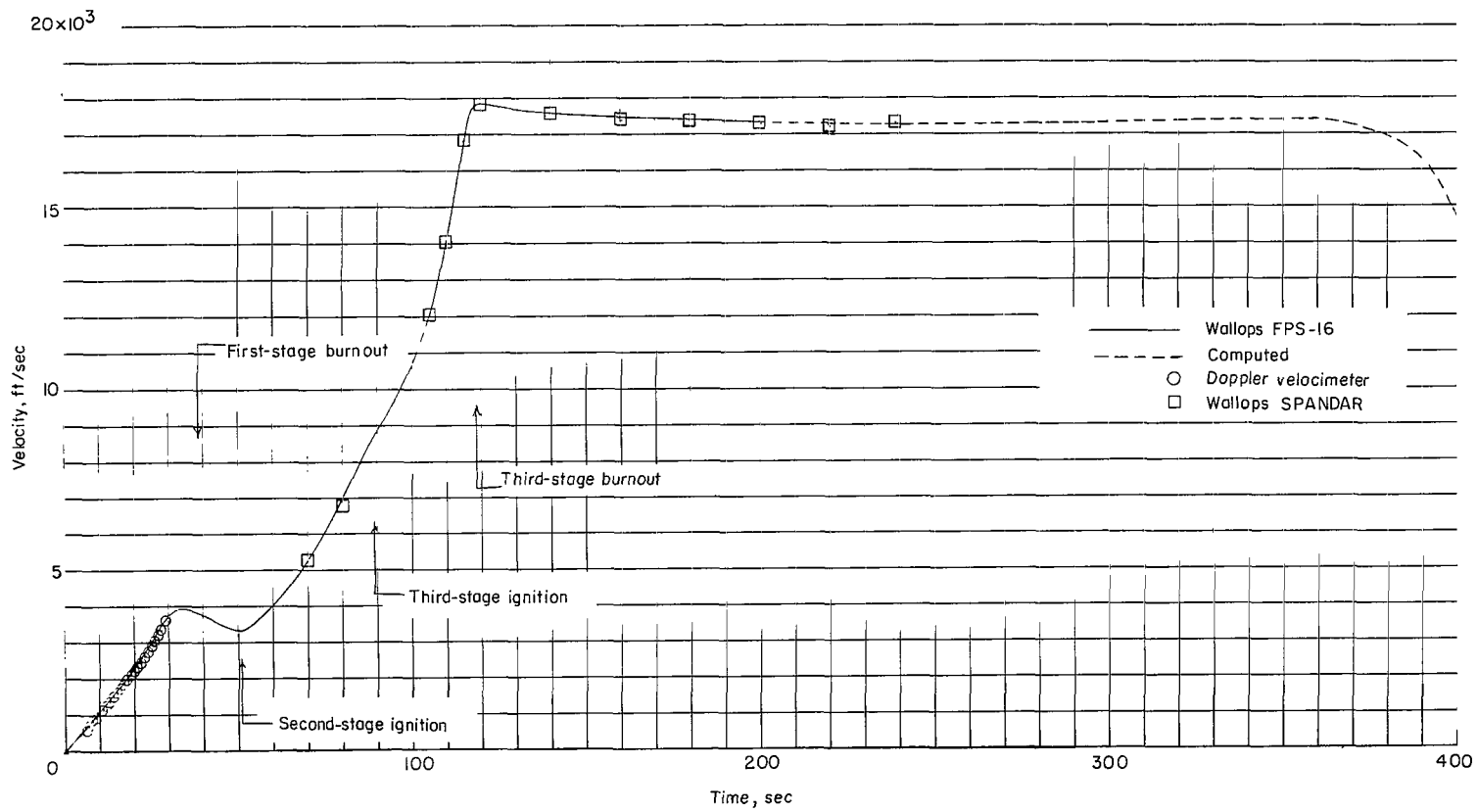
(b) Velocity history.

Figure 34.- Concluded.
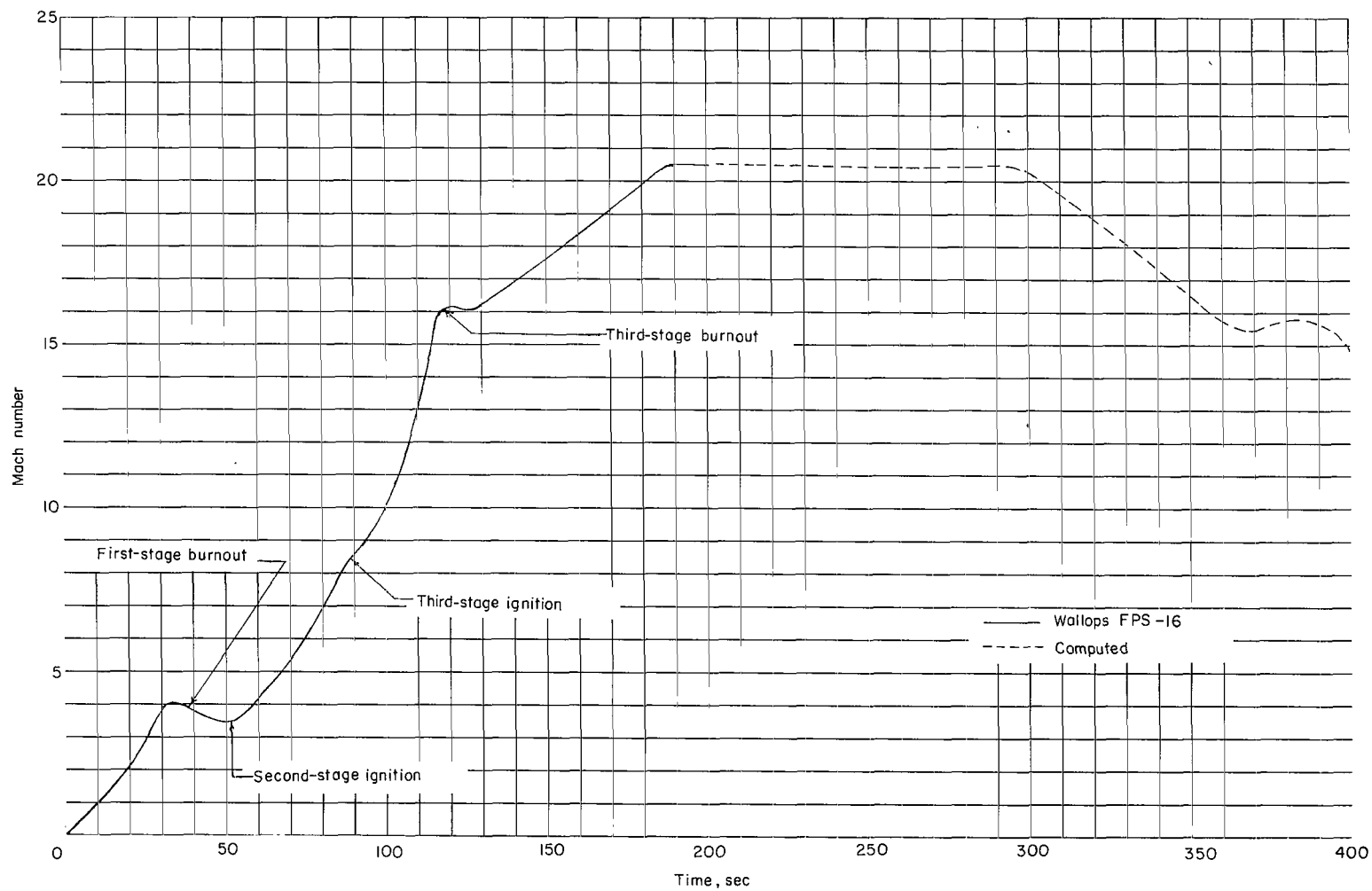
Figure 35.- Mach number time history determined from Wallops FPS-16 radar data and ARDC 1959 model atmosphere.
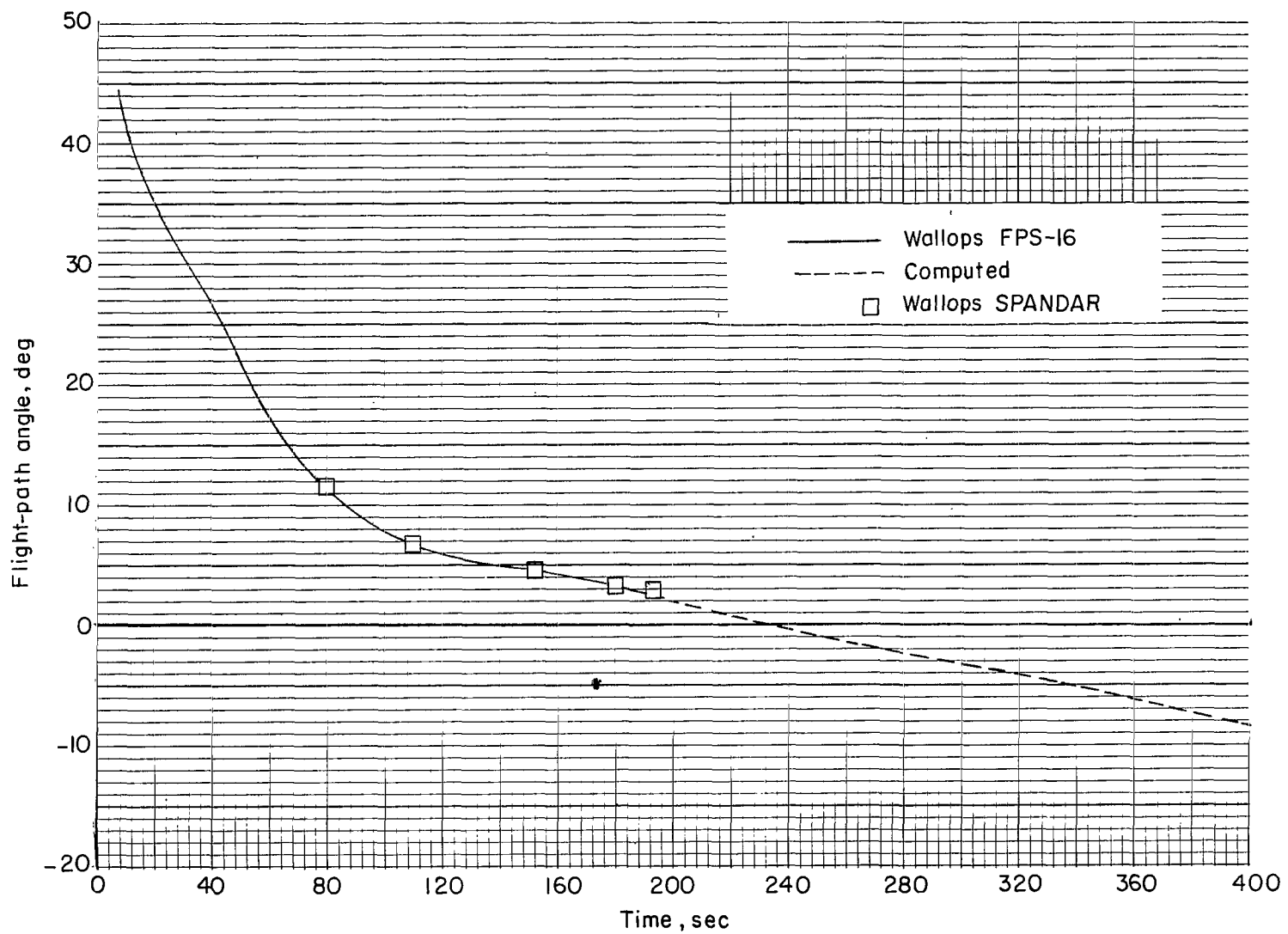
Figure 36.- Flight-path-angle time history.
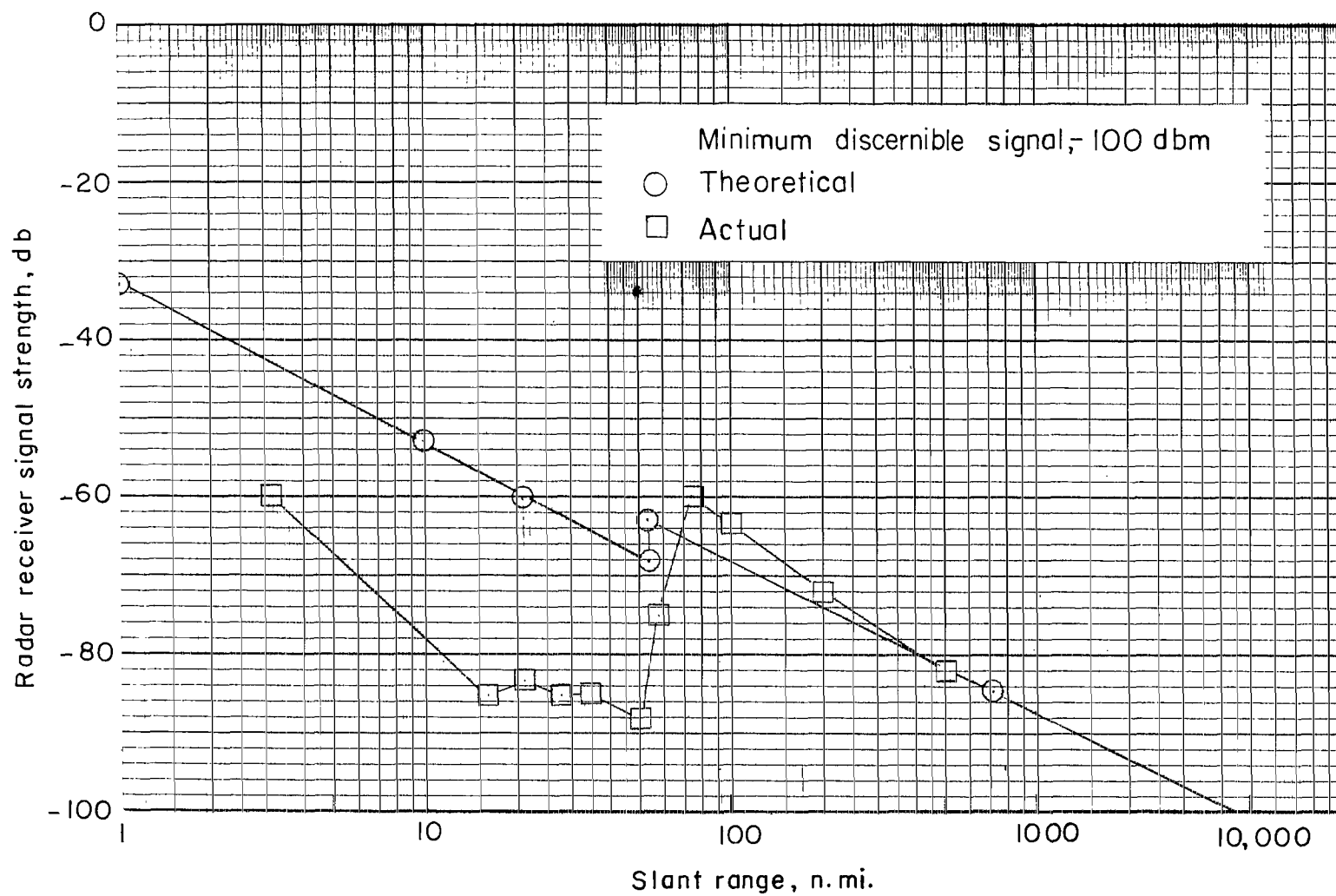
Figure 37.- The FPS-16 radar received signal as a function of slant range.
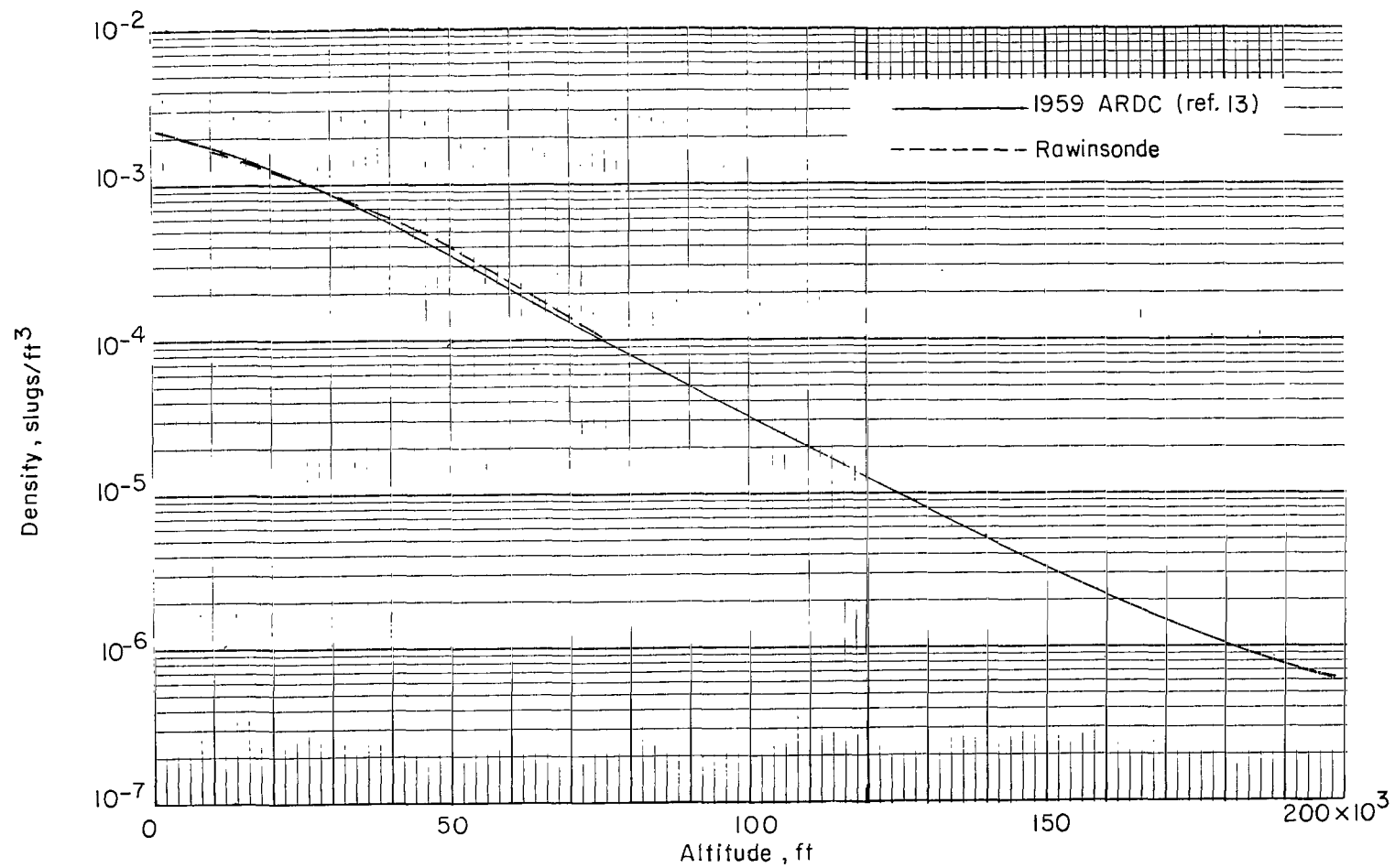
Figure 38.- Variation of atmospheric density with altitude.
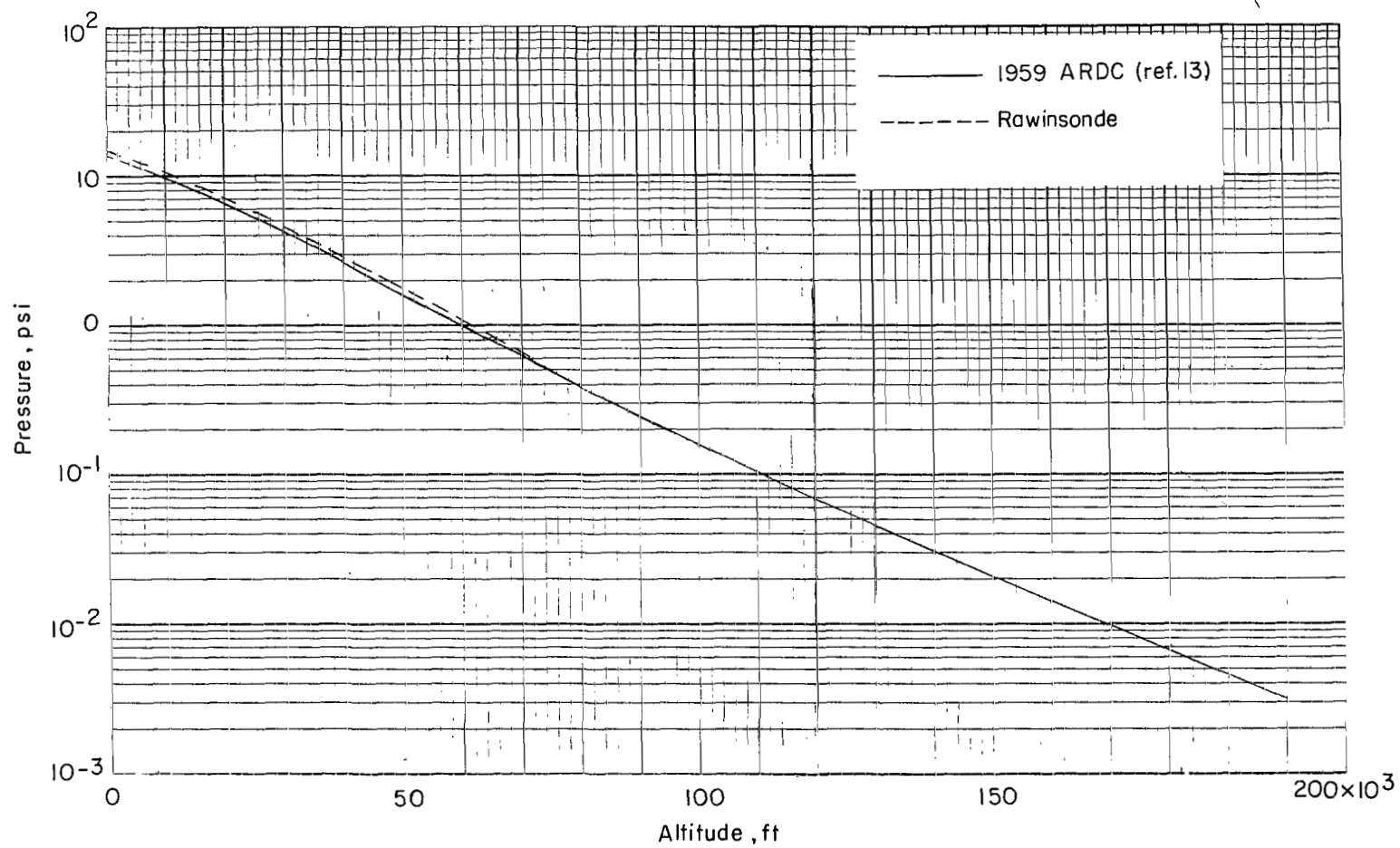
Figure 39.- Variation of atmospheric pressure with altitude.
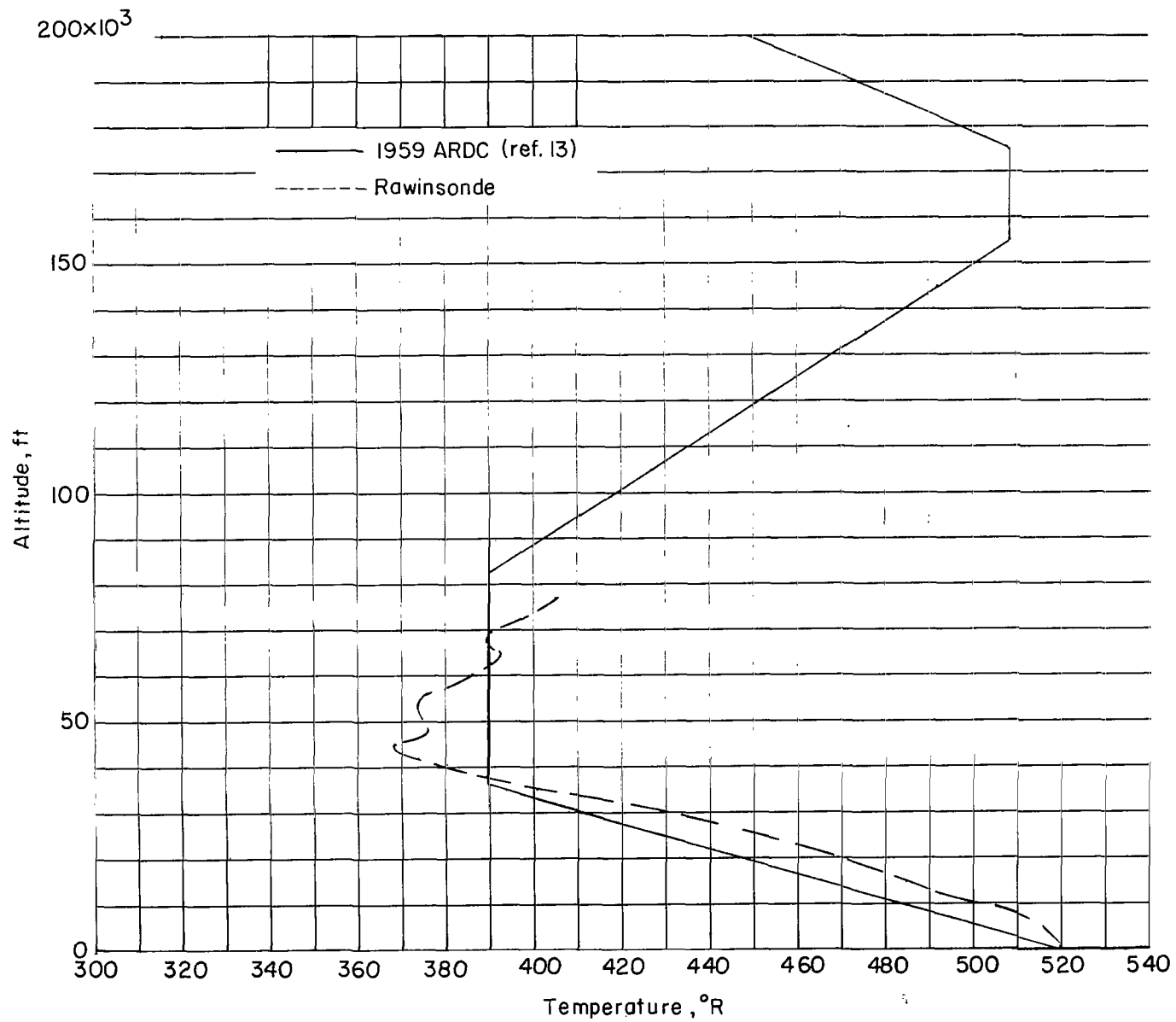
Figure 40.- Temperature at various altitudes.
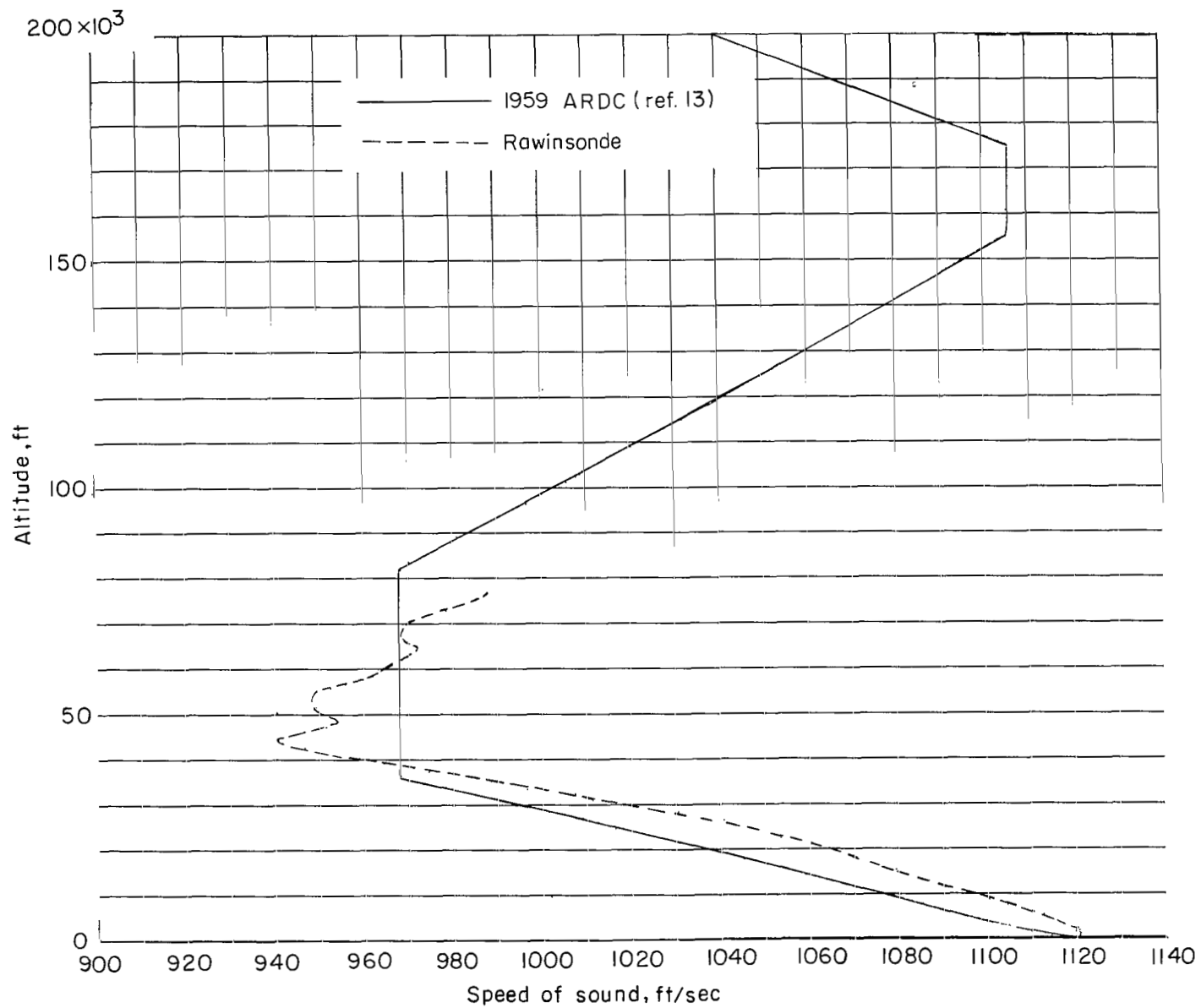
Figure 41.- Speed of sound at various altitudes.
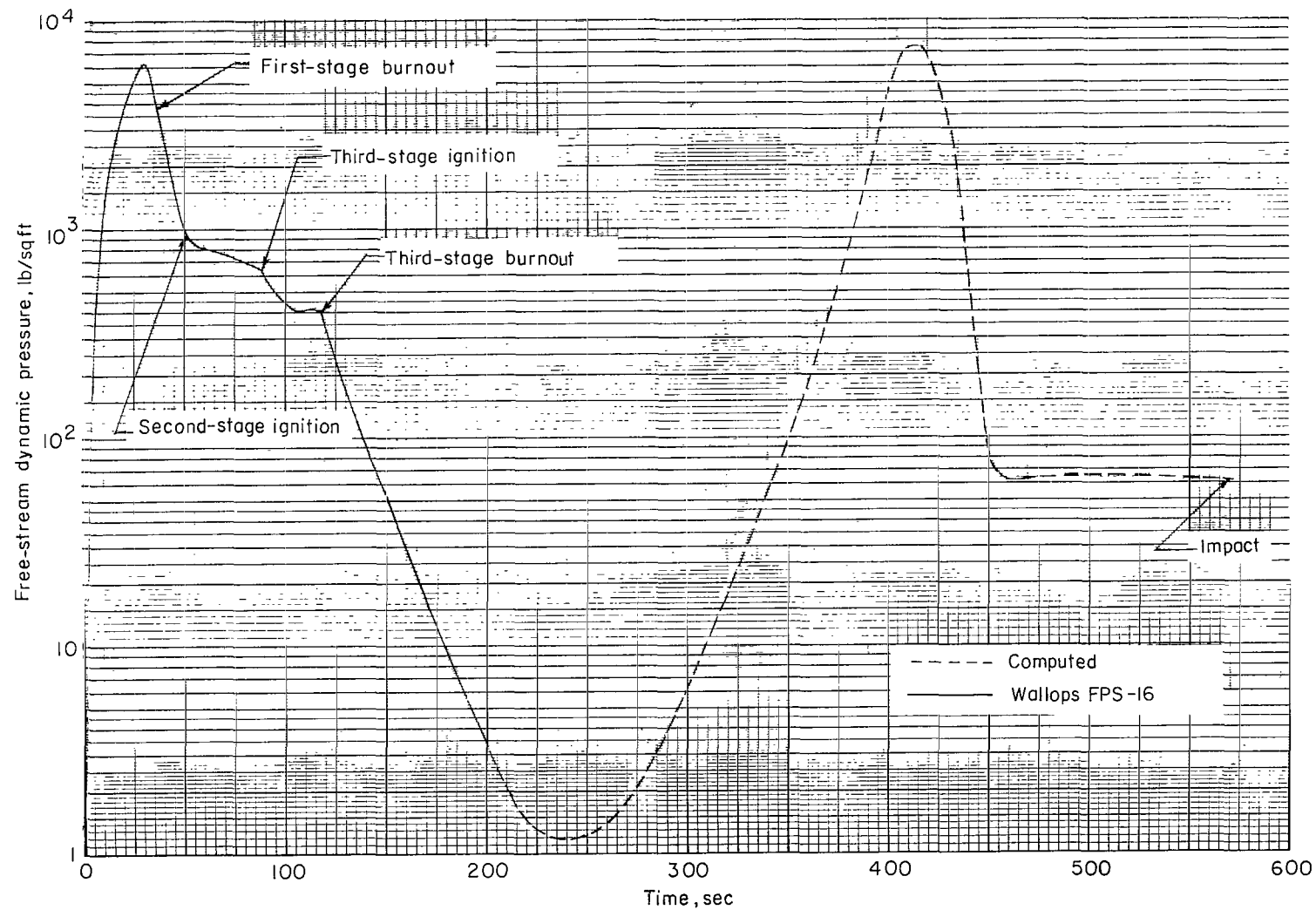
Figure 42.- Variation of free-stream dynamic pressure with time.
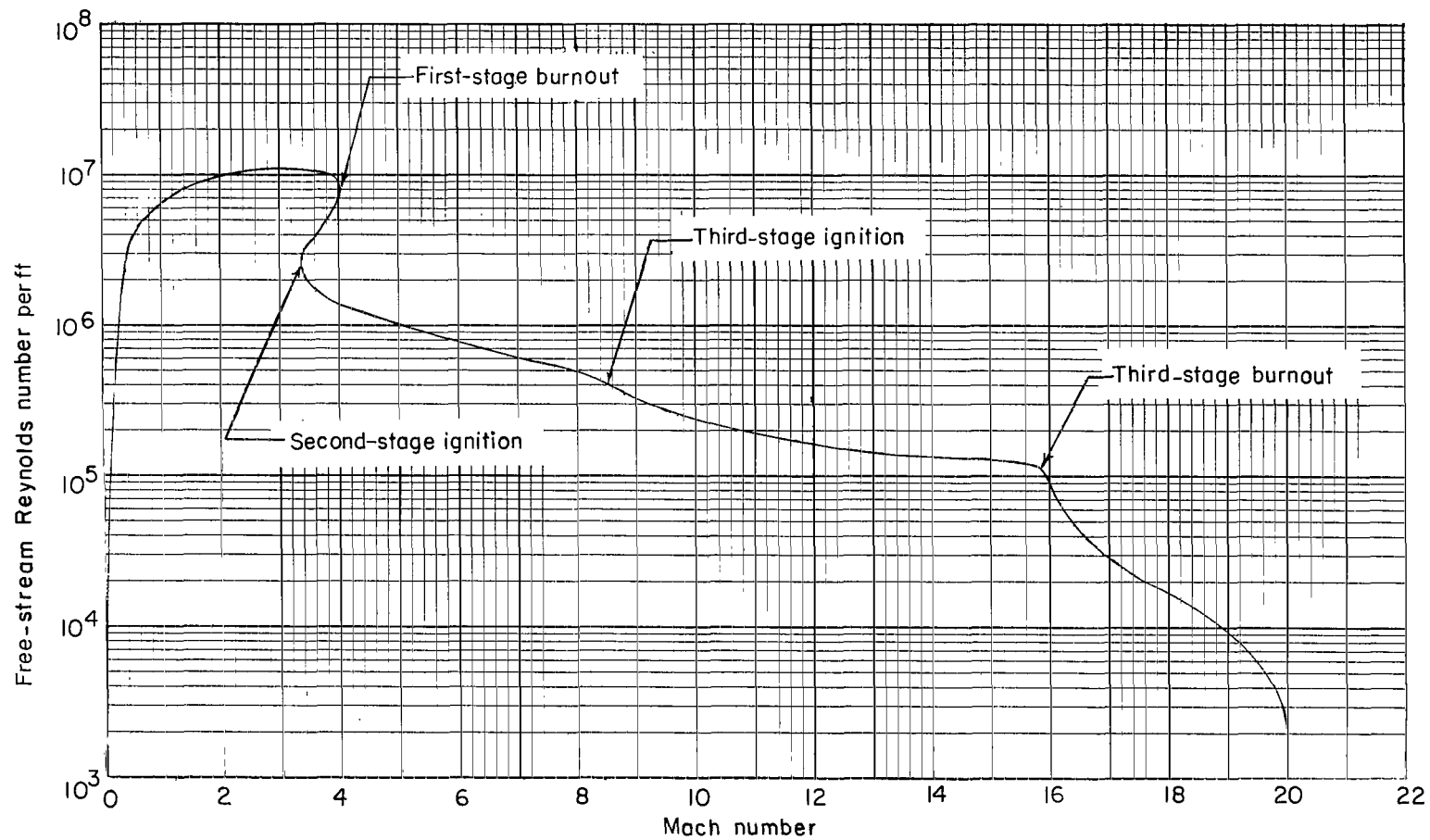
Figure 43.- Variation of free-stream Reynolds number with Mach number.
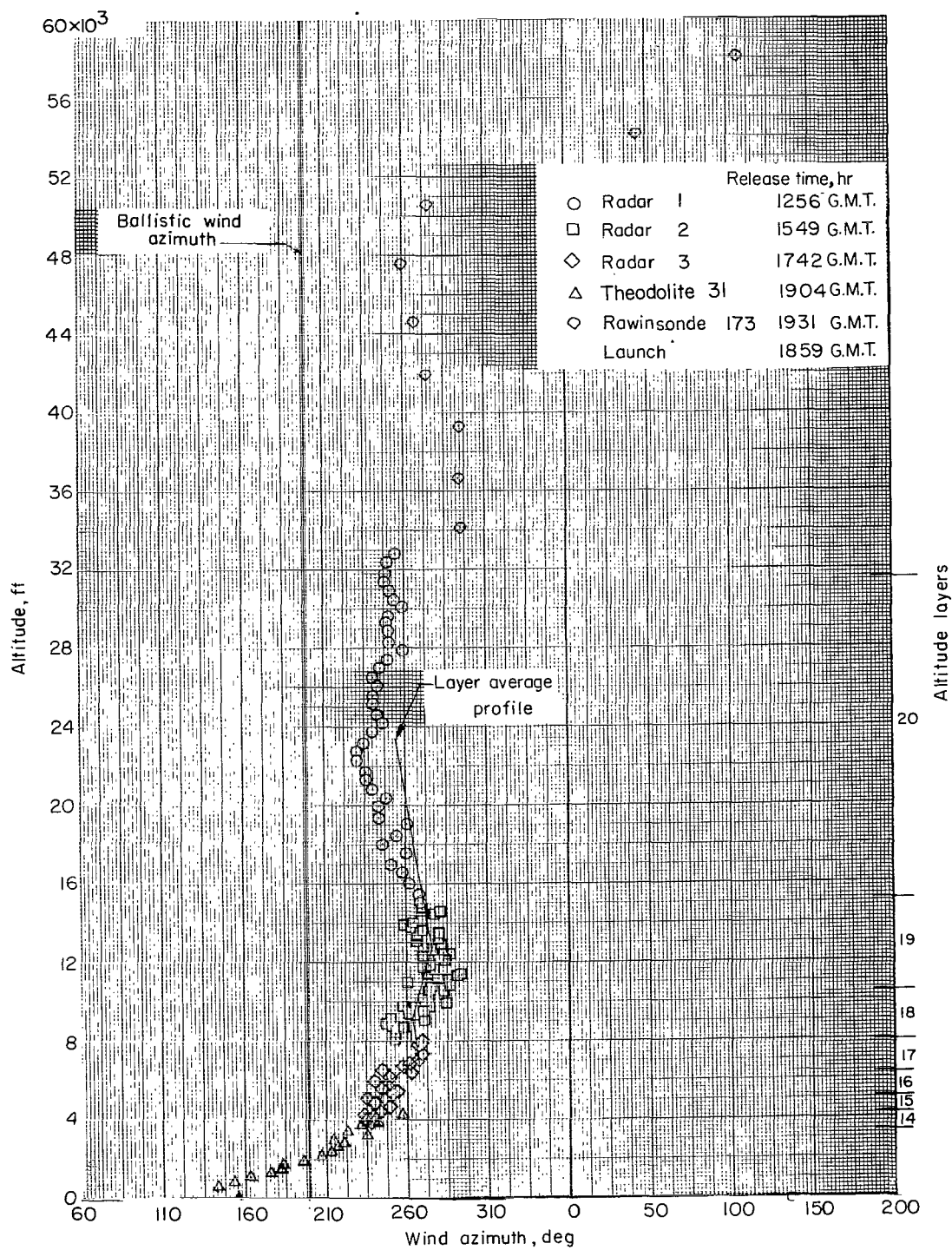
Figure 44.- Wind azimuth at various altitudes.
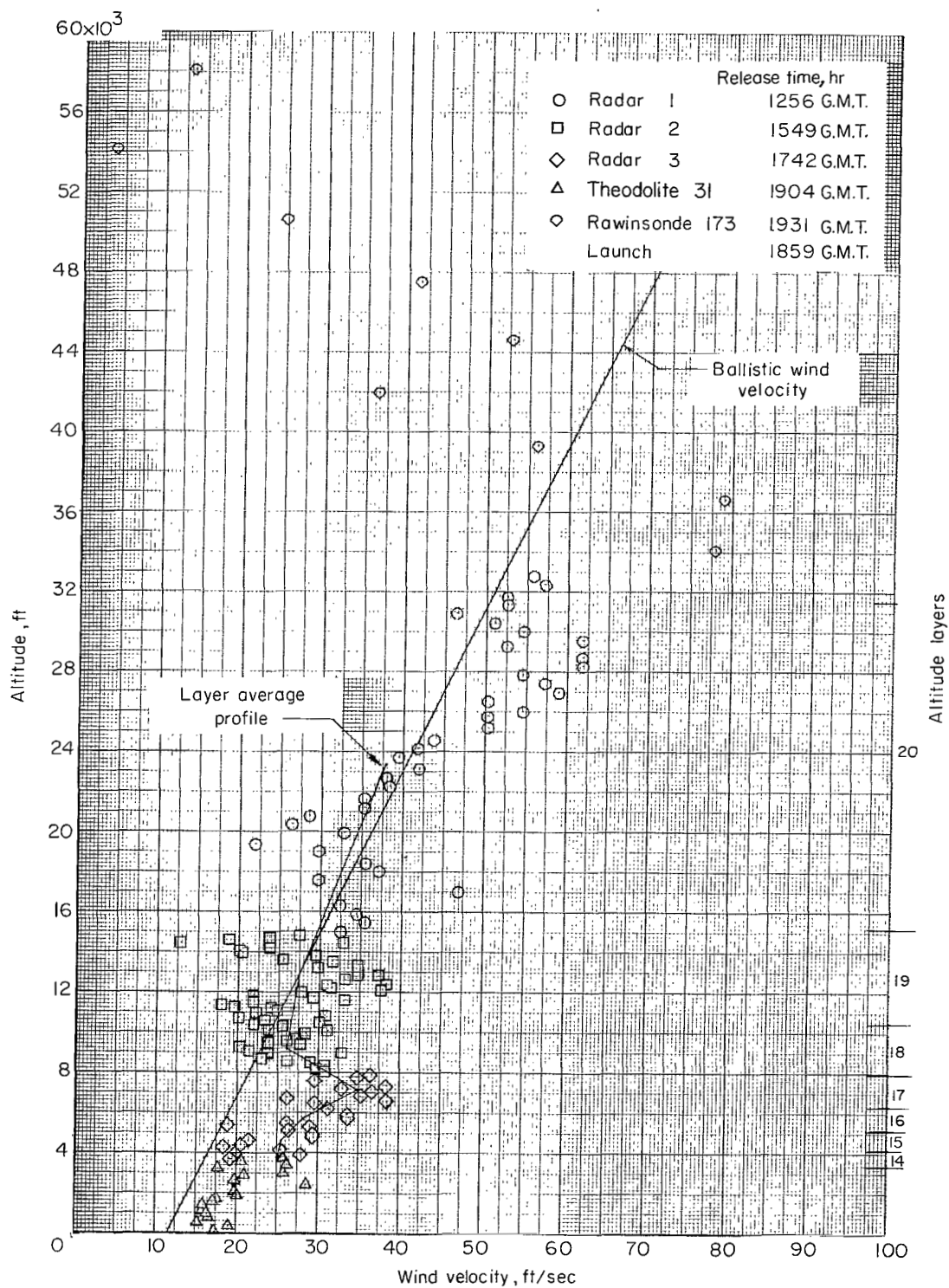
Figure 45.- Wind velocity at various altitudes.
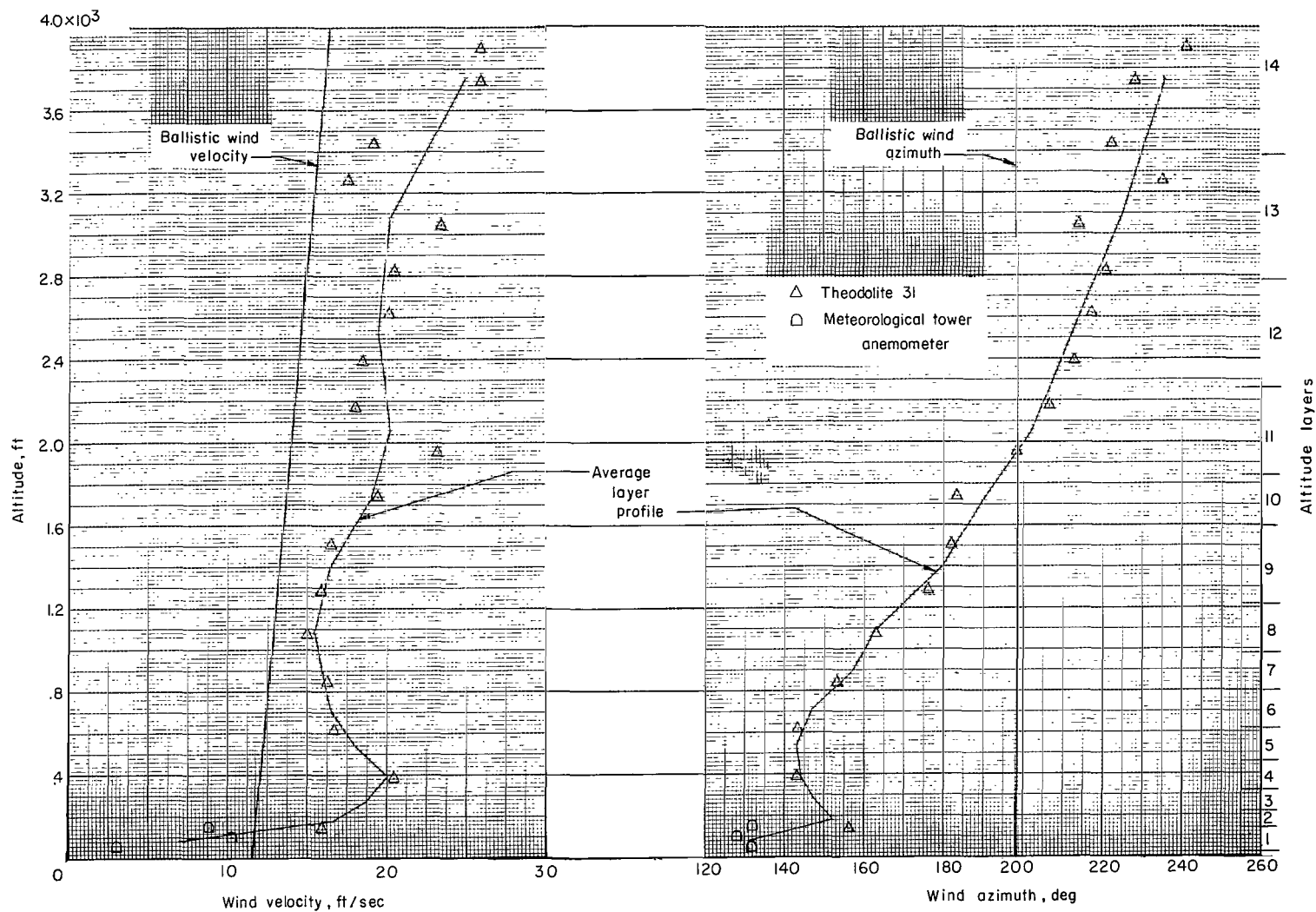
Figure 46.- Wind velocity and azimuth at various altitudes.
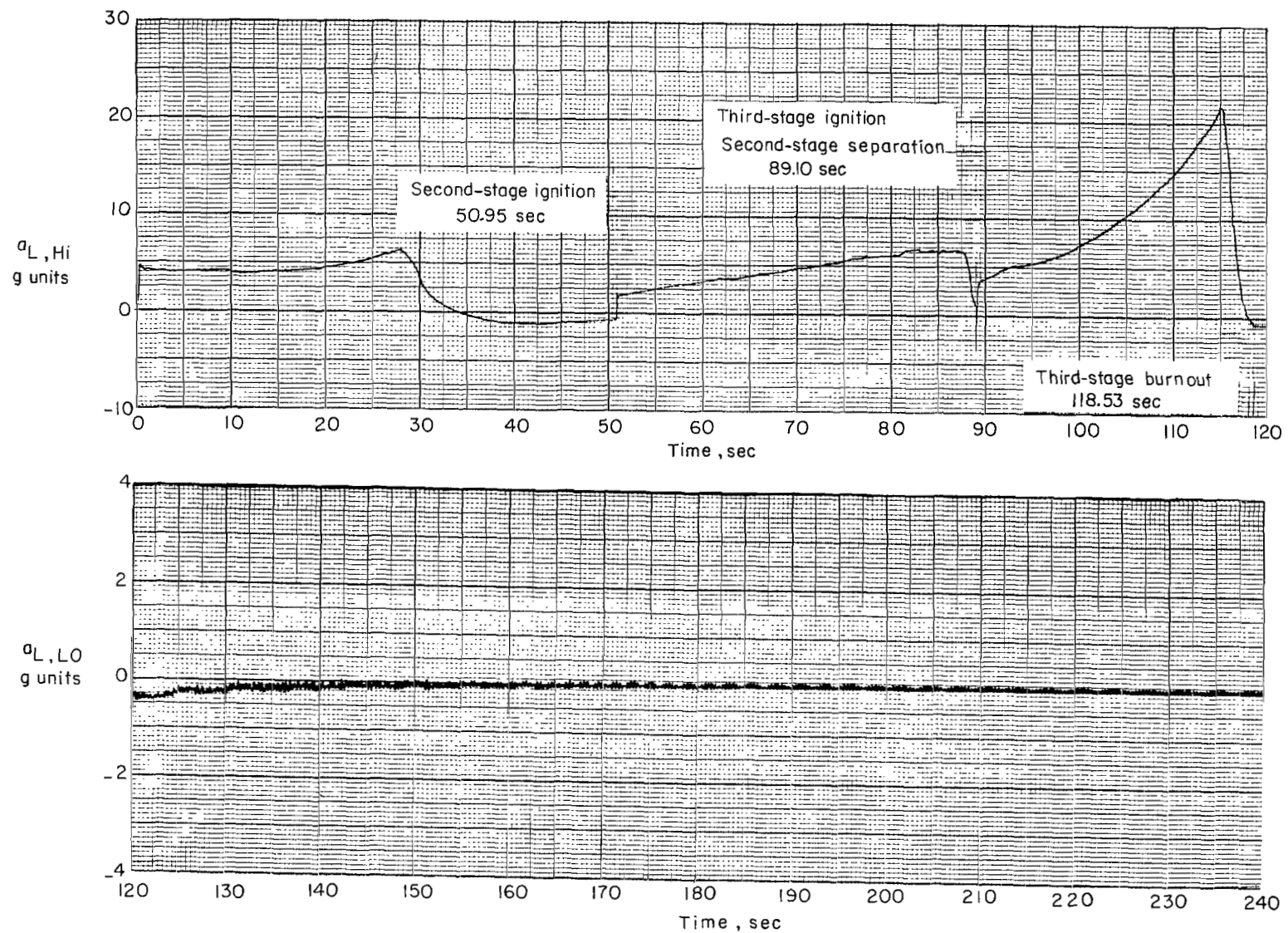
Figure 47.- Variation of longitudinal acceleration with time.
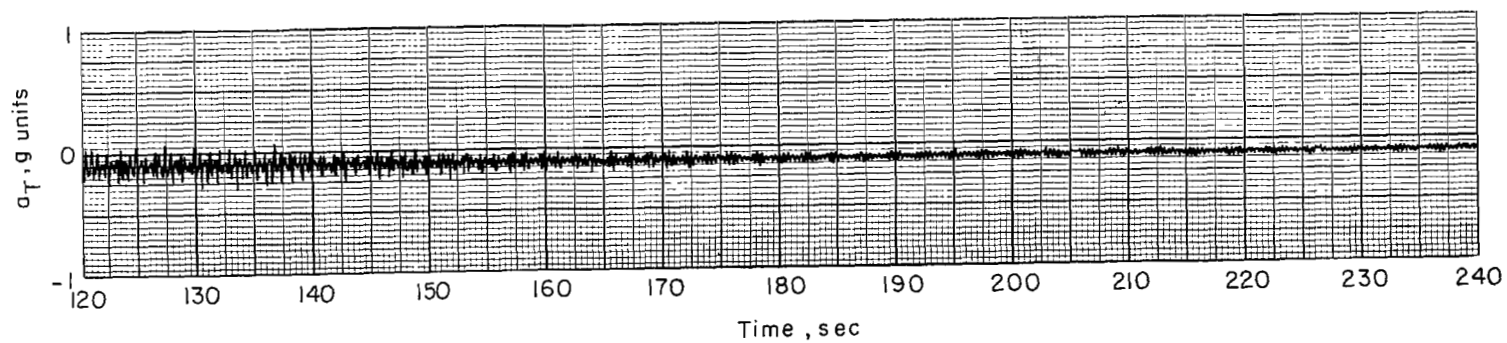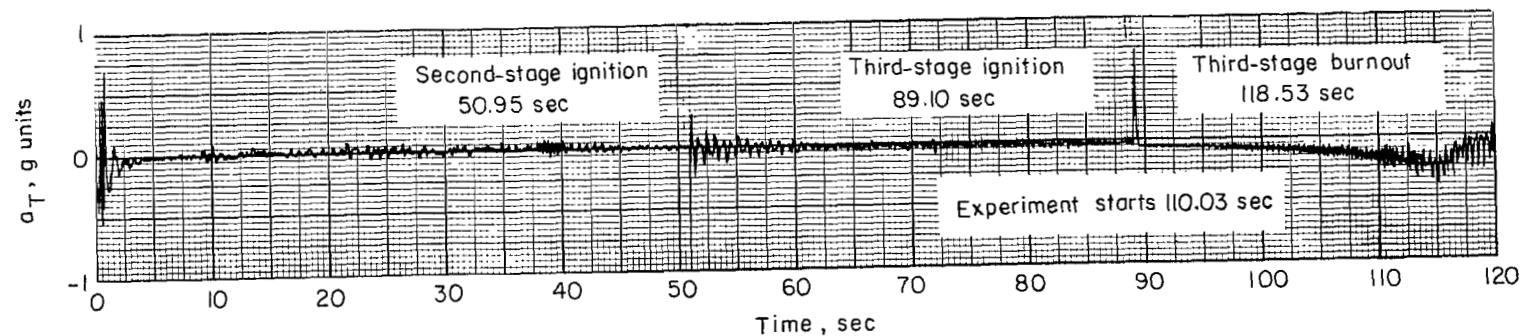
Figure 48.- Variation of transverse acceleration with time.
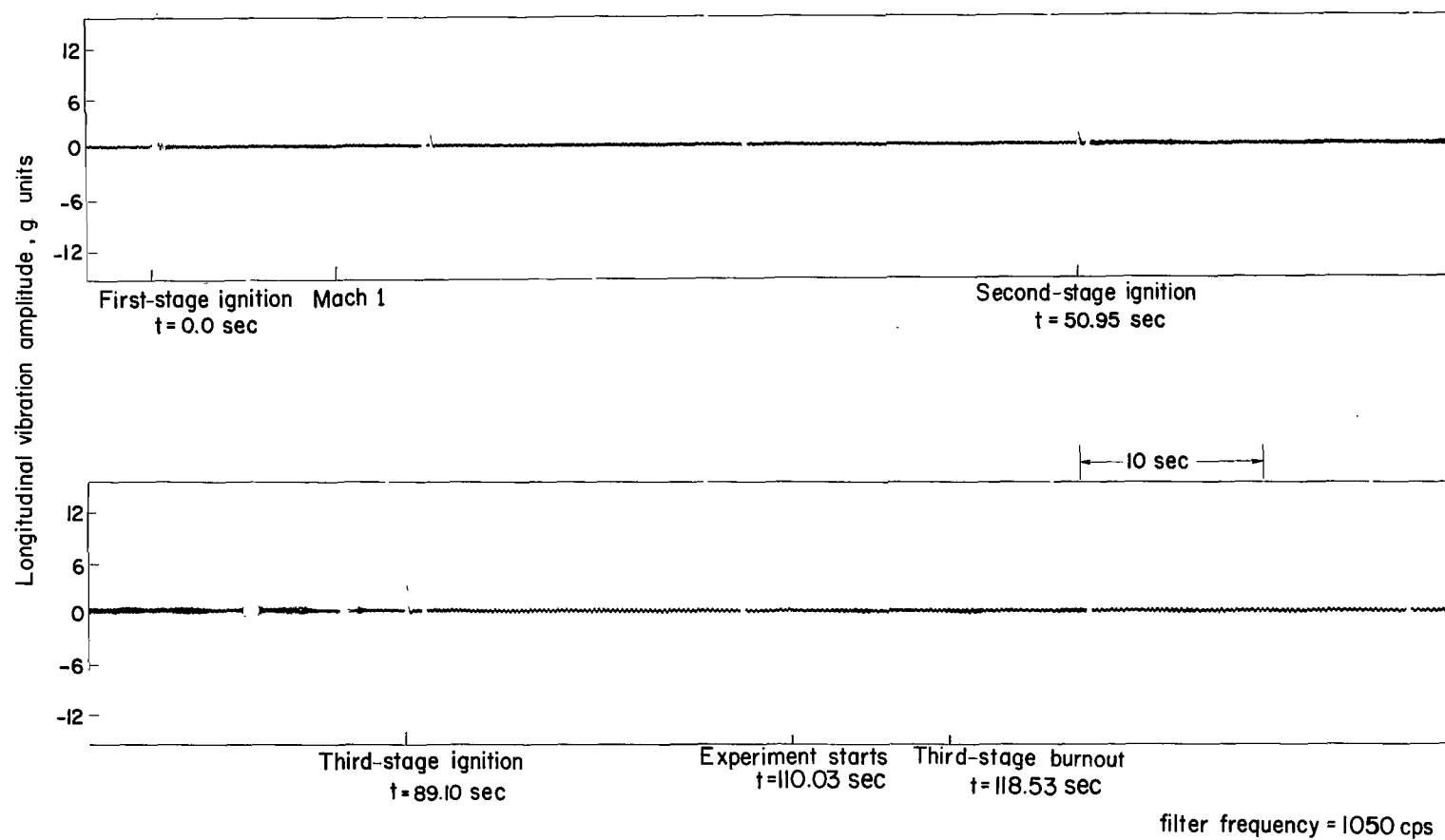
Figure 49.- Longitudinal vibration flight history. Filter frequency = 1050 cps.
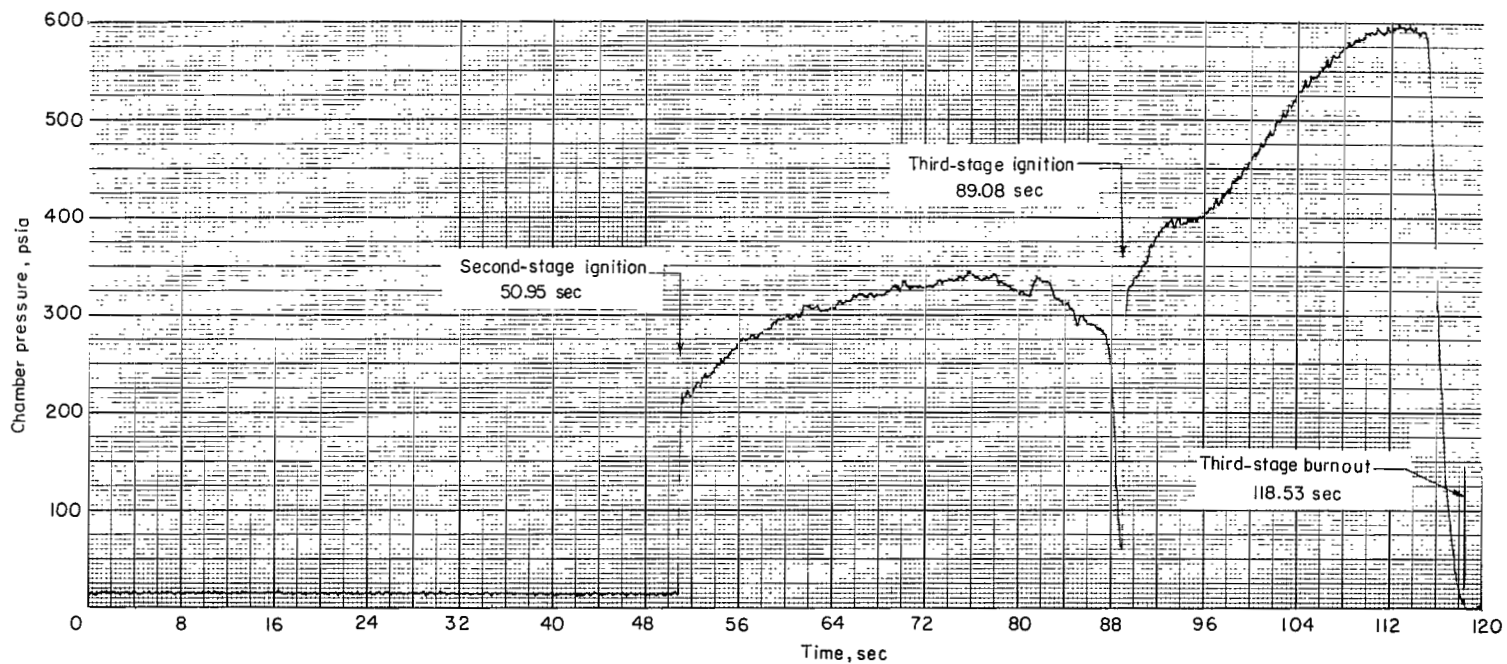
Figure 50.- Second- and third-stage-motor chamber-pressure time histories.
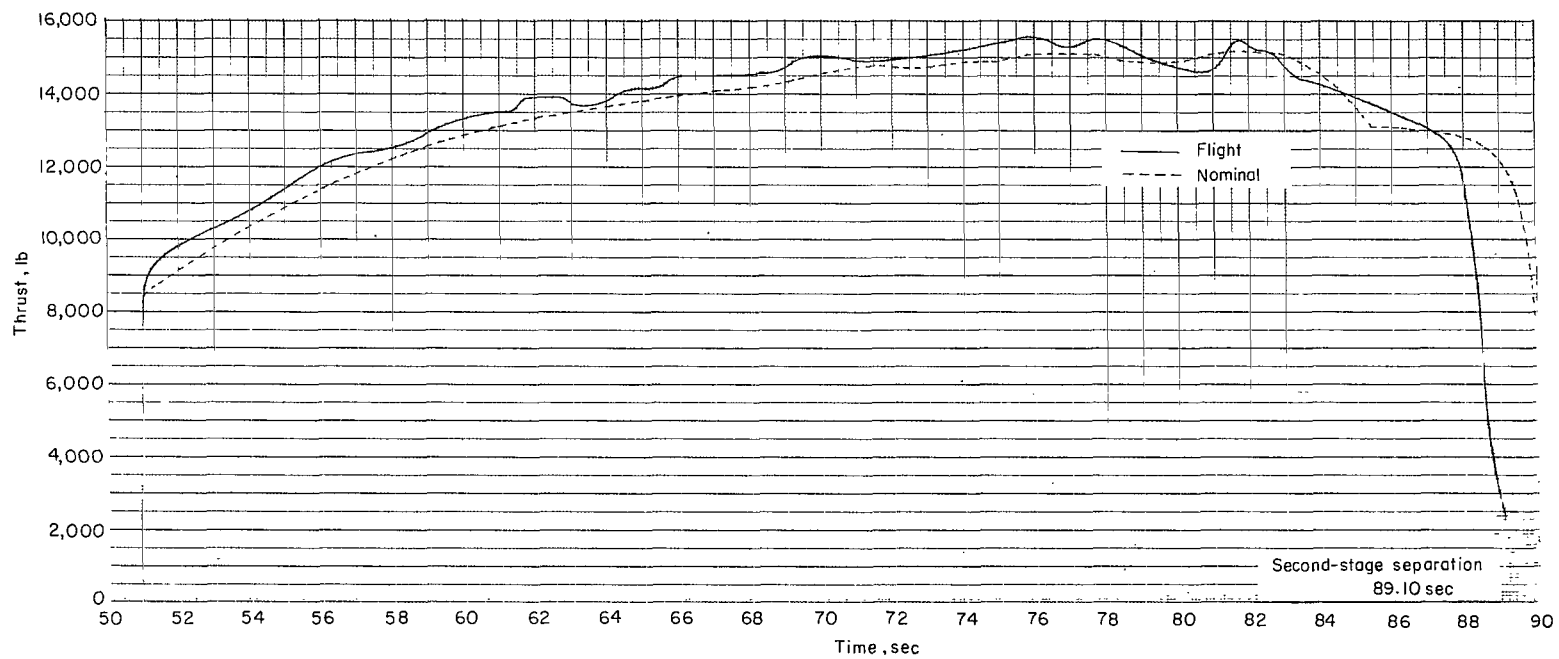
Figure 51.- Comparison of second-stage flight and nominal thrust.
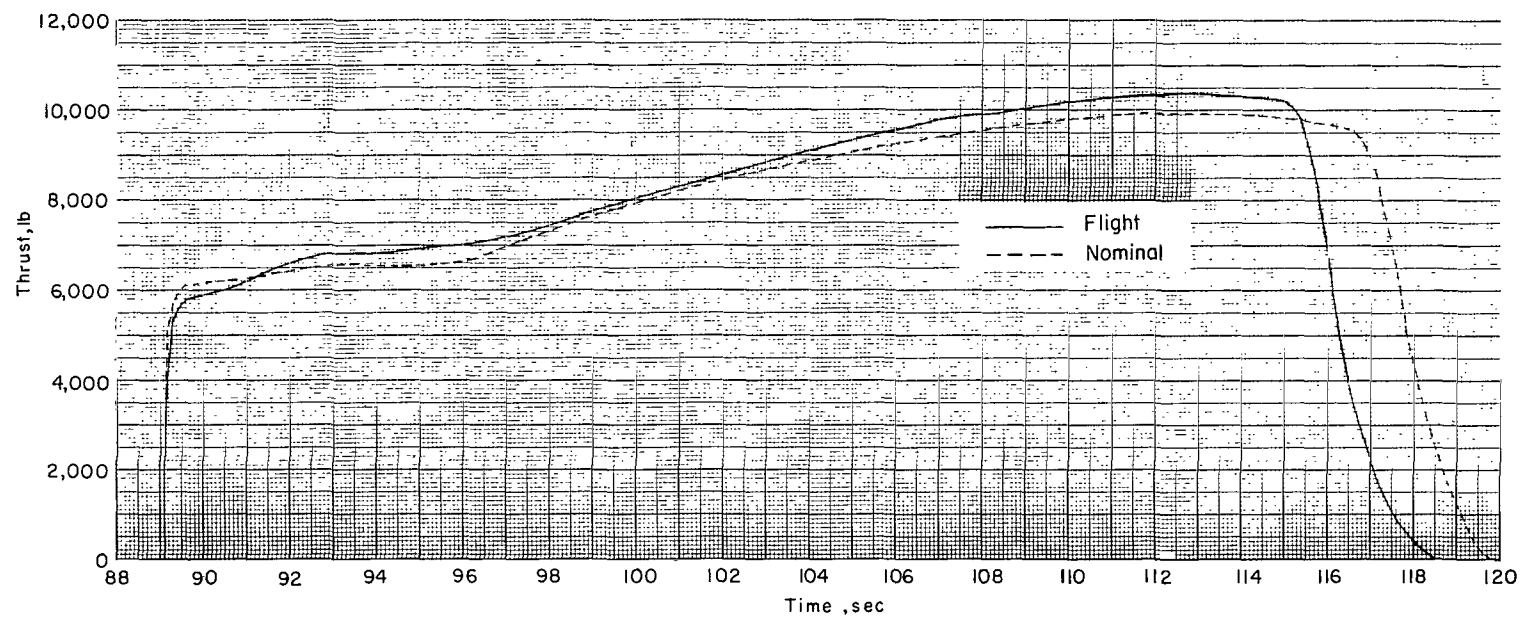
Figure 52.- Comparison of third-stage flight and nominal thrust.
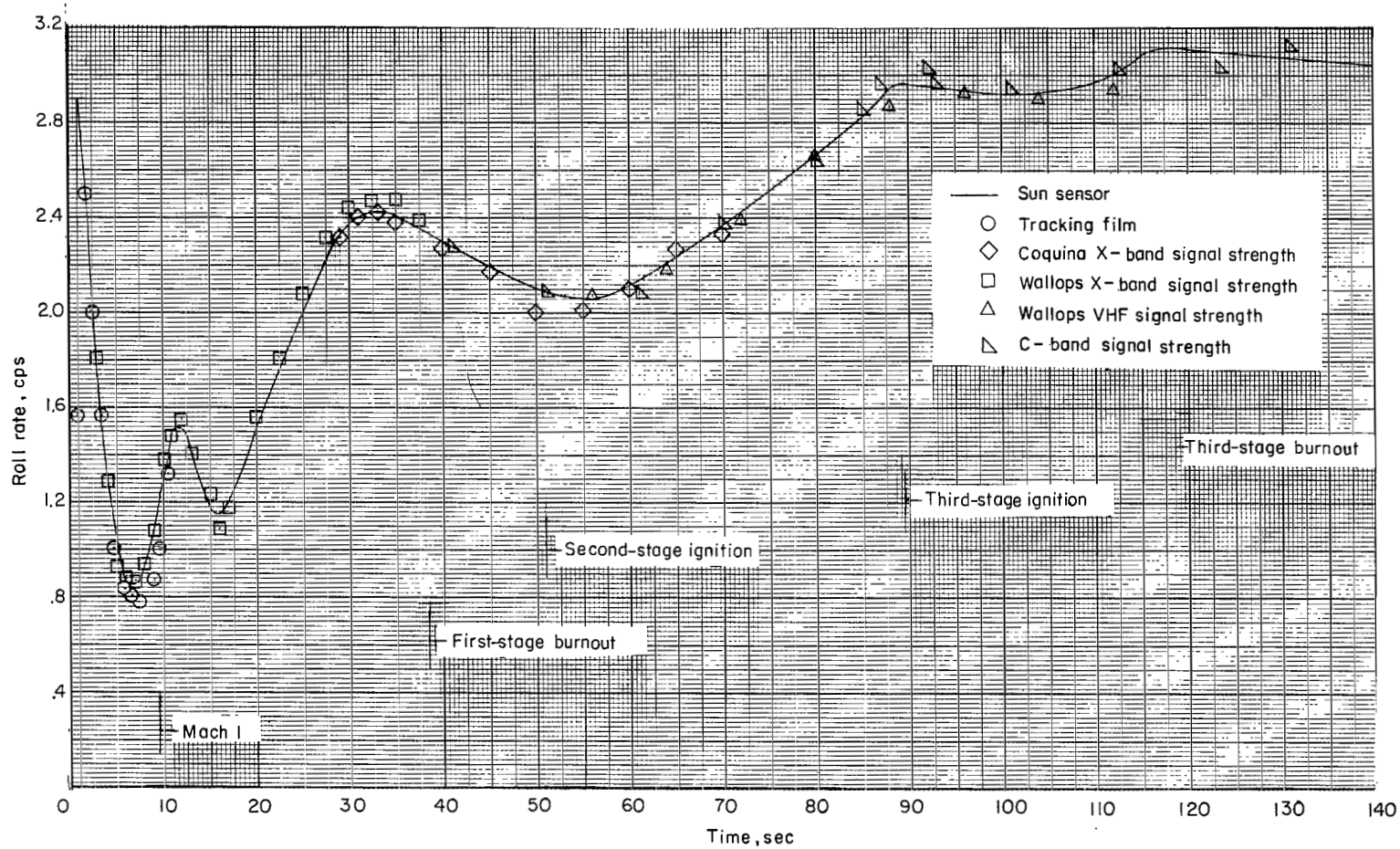
Figure 53.- Flight roll-rate history.
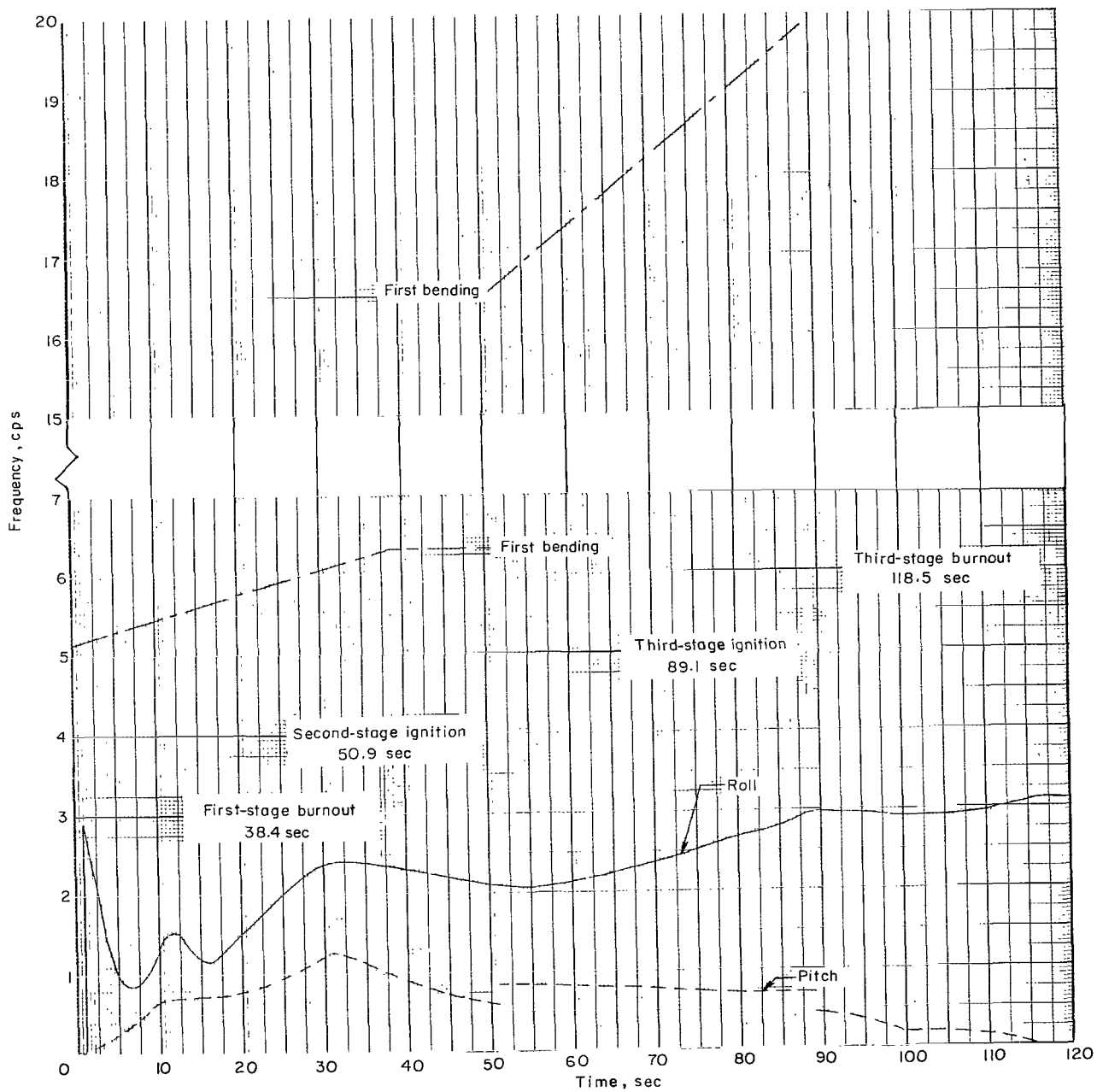
Figure 54.- Roll, pitch natural, and body-bending frequency histories.
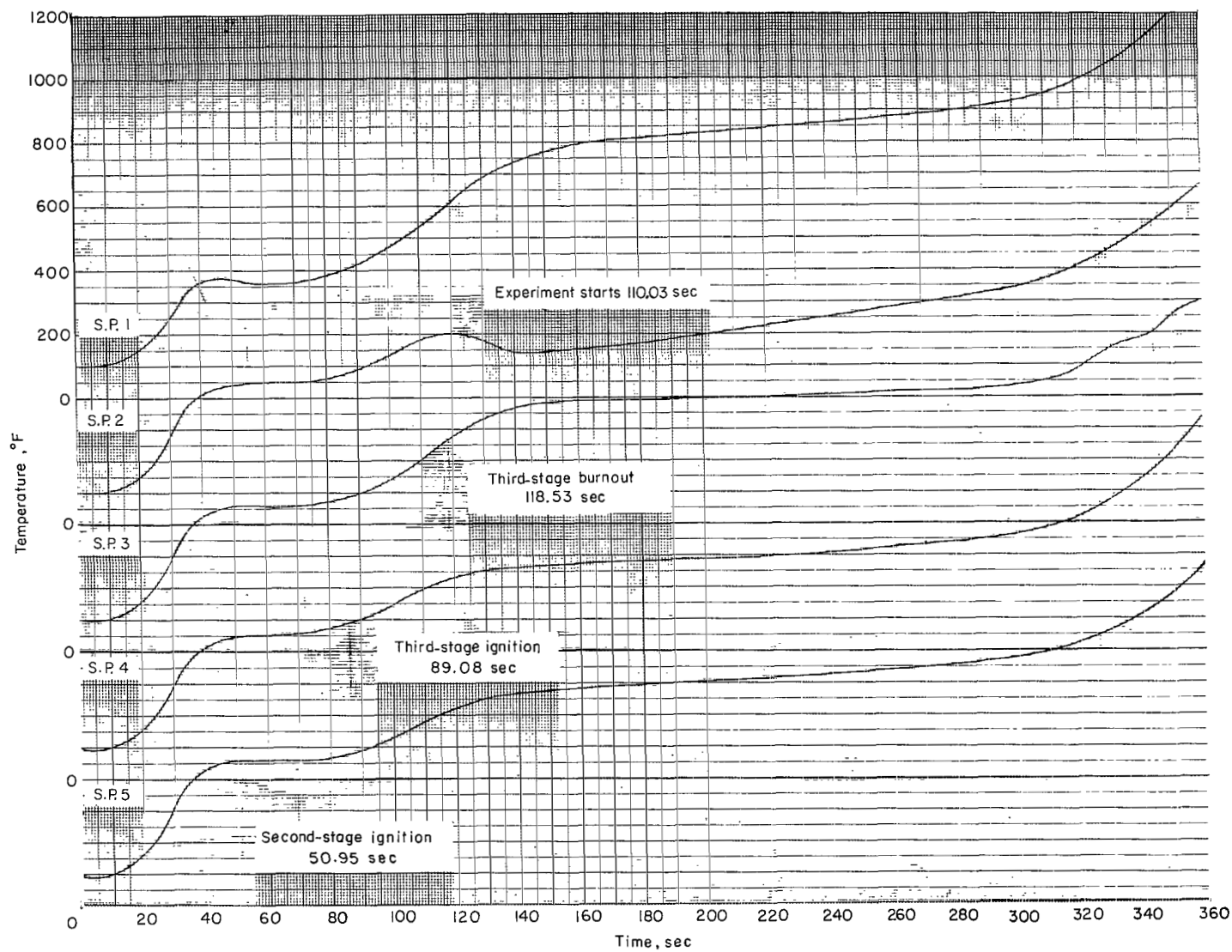
(a) Beryllium nose.

Figure 55.- Payload temperatures.
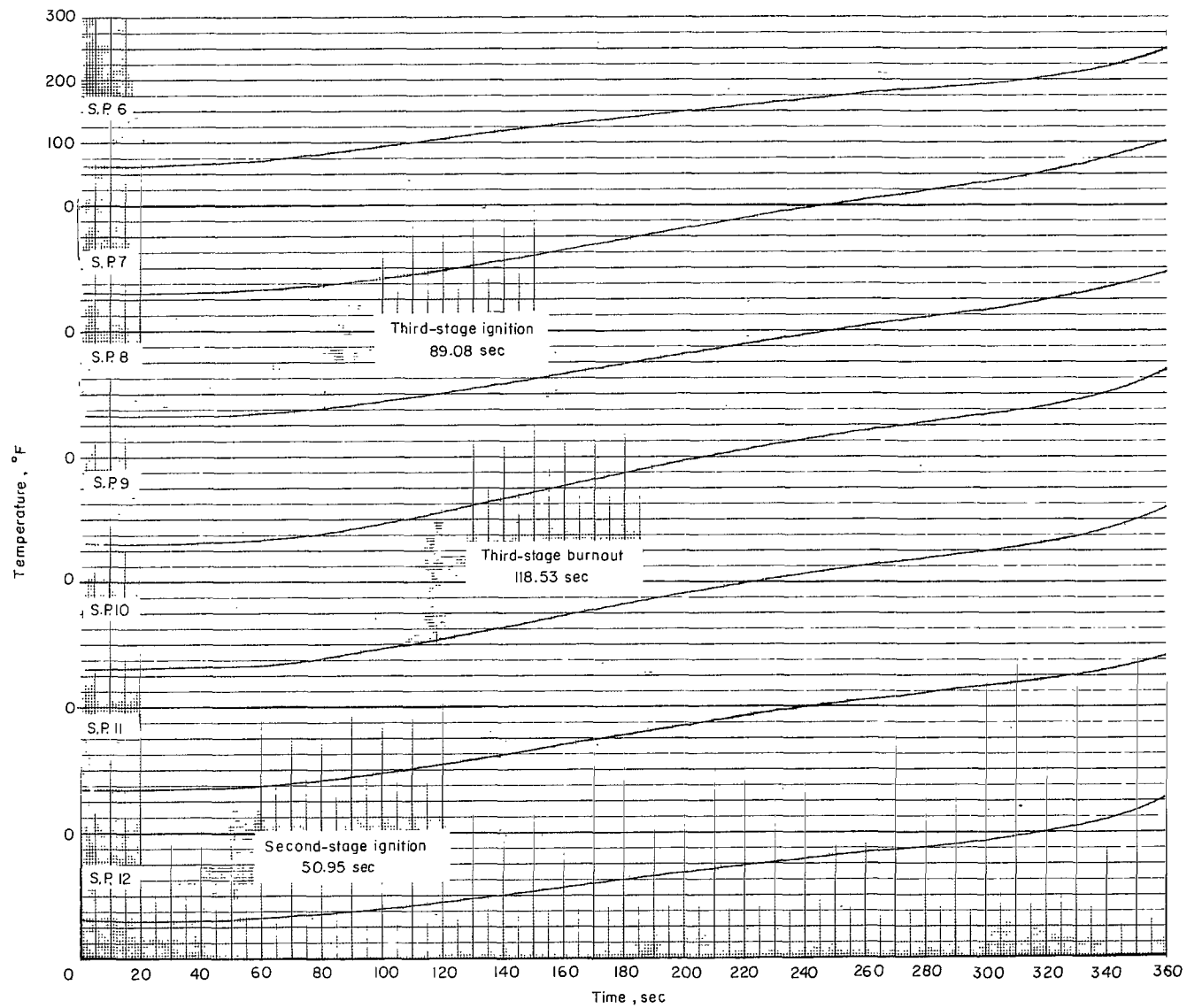
(b) Cone-cylinder.

Figure 55.- Concluded.
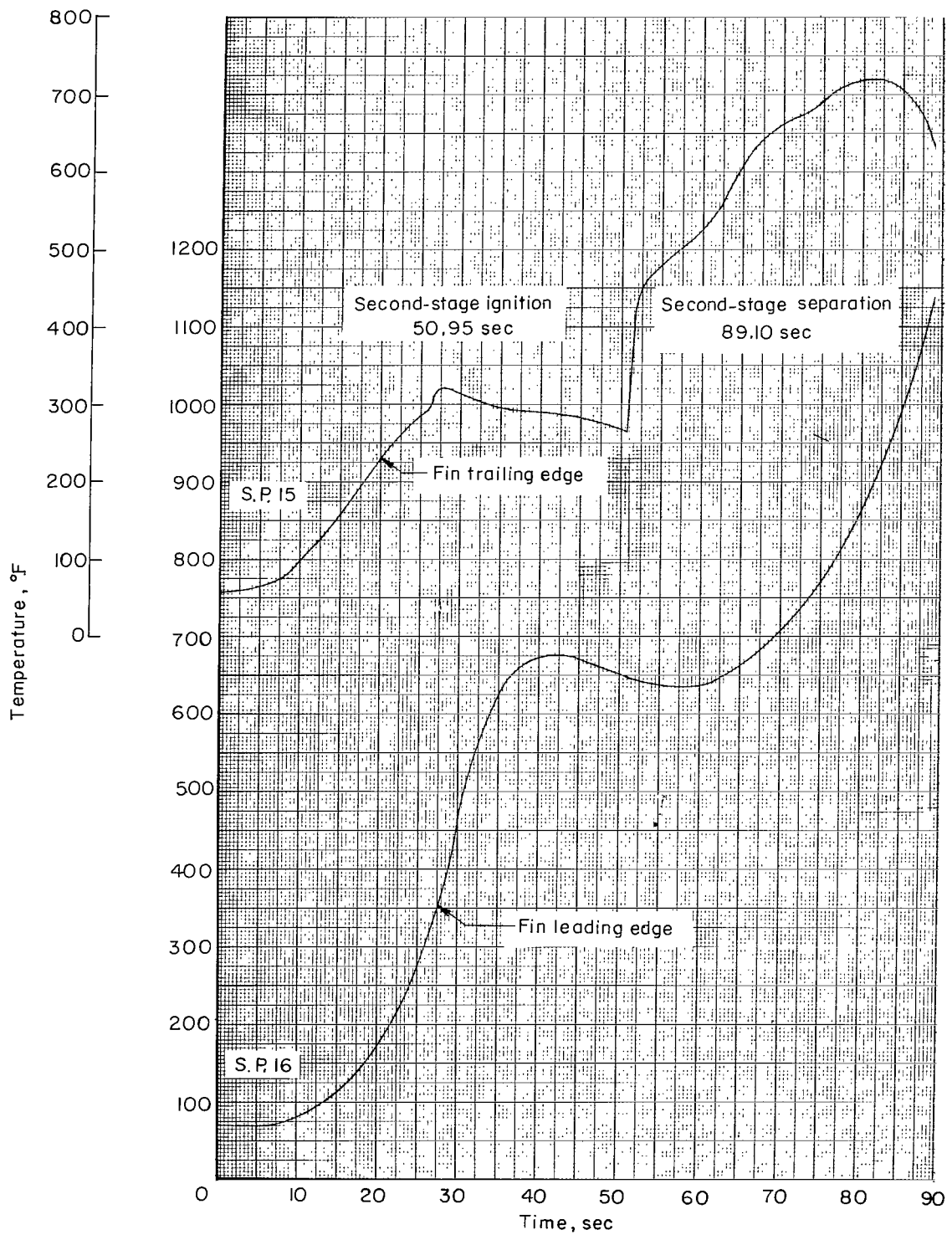
Figure 56.- Second-stage-fin leading-edge and trailing-edge temperature history.
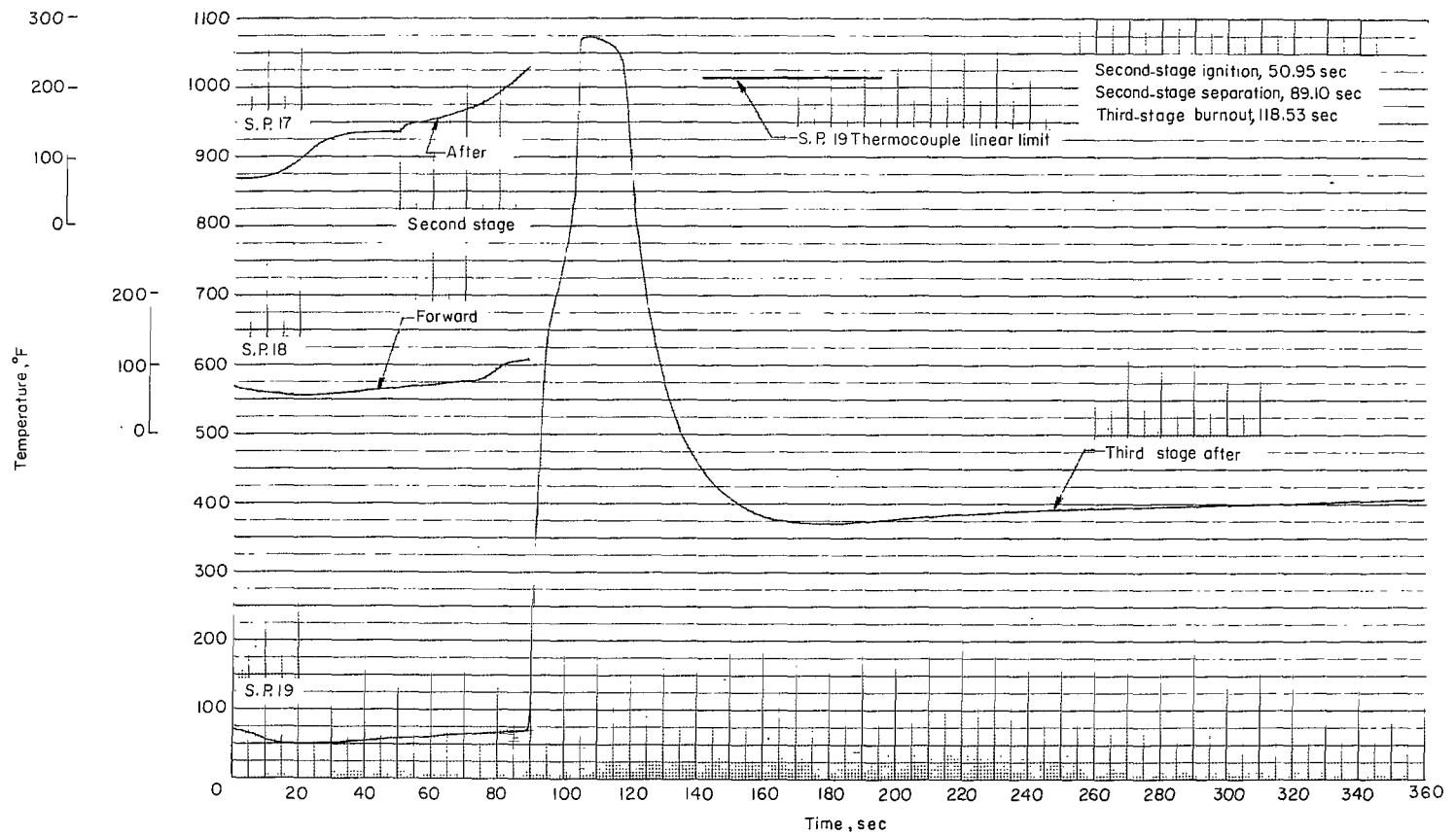
Figure 57.- Second- and third-stage-motor chamber dome free-air temperature histories.
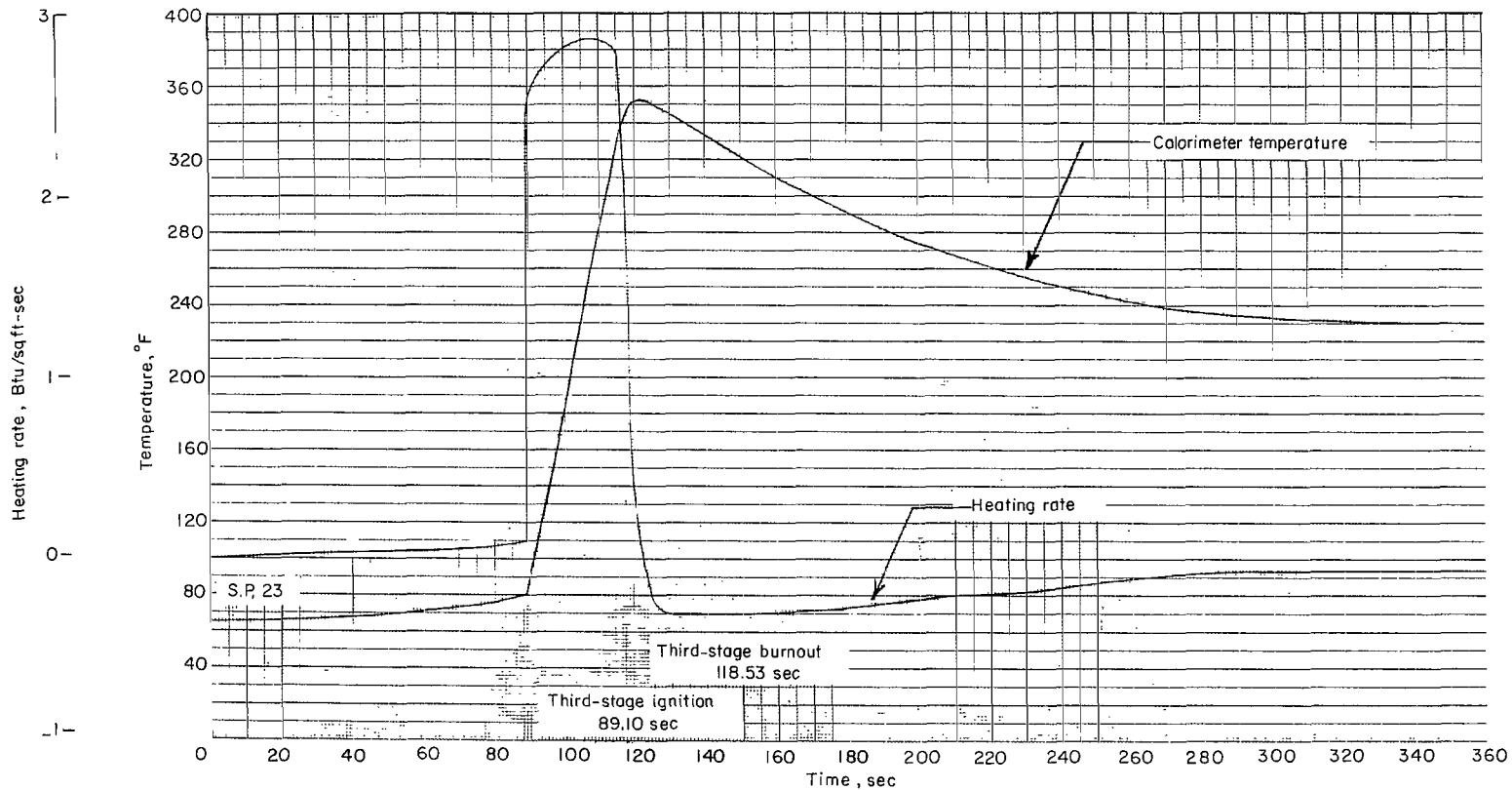
Figure 58.- Third-stage flare-closure temperature history.
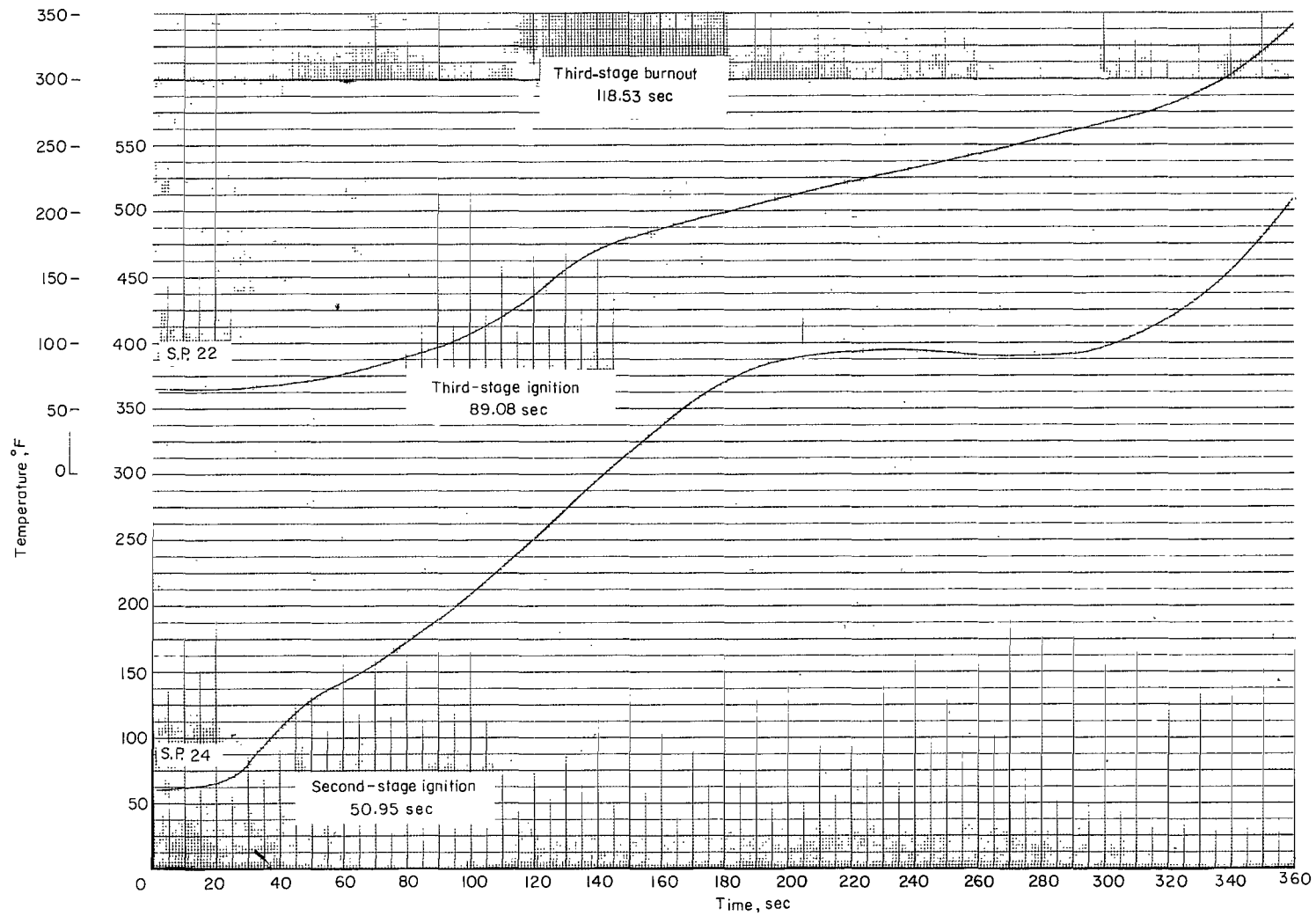
(a) Temperature histories.

Figure 59.- Flare-face temperature and heating-rate histories.
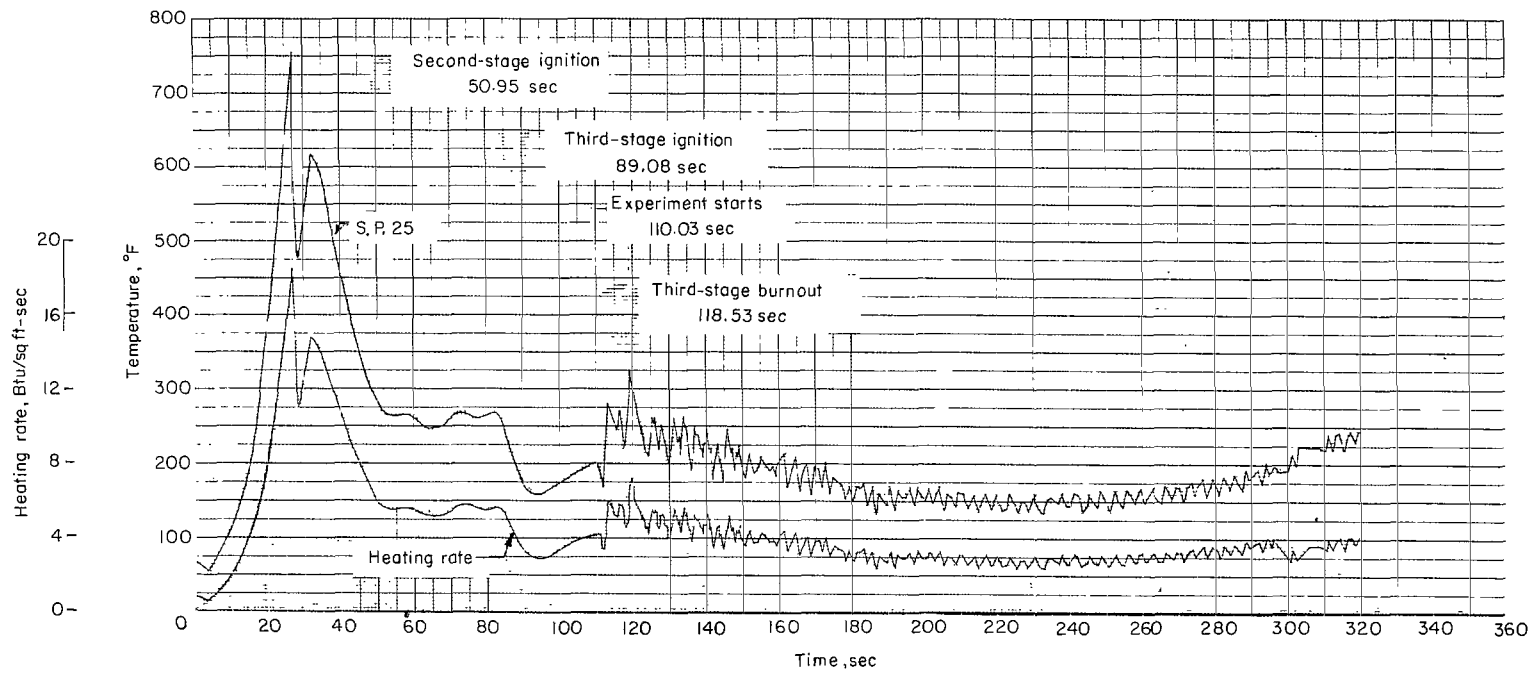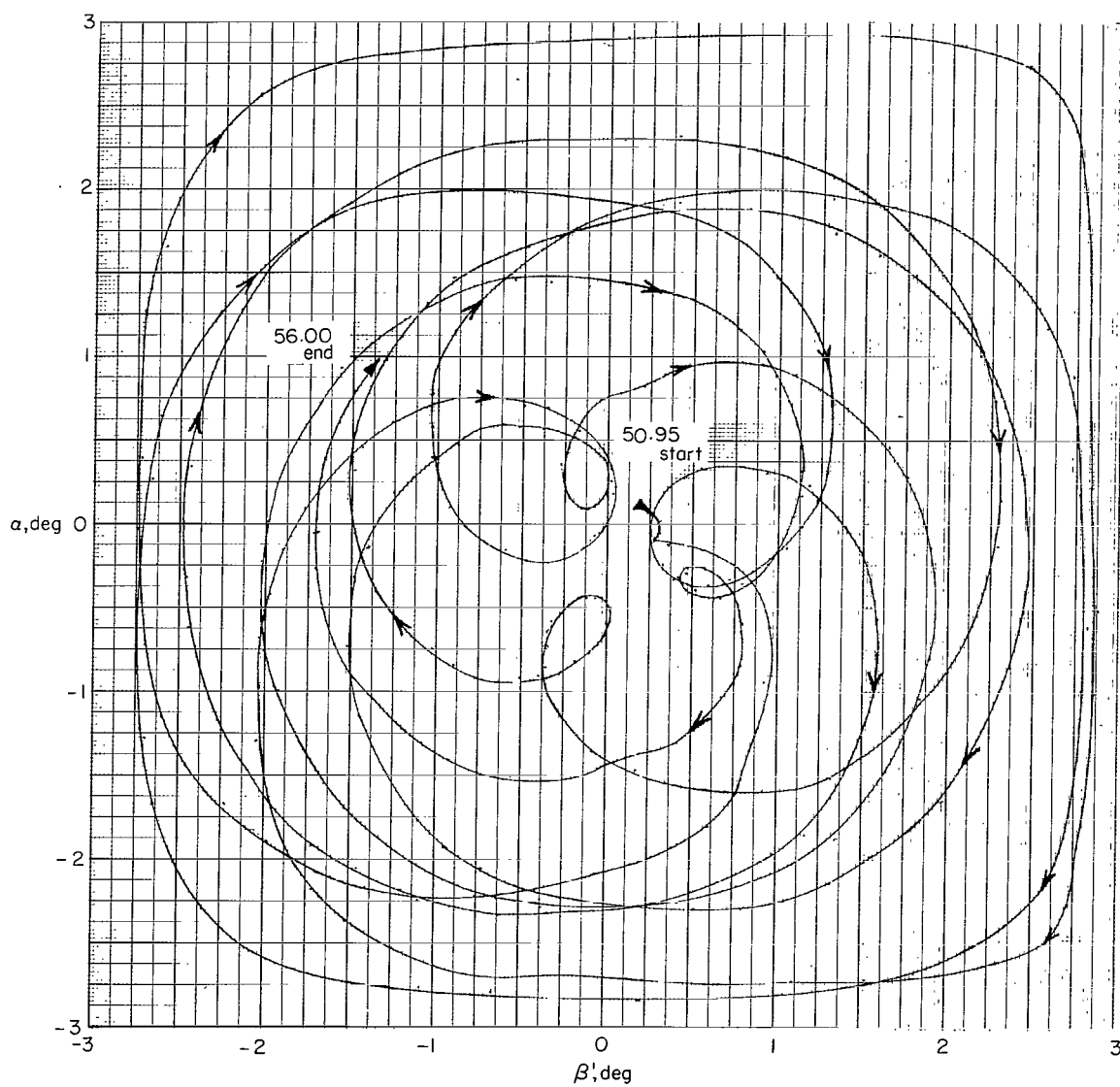
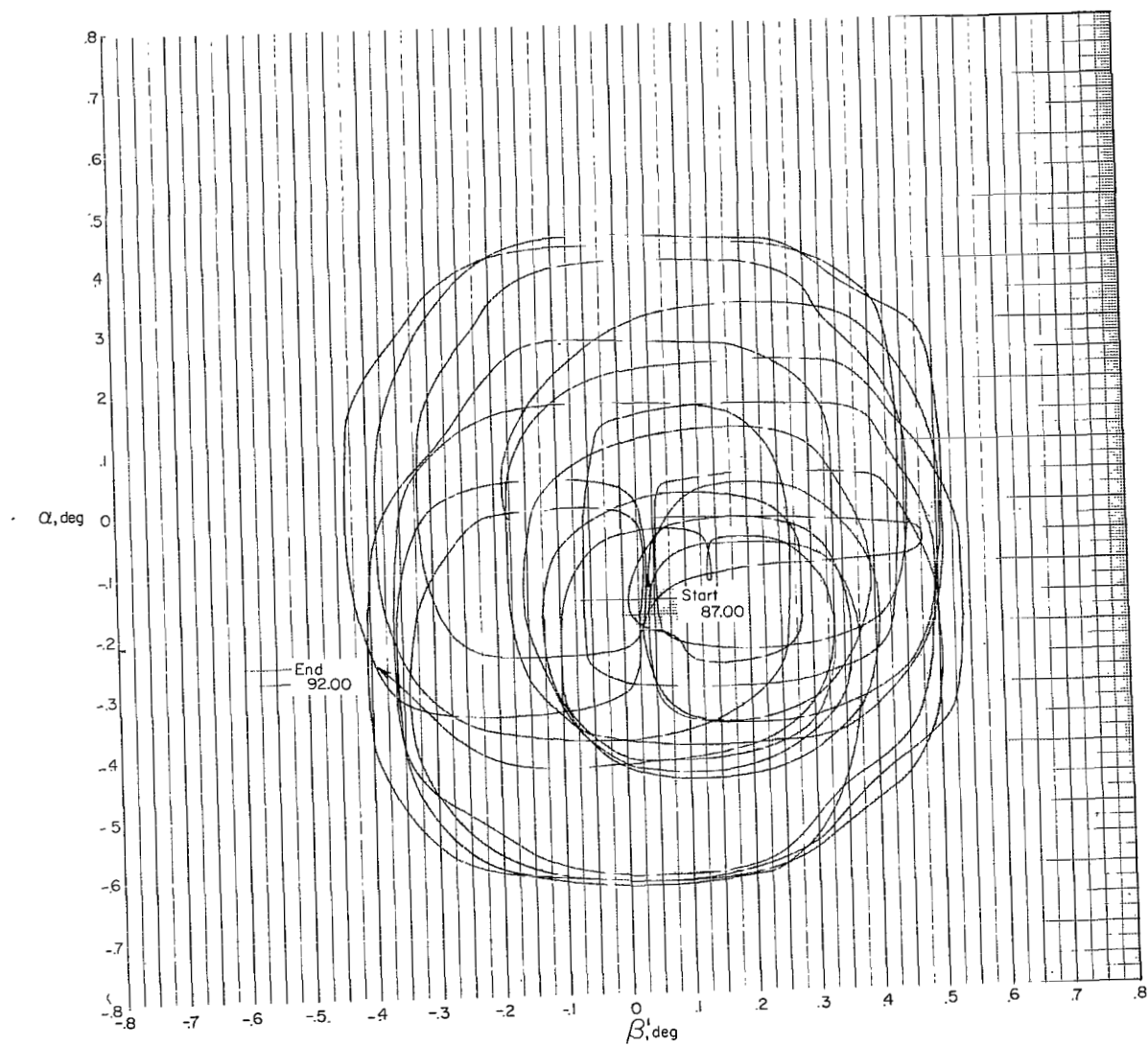(b) Heating-rate histories.

Figure 59.- Concluded.
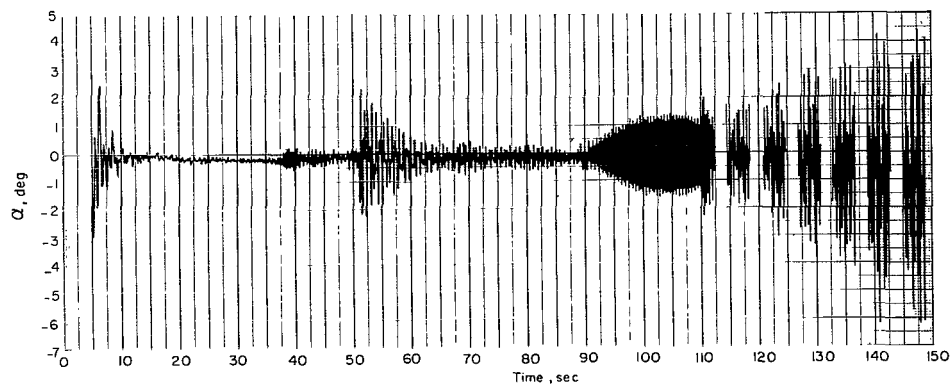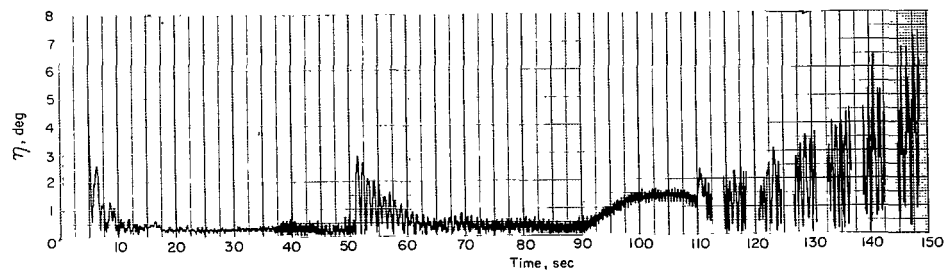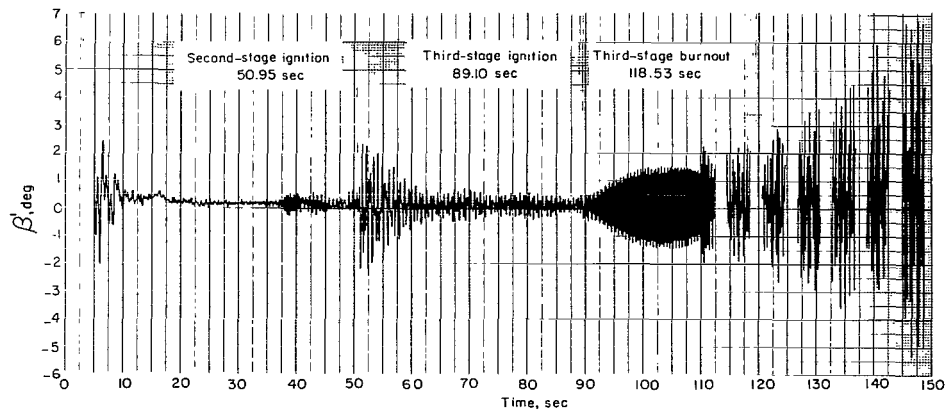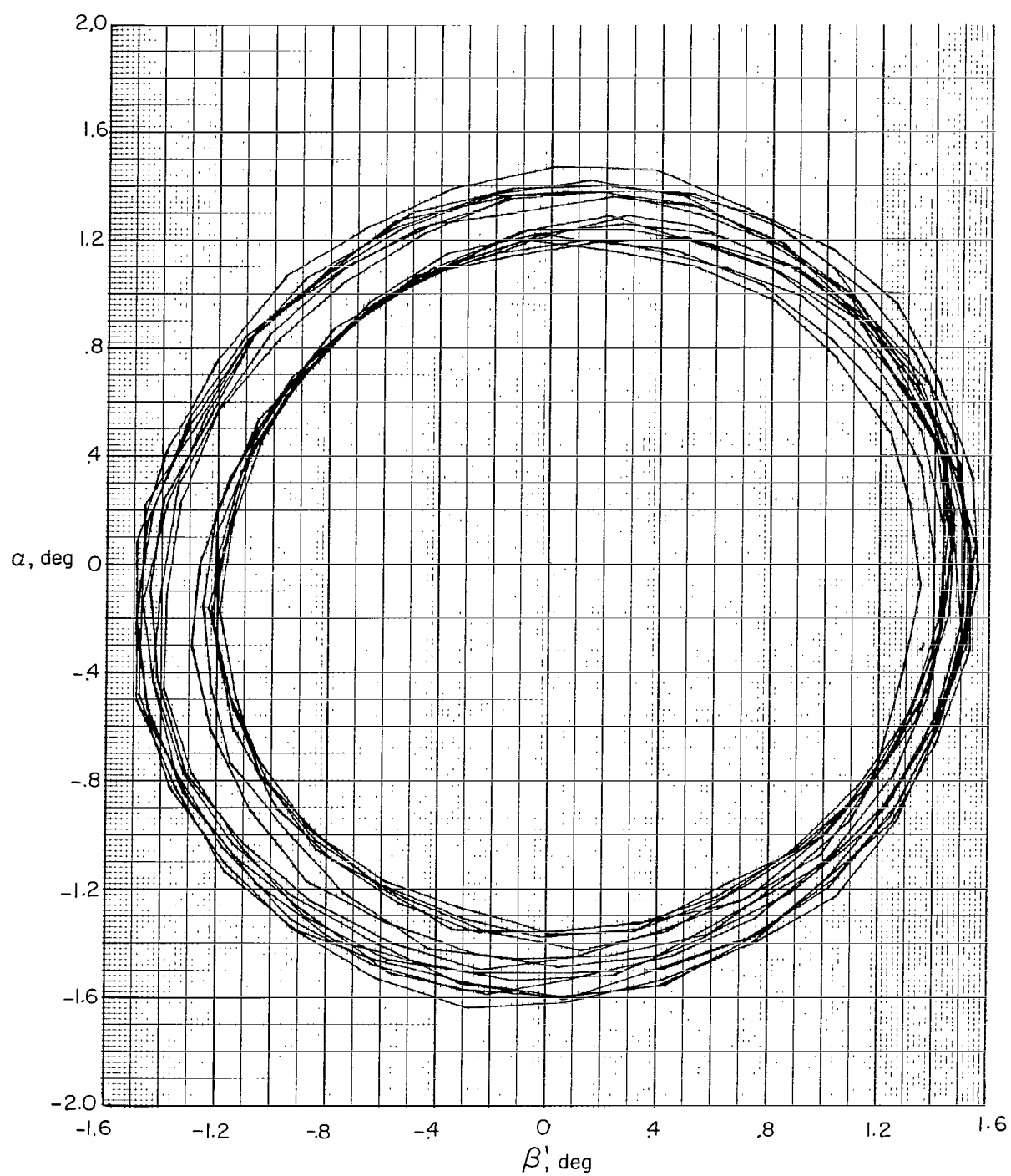
Figure 60.- Angle-of-attack histories.

(a) Second stage: 50.95 to 56.00 sec.

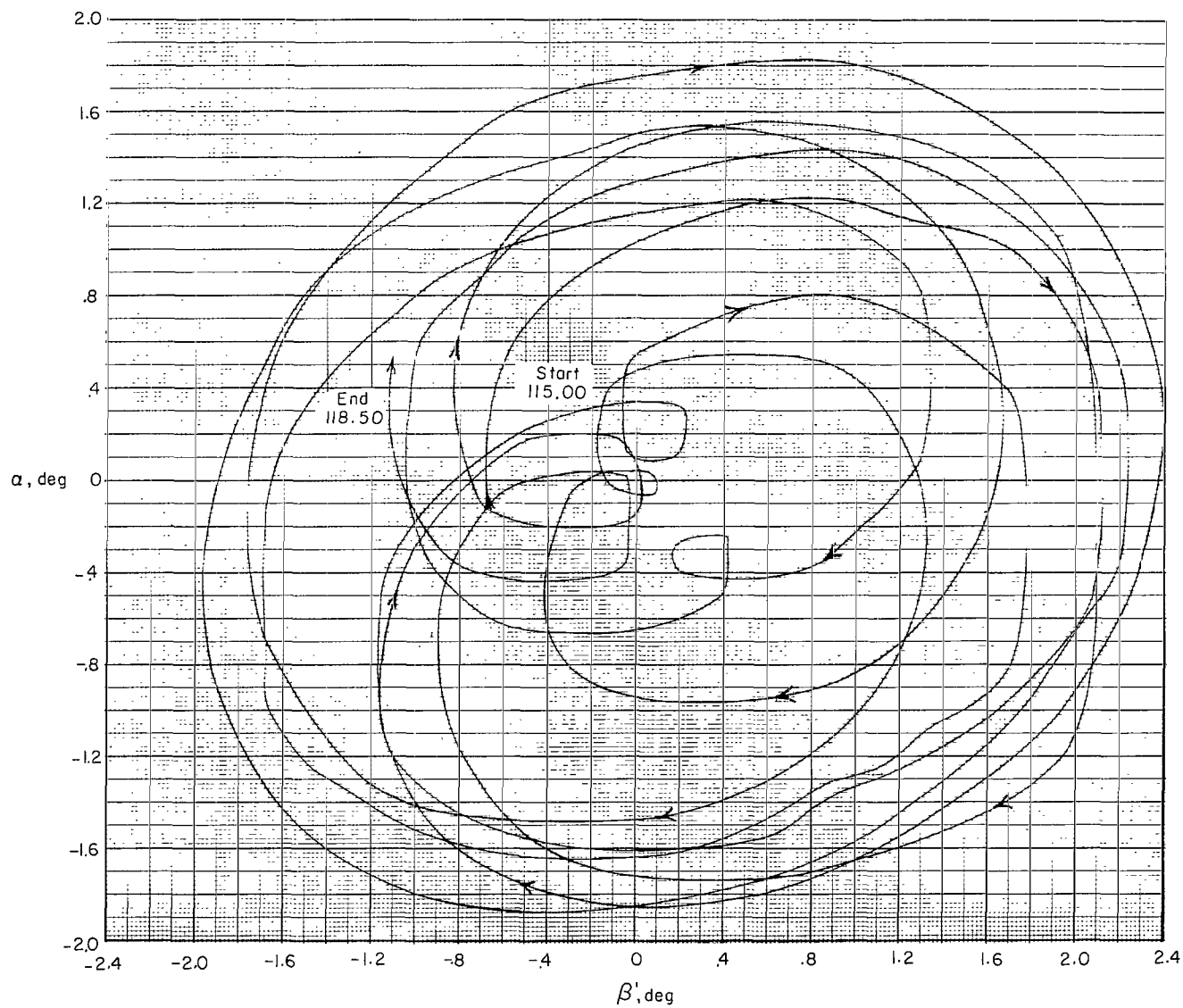Figure 61.- Angular motion cross plots.

(b) Third stage: 87.00 to 92.00 sec.

Figure 61.- Continued.

(c) Third stage: 104 to 108 sec.

Figure 61.- Continued.

(d) Third stage: 115.00 to 118.50 sec.

Figure 61.- Concluded.

"The aeronautical and space activities of the United States shall be conducted so as to contribute . . . to the expansion of human knowledge of phenomena in the atmosphere and space. The Administration shall provide for the widest practicable and appropriate dissemination of information concerning its activities and the results thereof."

—NATIONAL AERONAUTICS AND SPACE ACT OF 1958

NASA SCIENTIFIC AND TECHNICAL PUBLICATIONS

TECHNICAL REPORTS: Scientific and technical information considered important, complete, and a lasting contribution to existing knowledge.

TECHNICAL NOTES: Information less broad in scope but nevertheless of importance as a contribution to existing knowledge.

TECHNICAL MEMORANDUMS: Information receiving limited distribution because of preliminary data, security classification, or other reasons.

CONTRACTOR REPORTS: Technical information generated in connection with a NASA contract or grant and released under NASA auspices.

TECHNICAL TRANSLATIONS: Information published in a foreign language considered to merit NASA distribution in English.

TECHNICAL REPRINTS: Information derived from NASA activities and initially published in the form of journal articles.

SPECIAL PUBLICATIONS: Information derived from or of value to NASA activities but not necessarily reporting the results of individual NASA-programmed scientific efforts. Publications include conference proceedings, monographs, data compilations, handbooks, sourcebooks, and special bibliographies.

Details on the availability of these publications may be obtained from:

SCIENTIFIC AND TECHNICAL INFORMATION DIVISION
NATIONAL AERONAUTICS AND SPACE ADMINISTRATION
Washington, D.C. 20546